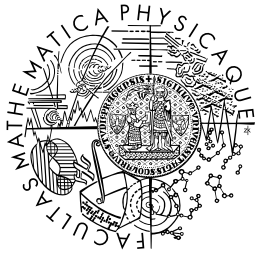

FACULTY
OF MATHEMATICS
AND PHYSICS
Charles University

DOCTORAL THESIS

Martin Krivoš

Study of production of jets and dijets in Xe+Xe and Pb+Pb collisions at the ATLAS experiment

Institute of Particle and Nuclear Physics

Supervisor of the doctoral thesis: doc. Mgr. Martin Spousta, Ph.D.
Study programme: Physics
Study branch: Particle and Nuclear Physics

Prague 2023

I declare that I carried out this doctoral thesis independently, and only with the cited sources, literature and other professional sources. It has not been used to obtain another or the same degree.

I understand that my work relates to the rights and obligations under the Act No. 121/2000 Sb., the Copyright Act, as amended, in particular the fact that the Charles University has the right to conclude a license agreement on the use of this work as a school work pursuant to Section 60 subsection 1 of the Copyright Act.

In Prague, January 31, 2023 .....

Author's signature

I would like to express my deepest gratitude to my supervisor, Martin Spousta, for his patience, excellent guidance, and endless support during my doctoral study.

A special thank you belongs to my colleague and dear friend Martin Rybář, who was always ready to help me with any problem.

I want to thank everyone in ATLAS heavy-ion group, namely Aaron, Adam, Anne, Barbara, Dhanush, Sebastian, and Tim, who helped me guide the Xe+Xe dijet analysis to the end.

I could not have undertaken this journey without my girlfriend Ingrid and all the great people at our department in Prague, namely Katka, Monsignor, Martin, Marek, Franciszek, Pavel, Hedvika, and Agnieszka.

Title: Study of production of jets and dijets in Xe+Xe and Pb+Pb collisions at the ATLAS experiment

Author: Martin Krivoš

Department: Institute of Particle and Nuclear Physics

Supervisor: doc. Mgr. Martin Spousta, Ph.D., Institute of Particle and Nuclear Physics

Abstract: A hot and dense medium is created during the heavy-ion collisions, affecting the strongly interacting particles forming jets. This typically leads to a suppression of jet production in heavy-ion collisions compared to jet production in proton-proton collisions. A study of this suppression in a dijet system, i.e., in a system of two back-to-back jets, can shed light on the details of the parton energy loss process responsible for this suppression. This thesis presents a measurement of dijet momentum balance in Xe+Xe collisions at $\sqrt{s_{\mathrm{NN}}} = 5.44$ TeV as measured by the ATLAS experiment at the LHC. Results were compared with the previous measurement of dijet momentum balance in Pb+Pb collisions at $\sqrt{s_{\mathrm{NN}}} = 5.02$ TeV. A significant momentum imbalance was observed in the most central Xe+Xe collisions, and this imbalance was decreasing with decreasing nuclear overlap. The ratio of a pair nuclear-modification factor further quantifies the differences between the dijet suppression in Xe+Xe and Pb+Pb collisions. The results are consistent with those measured in Pb+Pb data when compared in classes of the same event activity and when taking into account a difference between the center-of-mass energy of the initial parton scattering process in Xe+Xe and Pb+Pb collisions. These results provide new input for the understanding of the role of energy density, system size, path length, and fluctuations in the parton energy loss.

Keywords: Heavy-ion collisions, Quark-gluon plasma, Jet quenching, Dijet momentum balance, Xenon-xenon collisions, ATLAS Experiment

Contents

Introduction

The ultrarelativistic heavy-ion collisions at the LHC create a hot and dense medium of quasi-free quarks and gluons [1, 2, 3, 4]. Investigating this medium and its properties is one of the primary goals of the LHC heavy-ion program. In these collisions, an occasional hard scattering may happen between two colliding partons leading to a production of new high energetic quarks and gluons; these then radiate and create a flux of collimated particles called *jet*. It was shown [5] that jets are suppressed in the central Pb+Pb collisions by approximately a factor of two compared to *pp* collisions. The process leading to this suppression is called *jet quenching*. Strong suppression of jets was also observed in other systems such as gamma-jet or Z-jet systems [6, 7]. On the other hand, non-strongly interacting particles like gamma, Z, and W bosons (and their non-strongly interacting decay products) were measured in heavy-ion collisions and exhibited no suppression [8, 9].

Up to now, only suppression of charged hadrons was measured in Xe+Xe collision [10, 11, 12] and the jet energy loss in dijet system was measured only for Pb+Pb collisions at the LHC. The 2017 Xe+Xe run gives a unique opportunity to study jet quenching in collisions of lighter nuclei than Pb+Pb. This is attractive for several reasons. First, the underlying event is smaller in the most central collisions where the collision geometry is the most symmetric. Secondly, the lower number of nucleons in Xe compared to Pb nuclei may affect the amount of jet quenching through a reduction in both the overall energy density and path lengths traversed by the hard-scattered quarks and gluons in the QGP. Consequently, measurements in Xe+Xe collisions should provide more constraints on the impact of energy density, fluctuations, path length dependence, and on jet quenching. Studying the parton energy loss in a collision system that is smaller than the Pb+Pb system may also help to predict the energy loss for oxygen–oxygen collisions, which are intended to be performed during LHC Run 3 [13].

Measurements of imbalance in the transverse momenta of the two highest p_{T} jets can give us more insight into the processes influencing the jet quenching. This imbalance studies how much more or less the highest-p_{T} jet (leading jet) is suppressed compared to the second highest-p_{T} jet (subleading jet). A higher imbalance was observed in Pb+Pb collisions compared to *pp* ones [14, 15]. This suggests that momentum imbalance is an effect of interactions with the QGP. An increased imbalance shows that the two jets lose energy unevenly in the QGP – this may be due to various effects, for instance, their different path in the medium.

This thesis presents a momentum balance measurement of two highest p_{T}[1] jets forming a dijet in Xe+Xe collisions. The measure of momentum balance is

[1]Throughout this thesis, the following notation is used: z-axis points along the direction of the traveling particle, e.g., along the beam pipe. Cylindrical coordinates (r, ϕ) are used in the transverse plane, ϕ being the azimuthal angle around the z-axis. The pseudorapidity is defined in terms of the polar angle θ as $\eta = -\ln\tan(\theta/2)$ and the rapidity is defined in terms of the energy E and z-component of the momentum, p_z, as $y = 1/2\ln((E+p_z)/(E-p_z))$. Transverse momentum and transverse energy are defined as $p_{\mathrm{T}} = p\sin(\theta)$ and $E_{\mathrm{T}} = E\sin(\theta)$, respectively. The angular distance between two objects with relative differences $\Delta\eta$ in pseudorapidity and $\Delta\phi$ in azimuth is given by $\Delta R = \sqrt{(\Delta\eta)^2 + (\Delta\phi)^2}$.

defined by the ratio:

$$x_{\mathrm{J}} = \frac{p_{\mathrm{T},2}}{p_{\mathrm{T},1}},$$

where $p_{\mathrm{T},1}$ and $p_{\mathrm{T},2}$ are transverse momenta of the leading and subleading jets, respectively. The two jets must be back-to-back in azimuth, satisfying the condition $|\Delta\Phi| = |\Phi_1 - \Phi_2| > 7/8\pi$, where Φ_1 and Φ_2 are azimuthal coordinates of the leading and subleading jet, respectively. Both jets are required to be in rapidity region $|y| < 2.1$.

Two normalizations are used for the x_{J} distributions. The first one is normalization by the number of dijets (N_{pair}):

$$\frac{1}{N_{\mathrm{pair}}} \frac{\mathrm{d}N}{\mathrm{d}x_{\mathrm{J}}}, \tag{1}$$

which is referred to as *per-pair normalized* momentum-balance distribution. The second normalization is by the effective heavy-ion luminosity:

$$\frac{1}{N_{\mathrm{evt}}} \frac{1}{\langle T_{\mathrm{AA}} \rangle} \frac{\mathrm{d}N}{\mathrm{d}x_{\mathrm{J}}}, \tag{2}$$

which is called *absolutely normalized* momentum-balance distribution. Here, $\langle T_{\mathrm{AA}} \rangle$ is the nuclear thickness function [16] and N_{evt} is the number of minimum bias events in a given centrality interval. The self-normalized distributions were measured in dijet asymmetry measurements [14, 15], and they allow to quantify the impact of the jet quenching on the dijet momentum balance in the most simple way. The absolutely normalized distributions allow to directly compare the absolute yields of jet pairs across different centralities. This normalization was applied in the latest Pb+Pb measurement [15].

The presented analysis uses dijet yields to also calculate the ratio of pair nuclear modification factor between Xe+Xe and Pb+Pb collisions for both leading and subleading jets yield. For the leading jets yield, this ratio is defined as

$$\rho_{\mathrm{Xe,Pb}}(p_{\mathrm{T},1}) = \frac{R_{\mathrm{AA}}^{\mathrm{pair}}(p_{\mathrm{T},1})|_{\mathrm{Xe+Xe}}}{R_{\mathrm{AA}}^{\mathrm{pair}}(p_{\mathrm{T},1})|_{\mathrm{Pb+Pb}}},$$

where $R_{\mathrm{AA}}^{\mathrm{pair}}(p_{\mathrm{T},1})|_{\mathrm{AA}}$ is pair nuclear modification factor for leading jets in AA collisions.

The first two chapters of the thesis give a theoretical introduction to Quantum chromodynamics and heavy-ion collisions. Chapter 3 introduces the ATLAS experiment. In Chapter 4, a detailed description of the jet reconstruction procedure in ATLAS is provided. Chapter 5 presents the Xe+Xe dijet measurement with the results.

1. Strong Interaction at Particle Colliders

The most successful description of elementary particles is provided by Standard Model (SM), which was finalized in the late 1970s. It classifies all particles into two main groups: fermions (particles with half-spins) and bosons (particles with integer spins). There are 24 different fermions: six quarks (up, down, charm, strange, top, and bottom), six leptons (electron, electron neutrino, muon, muon neutrino, tauon, tauon neutrino), and 12 antiparticles — one for each particle. Fermions respect Pauli exclusion principle — two fermions cannot occupy the same quantum state [17]. On the other hand, bosons do not respect the exclusion principle, and in SM, they are the force carriers. The known bosons are a photon, Z, $W^{\pm}$, gluons, and Higgs boson. In SM, all particles are represented by quantum fields in four-dimensional space-time. The model has a local SU(3)×SU(2)×U(1) gauge symmetry, which gives rise to the three fundamental interactions. The SU(2)×U(1) symmetry is responsible for the electroweak interaction, a unification of weak and electromagnetic interaction. SU(3) symmetry generates gluon fields that interact with quarks and represent strong interaction. The results of this thesis aim to investigate the properties of the SU(3) gauge symmetry group, called Quantum Chromodynamics (QCD). In this chapter, we will provide a brief introduction to the QCD. For a great introduction to quantum field theory and the basics of the electroweak interaction, the reader is referred to [18, 19, 20].

1.1 Quantum Chromodynamics

We start with a Dirac equation of motion for a quark with a mass m [18]:

$$(i\gamma^{\mu}\partial_{\mu} - m)\mathbf{\Psi} = 0, \tag{1.1}$$

where γ^{μ} are Dirac matrices and the wave function $\mathbf{\Psi} = \psi(x)\chi_c$ is a product of a Dirac spinor $\psi(x)$ and a color wave function χ_c. There are three different colors with corresponding quantum states:

$$\chi_{\text{Red}} = \begin{pmatrix}1\\0\\0\end{pmatrix}, \quad \chi_{\text{Green}} = \begin{pmatrix}0\\1\\0\end{pmatrix}, \quad \chi_{\text{Blue}} = \begin{pmatrix}0\\0\\1\end{pmatrix}. \tag{1.2}$$

Interaction carrier fields arise by requiring an invariance under a local gauge transformation

$$\mathbf{\Psi} \rightarrow \mathbf{\Psi'} = e^{ig_s/2t_a\omega_a(x)}\mathbf{\Psi}, \tag{1.3}$$

where t_a are generators of the SU(3) group, which in the matrix representation are widely known as 3×3 Gell-Mann matrices. These generators satisfy a commutation relation $[t_a, t_b] = i2f_{abc}t_c$, where f_{abc} are structure constants of SU(3) Lie algebra. Invariance under the (1.3) is only possible, if we define the following

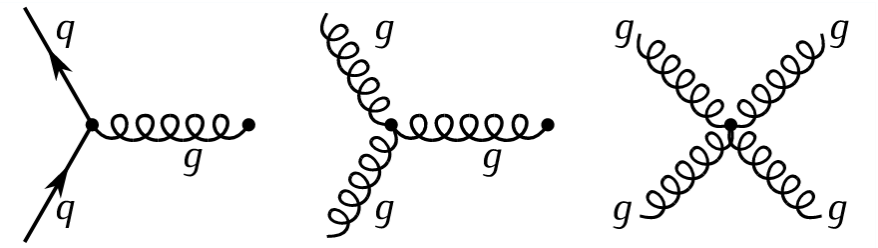

Figure 1.1: Feynman diagrams for interaction vertices of QCD represented by interaction Langrangian $\mathcal{L}_{\text{int}}$ in eq. (1.6) from left to right .

transformations [20]:

$$\partial^\mu \to (D^\mu)_{ij} = \partial^\mu \delta_{ij} + i\frac{g_\text{s}}{2} t_{a,ij} A_a^\mu$$
$$A_a^\mu \to A_a'^\mu = A_a^\mu + \frac{1}{g_\text{s}} \partial^\mu \omega_a(x) - f_{abc}\omega_b(x) A_c^\mu$$

where A_i are eight gluon fields, and g_s is the QCD coupling constant, which can be equivalently expressed as $g_\text{s} = \sqrt{4\pi\alpha_\text{S}}$. Now we are ready to write SU(3) local gauge invariant QCD Lagrangian [19]:

$$\mathcal{L}_\text{QCD} = -\frac{1}{4} G_{\mu\nu}^a G^{a\,\mu\nu} + \sum_f \bar{\psi}_{f,a} (i\gamma^\mu (D_\mu)_{ab} - m_f \delta_{a,b}) \psi_{f,b}, \tag{1.4}$$

where index f runs for all different flavors of quarks, a and b are color indices and run from 1 to the number of colors for quarks $N_\text{C} = 3$, and $G_{\mu\nu}^C$ is a field strength tensor defined as:

$$G_{\mu\nu}^a = \partial_\mu A_\nu^a - \partial_\nu A_\mu^a - g_\text{s} f^{abc} A_\mu^b A_\nu^c. \tag{1.5}$$

From (1.4), an interaction term $\mathcal{L}_\text{int}$ can be extracted:

$$\mathcal{L}_\text{int} = g_\text{s} A \bar{\psi} \psi + g_\text{s} AA\partial A + g_\text{s}^2 AAAA. \tag{1.6}$$

Three terms represent three different interaction vertices whose Feynman diagrams are shown in Figure 1.1 — ordered from left to right. The first term is analogous to the quantum electrodynamics vertex with the photon. The latter two arise because the gluon, in contrast with a photon, carries a non-zero color charge. This gluon self-interaction is a direct consequence of a non-abelian property of the SU(3) group.

The non-abelian theory can be proven to have two interesting properties, which turn out to have a crucial impact on the world we see: The first one is *color confinement* — it means that all we can observe are color-neutral hadrons. The second property is *asymptotic freedom*. It means that the interaction gets weaker as the length scale decreases or, equivalently, the energy scale increases. These properties result from a running coupling and a renormalization procedure shown in the next section.

1.2 Running Coupling Constant

A renormalization procedure removes divergences from loop QCD diagrams. It is far beyond the scope of this thesis to describe the renormalization procedure in

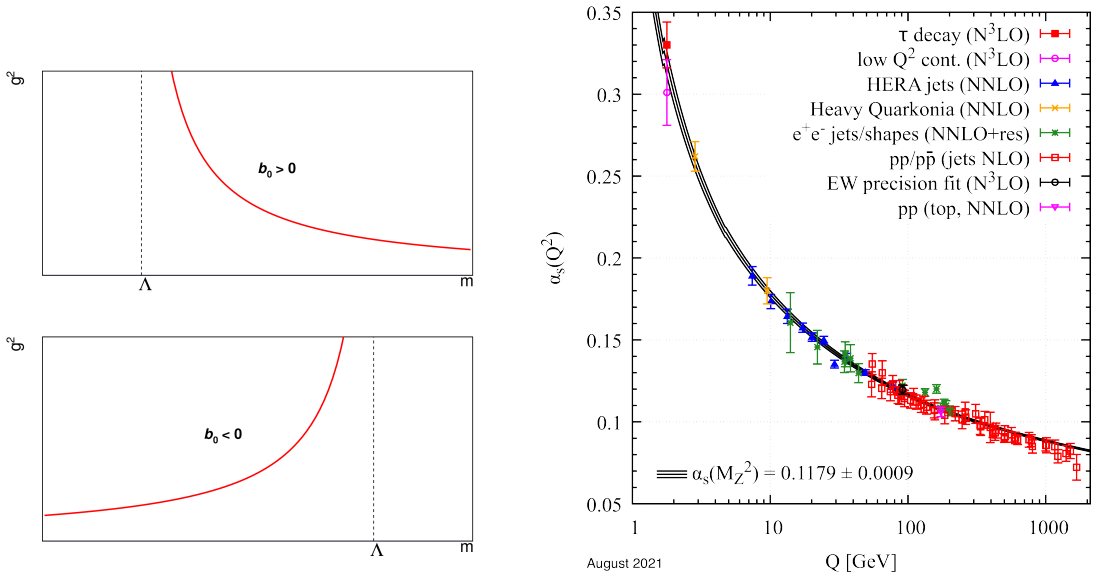

Figure 1.2: Left: Landau poles for two signs of parameter b_0. Right: A summary of different measurements of α_S for different energy scales Q. Figure is taken from [23].

detail. A good introduction is provided in Part II of Ref. [19]. The whole Standard Model, and QCD as its part, is renormalizable. This means that loop divergences can be removed in the perturbative approach. After the renormalization, the QCD coupling constant α_S depends on a non-physical energy scale μ, and this dependence is described by the renormalization group equation [19]:

$$\beta(\alpha_S) = \mu^2 \frac{\partial \alpha_S}{\partial \mu} = -\alpha_S^2 (b_0 + \alpha_S b_0 + \ldots), \tag{1.7}$$

where N_c is the number of colors and n_f is the number of quark flavors. $b_0 = (11N_c - 2n_f)/(12/\pi)$ [21, 22] and $b_1 = (17N_c^2 - 19n_f)/(24\pi)$ [23] are 1- and 2-loop β-function coefficients, respectively. Up to 2 loops, coefficients b are independent of the renormalization scheme when masses of quarks are zero. Choosing μ close to the scale of the momentum transfer Q in a given process, then $\alpha_S(\mu^2 = Q^2)$ is indicative of the effective strength of the strong interaction in that process [23]. The change of α_S with μ is called the running of the coupling constant.

At the leading order (LO), $\alpha_S(\mu)$ is divergent at $Q^2 = \Lambda^2_{\mathrm{QCD}}$ which is called *Landau pole*. Close to this pole, values of α_S are too big for the perturbation approach to be used. In general, for any coupling constant, these divergences can be classified into two types by the sign of b_0. Figure 1.2 (left) shows these two possibilities. When $b_0 > 0$, we have a divergence for small μ. For $b_0 < 0$, the divergent pole is for large μ values. The QCD has a positive b_0 and therefore is of the second type. This means that when we increase the energy of the interaction, the strong force gets weaker, and quarks and gluons are becoming free in the limit of $\mu \to \infty$. This is the explanation of the already mentioned asymptotic freedom. On the other hand, for low μ values (and low energies), the perturbative approach can no longer be used.

From (1.7), one can get for α_S in the LO

$$\alpha_S(\mu) = \frac{1}{b_0 \ln \frac{\mu^2}{\Lambda^2_{QCD}}}, \tag{1.8}$$

where Λ_{QCD} is the Landau pole for QCD, and in the LO, it is ≈ 200 MeV [23]. This energy is in the order of mass scales in typical hadrons. For this reason, a perturbative QCD cannot be used in the description of the structure of baryons or mesons.

Figure 1.2 (right) summarizes values of α_S measured at different processes with various values of μ. Because the first precise measurement of α_S was done at LEP at the energy of Z boson mass ($m_Z \approx 91$ GeV), all other measurements for different μ are recalculated to this value using the renormalization group equation. The world average value of α_S is then reported at $\mu = m_Z$ and is [23]

$$\alpha_S(m_Z) = 0.1179 \pm 0.0009.$$

1.3 Jets and Jet Algorithms

During a hard scattering where high momentum is transferred, in both pp and heavy-ion collisions, high-energy partons are created in the interaction vertex. One would like to measure their distributions, but due to color confinement, these partons are not the final observable states of the interaction. They radiate quarks and gluons; these then hadronize into color-neutral hadrons, creating a shower of particles. This shower is called *jet*. Ideally, we would like to identify all particles in the jet and reverse-engineer their decays into the original parton. This is difficult and ambiguous. As a consequence of that, we define and study jets instead of the initial partons.

We need a reliable method to reconstruct the jets in theory and experiment consistently. For this, we define a set of rules called *jet algorithms*. For one collision, different algorithms will likely create a different set of jets. Therefore, a jet is defined by the jet algorithm.

1.3.1 Jet Alorithms

There are two main requirements we impose on a jet algorithm. The first one is *infrared safety*. The algorithm is infrared safe if adding a soft (low momentum) particle does not change the definitions of jets in the event. Figure 1.3 (right) shows an example of an unsafe infrared algorithm, where an added soft particle in the middle of two jets merges them into one jet. The second requirement is *collinear safety*. It can happen that a detector falsely identifies one particle as two weaker colinear particles. The jet definition should stay the same if this happens. Looking at Figure 1.3 (left), splitting a particle into two has missed a potential jet in the event.

Because modern detectors have to process large amounts of collisions (e.g., LHC can deliver collisions every 25 ns), it is desired that the jet algorithms are fast enough to process large volumes of data.

We can classify the most commonly used algorithms into two groups: The first group is called *cone algorithms*. They identify jets as a set of particles within a

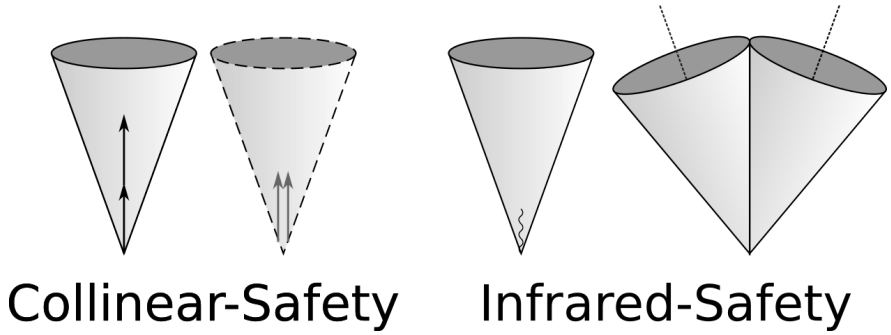

Figure 1.3: A demonstration of unstable behavior of jet algorithms. Left: Colinear unstable. Right: Infrared unstable.

calculated cone in space. The basic cone algorithm identifies the highest momentum particle and includes all particles in its predefined distance R into a jet. Such a procedure was shown to be neither co-linear nor intra-red safe. Its improved version — *seedless cone algorithm* (SISCone) removes these shortcomings but is computationally more demanding.

The second group is *clustering algorithms*. They are sequentially joining particles nearby in phase space into new pseudoparticles. This joining of particles continues iteratively until the pseudoparticles cannot be merged anymore. The final pseudoparticles or clusters are the final jets. The distance in the phase space can be defined in different ways, which will change the behavior of the algorithm, as we will see below. The clustering algorithms are used in most modern particle experiments, and their individual steps are described below.

As the first step in every iteration, the algorithm calculates the distance between each pair of particles,

$$d_{ij} = \min(p_{\mathrm{T},i}^{2k}, p_{\mathrm{T},j}^{2k}) \frac{R_{ij}^2}{R^2} \tag{1.9}$$

and defines a measure $d_{i\mathrm{B}}$ for each particle,

$$d_{i\mathrm{B}} = p_{\mathrm{T},i}^{2k}. \tag{1.10}$$

Here, $p_{\mathrm{T},i}$ and $p_{\mathrm{T},j}$ are transverse momenta of i-th and j-th particle, respectively. The jet radius parameter, R_{ij}, is the distance between the particles.

The algorithm then finds a minimum in the two sets: $\min\{d_{ij}\}$ and $\min\{d_{i\mathrm{B}}\}$. If $\min\{d_{ij}\} < \min\{d_{i\mathrm{B}}\}$, then i-th and j-th particles are recombined, else i is the final jet and is removed from the sample. The algorithm then starts calculating d_{ij} and $d_{i\mathrm{B}}$ again and repeats all steps until all particles are used. Clustering algorithms were shown to be infrared and collinearly safe.

The clustering algorithm is determined by a predefined value k. For $k = 1$, the algorithm is called k_t algorithm [25, 26], $k = 0$ is called Cambridge-Aachen algorithm [27, 28] and $k = -1$ is the anti-k_t algorithm [24]. The k_t algorithm has the longest history and was the main jet finding algorithm, for instance, at the Large electron-positron collider. It starts the recombination from the soft particles first. Cambridge-Aachen algorithm does not include the p_{T} of particles in the distance measure, and as a result, it clusters based only on the spatial position. The anti-k_t algorithm is the youngest of the three and produces jets

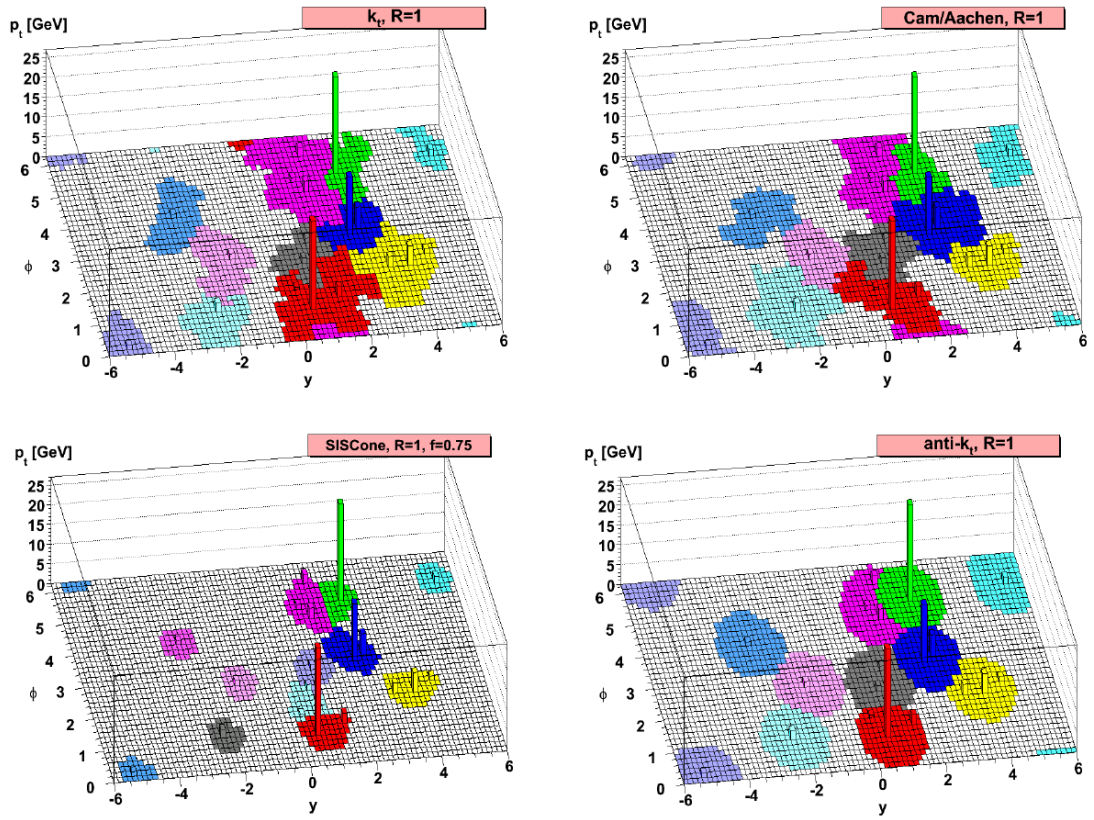

Figure 1.4: Different jet shapes for different jet algorithms. Figure is taken from [24].

with the most conical shape and is colinear and infrared safe. In a sense, it is a perfect cone algorithm. The anti-k_t algorithm starts clustering from the hard particles. Figure 1.4 shows a comparison of four various algorithms and the jets they produce. The anti-k_t is the standard jet finding algorithm at the ATLAS detector and is used to construct all jets in this thesis.

The recombination of two particles is defined by a *recombination scheme*, which specifies how to add their four-vectors. The two most important schemes are:

- E_{T} scheme: In this scheme, jets are massless, and the distance is computed as $R = \sqrt{(\Delta\eta)^2 + (\Delta\phi)^2}$. When combining two particles, the scheme adds their E_{T}, η, and ϕ. The scheme was used at Tevatron [29].

- four-momentum scheme: This scheme uses massive jets, and the distance is defined as $R = \sqrt{(\Delta y)^2 + (\Delta\phi)^2}$. The recombination process sums the 4-momenta of the particles. The scheme is used at the LHC.

Until now, we have used a word particle for the inputs to the jet-finding algorithms. This is only partially correct — the input can be many different objects, for instance, tracks of charged particles, calorimetric clusters, and particles as well. Different inputs have various advantages or disadvantages. For example, tracks are objects with a good resolution but are slow to calculate and contain only charged particles. Because neutral particles make up about 30% of the particles inside the jet, they will be missing in the track jets. On the other hand,

calorimeter cells or their clusters are very fast and contain neutral particles. Another essential difference between track and calorimeter jets is that the resolution of track jets decreases with p_{T} but increases with p_{T} in for calorimeter jets.

For a real measurement, jets must be calibrated for each individual detector. This calibration requires a proper simulation of jet showering and the showers' interaction inside a detector. Chapter 4 presents the jet reconstruction procedure used in ATLAS heavy-ion collisions in greater detail.

2. Heavy-Ion Collisions

In the last few decades, physicists have been accelerating particles to higher and higher energies and studying their collisions. During collisions of heavy ions, physicists discovered a new form of matter consisting of quasi-free quarks and gluons, which was present in the early stages of the evolution of the universe. This chapter provides a brief introduction to these collisions, supported by selected recent experimental observations.

In Figure 2.1 (left), two accelerated nuclei colliding with each other are depicted in the laboratory frame of reference. Each nucleus is Lorentz contracted into a thin disk in the direction of travel. For a Pb nucleus in the LHC, the disk has a height of about 14 fm [30] and a thickness of $14/\gamma$ fm, where the γ factor is about 2600 for $\sqrt{s_{\mathrm{NN}}} = 5.02$ TeV. The colliding discs are made of nucleons, which consist of quarks and gluons, commonly called partons. There are thousands of soft parton-parton interactions (soft means interaction with low momentum transfer). The multiplicity of these soft interactions can get as high as 30 thousand per nucleon-nucleon collision. Particles created in these soft collisions create a hot and dense medium called *quark-gluon plasma* (QGP). The γ factor has a non-trivial impact on the collision, as the two disks are shrunk more for higher γ, which increases the density of parton interactions [31].

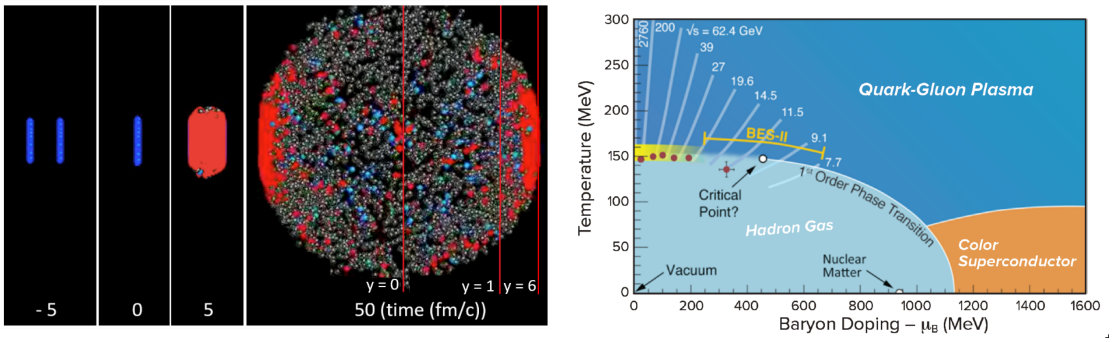

Figure 2.1: Left: Cartoon of an ultrarelativistic heavy-ion collision at different times. From left, 5 fm/c before the collision, two Lorentz contracted nuclei are shown in blue. Next, the moment when nuclei hit each other, followed by the creation of QGP. The last cartoon 50 fm/c after the collision is freeze-out — grey spheres represent hadrons. Right: A QGP phase diagram showing a region of hadrons and QGP. A potential critical point and first-order phase transition line are drawn as well. For very high baryon densities and low temperatures, we expect the formation of cold nuclear matter, which is supposed to be a color superconductor. This matter may also be found in the centers of neutron stars. Both figures are taken from [30].

The energy density right after the collision, say 1 fm/c, when the remnants of two nuclei are 2 fm apart, is much larger than a typical hadron energy density. The overlapping time of high-energy two nuclei is very short. Therefore, all secondary particles are created in a thin disk between the receding nuclei. The volume-averaged energy density inside this disk at formation time, τ_{form}, can be

estimated using the Bjorken energy density formula [2, 32, 33]:

$$\varepsilon_{\mathrm{BJ}}(\tau_{\mathrm{form}}) = \frac{1}{A}\frac{1}{\tau_{\mathrm{form}}}\frac{\mathrm{d}E_{\mathrm{T}}(\tau_{\mathrm{form}})}{\mathrm{d}y}, \tag{2.1}$$

where A is the overlap of the two nuclei in the transverse plane with respect to nuclei velocity, and $\mathrm{d}E_{\mathrm{T}}/\mathrm{d}y$ is transverse energy density per unit rapidity. In Refs. [33, 34], $\varepsilon_{\mathrm{BJ}}(\tau_{\mathrm{form}} = 1\ \mathrm{fm})$ was measured to be at least 12 GeV for the most central Pb+Pb collision at $\sqrt{s_{\mathrm{NN}}} = 2.76$ GeV at the LHC. This is much more than an energy density inside a proton, which is about $938\mathrm{MeV}/((4/3)\pi(1\mathrm{fm}^3)) \approx 250\ \mathrm{MeV/fm}^3$ [35]. In these conditions, quarks and gluons cannot be bound in their colorless states but are freed from nucleons. Because they carry a color charge, they interact with each other strongly. The medium they create is strongly coupled and has a strong collective movement [36, 37]. It flows as a relativistic fluid with the viscosity to entropy ratio η/s [38, 39], the lowest ever observed. As this medium cools down, the quarks and gluons hadronize and can be observed. The imprint of the medium can be studied using these final products.

An open question is a description of a transition between the QGP and hadronic matter. Figure 2.1 (right) shows a temperature to baryon doping phase diagram of the QGP. Baryon doping is an excess of quarks over anti-quarks and can be expressed as baryochemical potential μ_{B}. The matter with equal quantities of quarks and anti-quarks is represented by $\mu_{\mathrm{B}} = 0$. The μ approaching zero is achieved in ultrarelativistic heavy-ion collisions at the LHC. The $\mu = 0$ is achieved in the early universe. To map the whole phase diagram, we need data with higher values of baryochemical potential, which can be done by lowering the collision energy — this is being done, for instance, at Relativistic Heavy Ion Collider (RHIC) [40]. RHIC is a particle accelerator dedicated to heavy-ion collisions, operating at Brookhaven National Laboratory. A big focus is put on establishing if there is the first order phase transition and a search for the critical point between the QGP and hadronic states. Confirming or ruling out the first-order phase transition can help us understand the transition of the universe in its early stages, which was mainly the QGP, to the preset baryonic state.

The two nuclei do not necessarily have to hit head-on, meaning that not all nucleons in the nuclei must interact in the collision. The overlap can and will vary from collision to collision. Only the nucleons in the overlap participate in the collision and are called *participants*. The quantity of created QGP is proportional to the overlap between them — that is, more overlap means more interacting partons and a bigger droplet of the QGP [16]. The nucleons that do not interact are called *observers*. These observers will travel down the beam pipe with almost unaltered momentum. A special case is an *ultra-pheripheral collision*, where the colliding nuclei miss each other completely. In these collisions, nuclei can still interact via an electromagnetic interaction. It was in these collisions that the first $\gamma\gamma$ scattering via QED box-diagram was observed [41].

Another interesting property of the QGP medium is its hydrodynamics, flow, and collective movement of its constituents. An asymptotically free theory is expected to have weakly coupled constituents at very high energies. However, this is not seen. A strong coupling is observed between quarks and gluons. An example of collective motion can be seen in Figure 2.2 (left), where azimuthal correlations are observed in energies deposited in the calorimeter as measured

by the Compact Muon Solenoid (CMS) [42] experiment. Correlations are seen for particles with different rapidities, and by causality, their origin must come from the early stages of the collision. These early collective motions are then imprinted into the final hadrons we observe. Relativistic hydrodynamics simulations show that the medium behaves like a liquid with remarkably low viscosity. A good way to visualize this is: Collided nuclei are not perfect spheres. Their mass distribution is certainly not constant, and their shape is a little lumpy as well. Therefore, it is expected that pressure gradients are present right after the medium is created. Should the medium be gas-like (constituents rarely interacting), any initial anisotropy in the pressure would soon fade out, and no azimuthal correlations will be observed. Should the medium behave as a liquid with higher viscosity, any pressure-driven currents would also stop. Therefore, a low-viscosity, strongly-coupled medium is a very coherent picture. We can say that hydrodynamics converts spatial anisotropy into momentum anisotropy.

To quantify the azimuthal anisotropy, the azimuthal angular distribution of produced particles is expanded in Fourier transformation [43, 44]:

$$\frac{\mathrm{d}N}{\mathrm{d}\phi} \propto 1 + 2\sum_{n=1}^{\infty} v_n \cos\Big(n(\phi - \Psi_n)\Big), \tag{2.2}$$

where ϕ is an angle of a particle in the transverse plane and Ψ_n is the event plane angle [44, 45]. The event plane is calculated for each event so that, on average, particles having its direction lose less energy. Such particles are called in-plane. Particles going perpendicular to the event plane are then called out-of-plane. The v_n are anisotropic flow coefficients, and they are what is usually reported in experiments. These coefficients are usually measured differentially in particle pseudorapidity (η), particle-transverse momentum (p_{T}), and different colliding nuclei overlap (centrality). The most studied flow coefficient is that of the second order — ν_2 and is called *eliptic flow*. This eliptic flow is susceptible to the initial asymmetry of the eliptic-shaped overlap between the two nuclei. The higher order flow coefficients ($n > 2$) are sensitive, e.g., to viscous effects of the QGP and fluctuations of the initial-stage geometry [43, 44, 46].

Figure 2.2 (right) shows six azimuthal flow coefficients as a function of particle transverse momentum for the mid-centrality region. A typical trend for the flow coefficients is seen: increasing values with p_{T} up to $p_{\mathrm{T}} \approx 3 - 4$ GeV and then decreasing with p_{T}. A non-zero v_n coefficients are the direct evidence of the angular anisotropies, a remnant of the initial geometry. Different measurements at RHIC [47, 48] in Au+Au collisions, and at LHC [45, 49, 50, 51] in Pb+Pb collisions have shown that these coefficients are independent of the collision energy when compared in the comparable centrality intervals.

Rarely a hard collision with high energy transfer occurs between two partons. This process creates high-energetic quarks or gluons with energies reaching up to 1 TeV at the LHC. Each of these products radiates and creates a collimated shower, or jet, in the direction of its travel. The creation and evolution of this shower in a vacuum is well understood in perturbative QCD. In a heavy-ion collision, this shower must propagate through the QGP. As it plows through, it interacts with the medium and loses energy and momentum. What is lost in the jet is deposited in the QGP droplet, creating a medium response — a wake. The main work of this thesis is to investigate and further understand this energy loss.

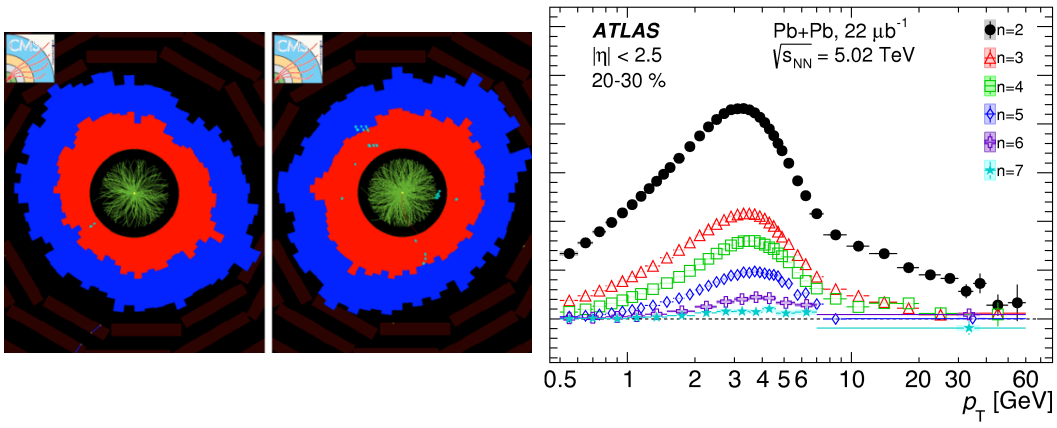

Figure 2.2: Left: An event display showing energy deposited in CMS electromagnetic (blue) and hadronic (red) calorimeter for two heavy-ion collisions. An apparent azimuthal anisotropy is seen in these events. Right: The distribution of six different ν_n azimuthal flow coefficients as the function of particle p_{T} in Pb+Pb collisions measured by the ATLAS experiment. Figure is taken from [52].

We will return to these hard scatterings and how we measure them in Sec. 2.3.

2.1 Glauber Model

In the 1950s, Roy Glauber introduced a formalism to study the scattering of composite objects at large energies [53]. His work was reviewed and updated to suit the modern need for high-energy nucleus-nucleus collisions [16, 54]. This model calculates geometric quantities in the heavy-ion collisions, namely the impact parameter — b, number of participating nucleons — N_{part}, and number of binary collisions — N_{coll}.

Glauber model assumes an optical limit approximation — fast and energetic nucleons in the colliding nuclei will be undeflected as the two nuclei pass through each other. The model sees the nucleons in the nucleus move independently of each other; that is, in the time of the collisions, they all move in the linear path. Consider a situation shown in Figure 2.3. Nucleus A and nucleus B are about to collide with an impact factor b. The cylindrical flux at a distance $\mathbf{s}$ from the center of nucleus A is shown in grey. The probability to have a nucleon in the nucleus A at the position $\mathbf{s}$ is $T_{\mathrm{A}} = \int \rho_{\mathrm{A}}(\mathbf{s}, z_{\mathrm{A}}) dz_{\mathrm{A}}$, where $\rho_{\mathrm{A}}(\mathbf{s}, z_{\mathrm{A}})$ is a probability per unit volume to find a nucleon in the grey cylinder. The analogous probability can be calculated for nucleus B. $T_{\mathrm{A}}(\mathbf{s})T_{\mathrm{B}}(\mathbf{s}-\mathbf{b})\mathrm{d}^2\mathbf{s}$ is then joint probability per unit area that two nucleons of the opposing nuclei will be in the area $\mathrm{d}^2\mathbf{s}$. Integrating over all possible values of $\mathbf{s}$ one gets the *nuclear thickness function* $T_{\mathrm{AB}}(\mathbf{b})$:

$$T_{\mathrm{AB}}(\mathbf{b}) = \int T_{\mathrm{A}}(\mathbf{s})T_{\mathrm{B}}(\mathbf{s}-\mathbf{b})\mathrm{d}^2\mathbf{s}. \tag{2.3}$$

The product $T_{\mathrm{AB}}(\mathbf{b})\sigma_{\mathrm{inel}}^{\mathrm{NN}}$, where $\sigma_{\mathrm{inel}}^{\mathrm{NN}}$ is the cross-section of the inelastic nucleon-nucleon scattering, gives the probability of the nucleon-nucleon interaction. Because the elastic collisions result in a very low energy losses, they are not considered in the Glauber-model calculations.

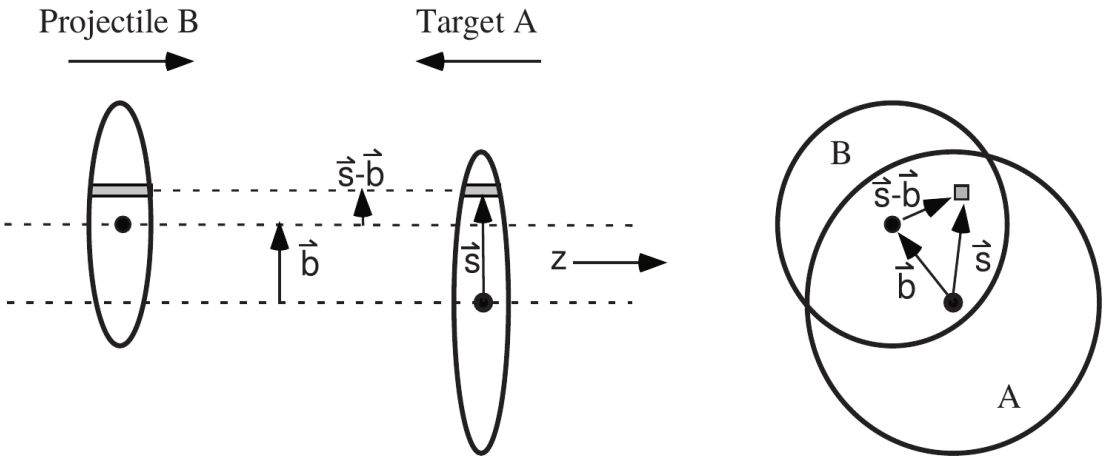

Figure 2.3: Left: Glauber model schematic view of the collisions. Right: The same collision as on the left, but along the moving nucleon. Figure is taken from [16].

The probability that n such collisions occure between nucleus A with N_{A} nucleons and nucleus B with N_{B} nucleons is given by the binomial distribution

$$\mathrm{P}(n,\mathbf{b}) = \binom{N_{\mathrm{A}}N_{\mathrm{B}}}{n}[T_{\mathrm{AB}}(\mathbf{b})\sigma_{\mathrm{inel}}^{\mathrm{NN}}]^{n}[1-T_{\mathrm{AB}}(\mathbf{b})\sigma_{\mathrm{inel}}^{\mathrm{NN}}]^{N_{\mathrm{A}}N_{\mathrm{B}}-n}. \tag{2.4}$$

With n binary (nucleon-nucleon) collisions, we have $N_{\mathrm{A}}N_{\mathrm{B}} - n$ misses. Now, all necessary factors can be calculated very easily. The total number of binary collisions is

$$N_{\mathrm{coll}}(\mathbf{b}) = \sum_{n=1}^{\mathrm{AB}} n\mathrm{P}(n,\mathbf{b}) = N_{\mathrm{A}}N_{\mathrm{B}}T_{\mathrm{AB}}(\mathbf{b})\sigma_{\mathrm{inel}}^{\mathrm{NN}}, \tag{2.5}$$

The number of nucleons in both nucleus A and B which interact with at least one nucleon from the other nucleus is called the *number of participants* N_{part}, and is equal to:

$$N_{\mathrm{part}}(\mathbf{b}) = N_{\mathrm{A}}\int T_{\mathrm{A}}(\mathbf{s})\Big\{1-\Big[1-T_{\mathrm{B}}(\mathbf{s}-\mathbf{b})\sigma_{\mathrm{inel}}^{\mathrm{NN}}\Big]^{\mathrm{B}}\Big\}\mathrm{d}^2\mathbf{s}+ \tag{2.6}$$

$$N_{\mathrm{B}}\int T_{\mathrm{B}}(\mathbf{s}-\mathbf{b})\Big\{1-\Big[1-T_{\mathrm{A}}(\mathbf{s})\sigma_{\mathrm{inel}}^{\mathrm{NN}}\Big]^{\mathrm{A}}\Big\}\mathrm{d}^2\mathbf{s}. \tag{2.7}$$

Nucleons that do not participate in the collision are called *observers* and continue traveling with unaltered momentum. Obviously, $N_{\mathrm{part}} + N_{\mathrm{obs}} = N_{\mathrm{A}} + N_{\mathrm{B}}$, where N_{obs} is the number of observers.

There are two inputs into the Glauber model. One is nucleon-nucleon inelastic cross section $\sigma_{\mathrm{inel}}^{\mathrm{NN}}$, and the other is the nucleon density, described by a Wood-Saxons distribution [55]:

$$\rho(r) = \rho_0\frac{1+w(r/\mathrm{R})^2}{1+\exp\Big(\frac{r-\mathrm{R}}{a}\Big)}, \tag{2.8}$$

where R is the radius of the nucleus and ρ_0 is nucleon density in the middle of the nucleus. Parameters a and w are corrections for skin depth and deviation from spherical shape, respectively.

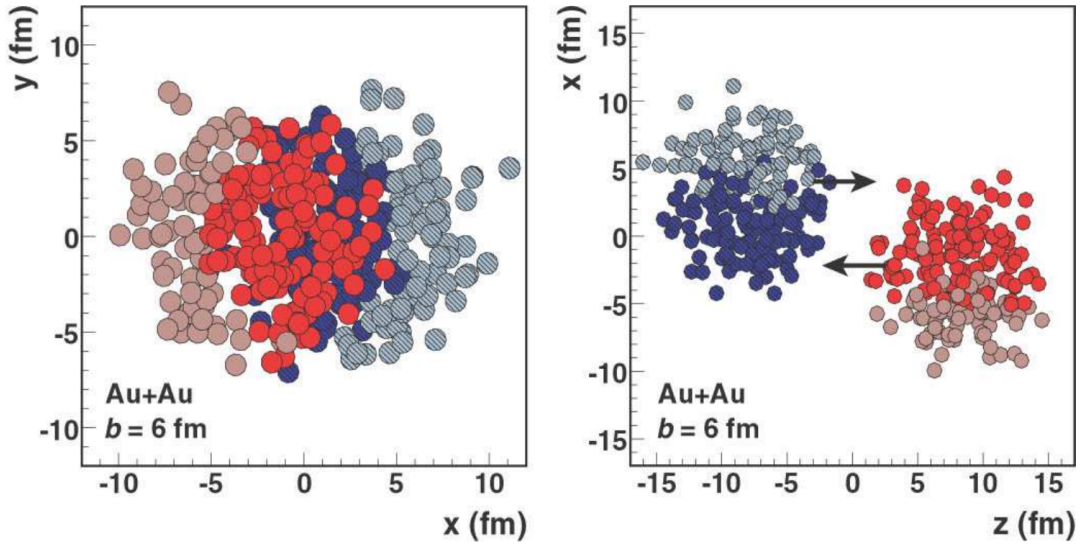

Figure 2.4: Simulation of a collision between two gold nuclei using Glauber model Monte Carlo. Darker colors denote participating nucleons, and lighter colors are observers. Left: The red nucleus is going toward us, and the blue nucleus is going away from us. Right: The nuclei go in the right-left direction, as indicated by the arrows. Figure is taken from [16].

With the use of modern computers, a Monte Carlo Glauber model is a very convenient way to calculate average values of geometric quantities. The computer randomly selects an impact factor b and assembles nucleons in both nuclei based on nucleon probability density. The collision is then viewed as a sequence of many nucleon-nucleon collisions. It is assumed that nucleons travel in a straight trajectory, independent of other nucleons or previous interactions (one nucleon can hit multiple other nucleons). In the simplest case, the two nucleons hit each other if their mutual distance d in a plane perpendicular to the beam axis is $d < \sqrt{\sigma_{\text{inel}}^{\text{NN}}\pi}$. Figure 2.4 shows a simulation of a collision of two gold nuclei. Repeating the above procedure many times, average values of $\langle N_{\text{part}} \rangle$ and $\langle N_{\text{coll}} \rangle$ can be calculated.

One has to keep in mind that there is a difference between the Glauber model and the MC approach. This difference comes mainly from the Glaubers optical limit where the incoming nucleons see the opposite nucleus as a smooth density, while the MC generator assembles the nuclei in each collision [16].

2.2 Centrality of Collision

In an actual measurement, it is impossible to set up a collision for a particular value of the impact factor, the number of participants, or the number of binary collisions. Each collision has these randomly selected by nature. It is also impossible to determine these values after the collision. All we are left with is the debris of produced particles. Mean values of geometric quantities can be obtained from the Glauber model by mapping the selected measured distribution and the same distribution obtained from the model. This mapping can vary between experiments. Here, we will describe the approach taken by the ATLAS

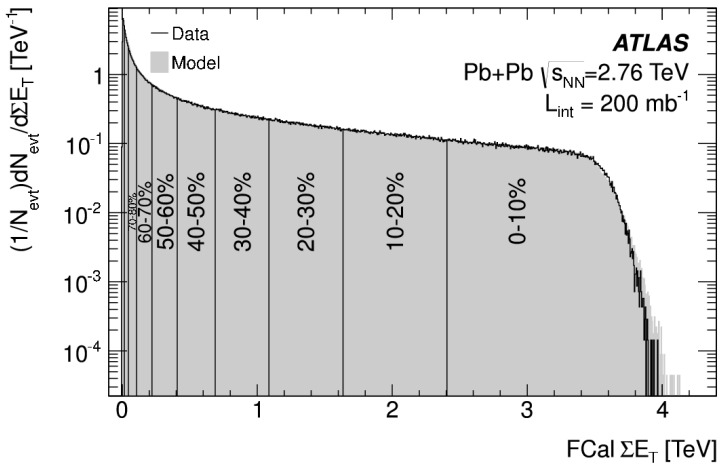

Figure 2.5: The distribution of total energy deposited in the forward region of the ATLAS detector for Pb+Pb collisions at $\sqrt{s_{\mathrm{NN}}} = 2.76$ GeV. Vertical lines indicate the centrality intervals. Figure is taken from [45].

experiment.

The number of participating nucleons N_{part} is monotonically proportional to the energy deposited in the forward regions of the detector ($3.2 < |\eta| < 4.9$) [16]. Figure 2.5 shows the distribution of the total energy deposited in this forward region per event. This distribution is calculated after we have all the collisions measured. The distribution is divided into intervals based on their fraction of the total integral. Intervals representing certain fractions are called *centrality intervals*. A centrality interval of a total size of 10% (e.g., $0 - 10\%$) contains 10% of all collisions but with a specific range of energy deposited in the forward region. In the MC Glauber model, we generate many collisions and produce the same distribution, again with its own centrality intervals. Then, we can connect the geometric quantities in the same centrality intervals between the data and the MC. It is important to note that interval starting with zero (e.g., 0–10%) contains the most central collisions, that is, collisions with the biggest mutual overlap and the smallest impact factor. On the other side of the spectrum are *peripheral collisions*, where the overlap between the nuclei is not very large — these are represented typically by $60 - 80\%$ centrality interval.

2.3 Jet Quenching

High p_{T} objects created in the hard scattering can be used as probes for studying the medium properties. Jets, charmonia, or bottomia, known as *hard probes*, can be used for this purpose. Unless stated otherwise, we will reserve our arguments in this section to jets. To quantify the effect of the QGP, a simple counting of jets can be used. As was seen in Glauber model calculations, on average, N_{coll} binary scatterings take place during a heavy-ion collision. Therefore a natural observable to investigate a potential change in jet production is a ratio called

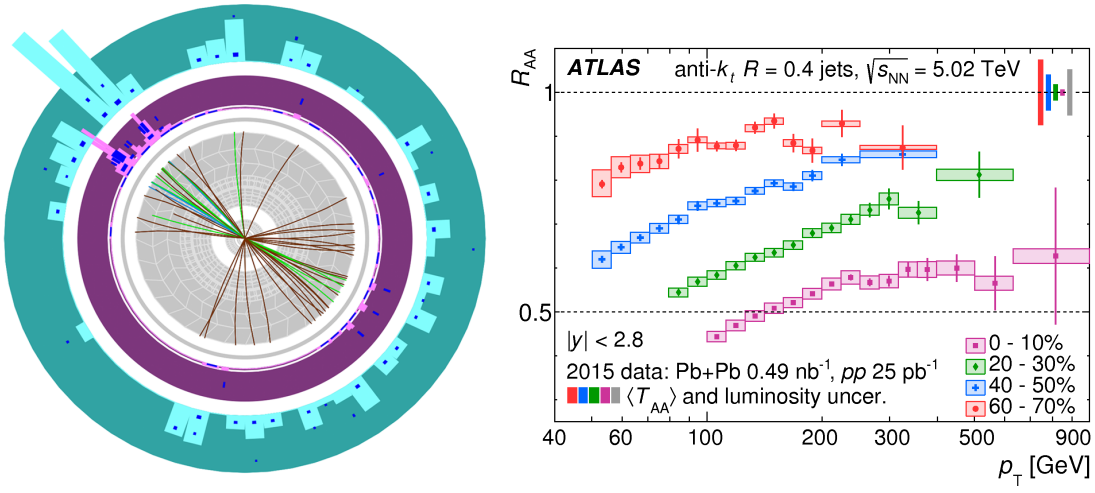

Figure 2.6: Left: Highly asymmetric event with one jet with $p_{\mathrm{T}} > 100$ GeV, but no evident recoil jet. Figure is taken from [57]. Right: Nuclear modification factor R_{AA} as a function of inclusive jet p_{T} for four centrality intervals in Pb+Pb collisions at $\sqrt{s_{\mathrm{NN}}} = 5.02$ TeV as measured by the ATLAS experiment. Figure is taken from [5].

nuclear modification factor R_{AA} defined as:

$$R_{\mathrm{AA}} = \frac{\left.\frac{\mathrm{d}N}{\mathrm{d}p_{\mathrm{T}}}\right|_{\mathrm{AA}}}{N_{\mathrm{coll}} \times \left.\frac{\mathrm{d}N}{\mathrm{d}p_{\mathrm{T}}}\right|_{pp}}, \tag{2.9}$$

where $\mathrm{d}N/\mathrm{d}p_{\mathrm{T}}$ are per-event yields of jets in an indicated system. If no QGP was formed, R_{AA} would be unity, and one heavy-ion collision would be equal to N_{coll} pp collisions. Because jets have a steeply falling spectrum in the order of approximately p_{T}^{-5} at the LHC, a significant deviation of R_{AA} from unity is expected for even a small energy loss [56].

Figure 2.6 (right) shows a measurement of the nuclear modification factor R_{AA} for jets in Pb+Pb collisions at $\sqrt{s_{\mathrm{NN}}} = 5.02$ TeV. Clearly, R_{AA} is below unity for all centrality intervals. This leads to the conclusion that a heavy-ion collision cannot be interpreted as a superposition of proton-proton collisions, and suppression of jet yields is present. This suppression of jets is called *jet quenching*. In the same figure, the R_{AA} is measured for different centrality intervals; not only do we see $R_{\mathrm{AA}} < 1$ for all of them, but a clear hierarchy can be seen — the more central collision we have, the smaller the R_{AA} is. This is a result of different amounts of QGP created in different centrality intervals. The droplet size increases with the increased overlap of the nuclei, and thus, more central collisions are expected to show larger suppression. Jet suppression is also observed in other LHC experiments, for instance, in Refs. [58, 59].

A crucial check is to look at the nuclear modification factor for colorless particles, where $R_{\mathrm{AA}} = 1$ is expected. Figure 2.7 shows two ATLAS measurements: Left panel of Figure 2.7 shows scaled yields and the R_{AA} for Z boson decaying into a muon pair. The right panel of the same figure shows the R_{AA} for W boson leptonic decay. None of these interact via a strong interaction. For the Z boson, we observe a clear consistency of the R_{AA} with the unity. For W boson, the

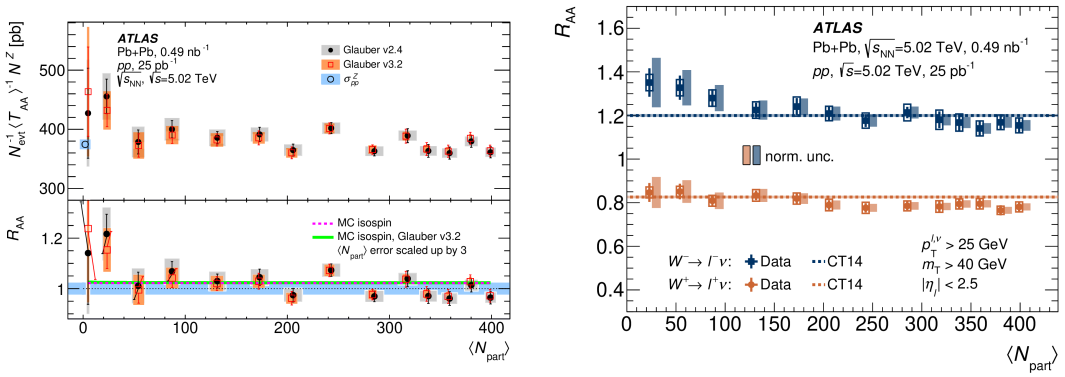

Figure 2.7: Left: Bottom panel shows the nuclear modification factor R_{AA} for Z bosons as a function of N_{part}. Right: The R_{AA} as a function of $N_{\mathrm{part}}$for $\mathrm{W}^{\pm}$ bosons. Figures are taken from [60, 61].

situation is less straightforward, as there is an uneven number of valence up and down quarks in the Pb+Pb and *pp*. This produces an *isospin effect*, where W^{+} and W^{-} production is not the same between the two systems. Nevertheless, one may conclude that no energy loss is seen for Z, W^{+}, and W^{-} bosons. Thus, these measurements established the QGP as a purely strongly interacting medium.

A jet we measure is always altered by the QGP. We do not know what would be the energy of the jet without the medium. Measuring jets recoiling against a colorless particle like γ or Z boson can help us measure the unaltered momentum of the jet. A sample with jets opposite to a high-p_{T} photon was analyzed in ATLAS γ-tagged jet measurement [62]. γ-tagged jets also provide a means to study flavor energy loss dependence. As is shown in Figure 2.8 (left), γ-jets are much more likely to be initiated by a quark than a gluon. Figure 2.8 (right) shows the nuclear modification factor R_{AA} as a function of jet p_{T} for γ-jets and inclusive jets. The γ-jets are suppressed in all p_{T} intervals, and the suppression increases with centrality. The R_{AA} of γ-tagged jets is significantly higher than that for inclusive jets in the same p_{T} and centrality interval, indicating that parton energy loss is sensitive to the color charge of the initiating parton. This is due to the fact that gluons are 2.25 times more likely to radiate in the QGP and therefore lose more energy.

The mass of the quark which initiated the jet can also play a role in the suppression. This mass dependence is described by *dead cone effect* [63], where gluon emission is suppressed in the angles smaller than quark's mass-to-energy ratio (see Figure 2.9 (left)). The effect is more pronounced for heavier quarks at the same energy. A study measuring the suppression of muons coming from heavy-flavor $\mathrm{D}(c\bar{c})$ and $\mathrm{B}(b\bar{b})$ mesons was done in Ref. [64]. The measurement of the R_{AA} indicates a significant suppression for both flavors and the suppression is increasing with the event centrality. The suppression is stronger for c quarks than for b quarks, as seen via muons at low $p_{\mathrm{T}} < 10$ GeV. This difference is quantified in their respective R_{AA} ratio shown in Figure 2.9 (right) and is due to b quark's bigger mass, which results in a more significant dead cone effect.

As was previously explained in Section 1.3, jets are constructed using a pre-defined algorithm with a pre-defined radius R. But what if the medium cannot resolve all internal structures? Figure 2.10 (left) shows the same jet but with two

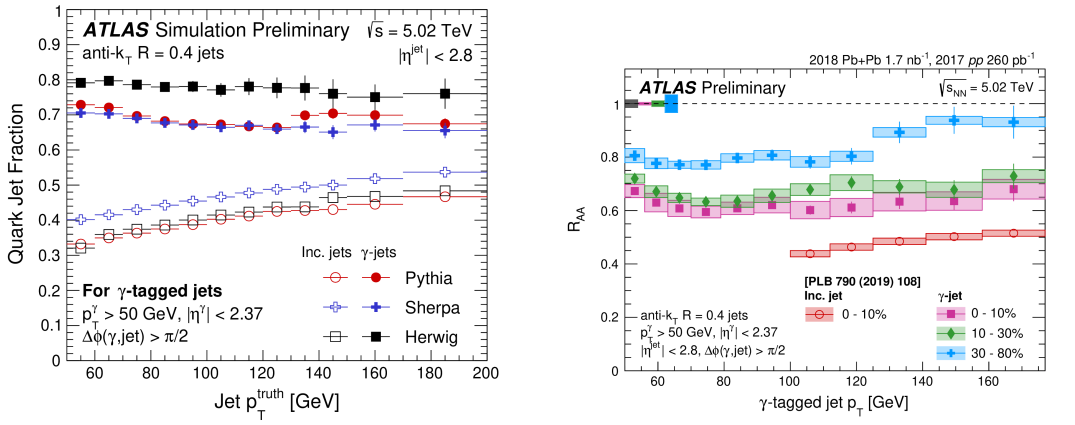

Figure 2.8: Left: Fraction of quark-initiated jets for inclusive jets (open markers) and γ-tagged jets (full markers). Right: Nuclear modification factor R_{AA} as a function of jet p_{T} for three different centralities for γ-tagged jets and inclusive jets. Figures is taken from [62].

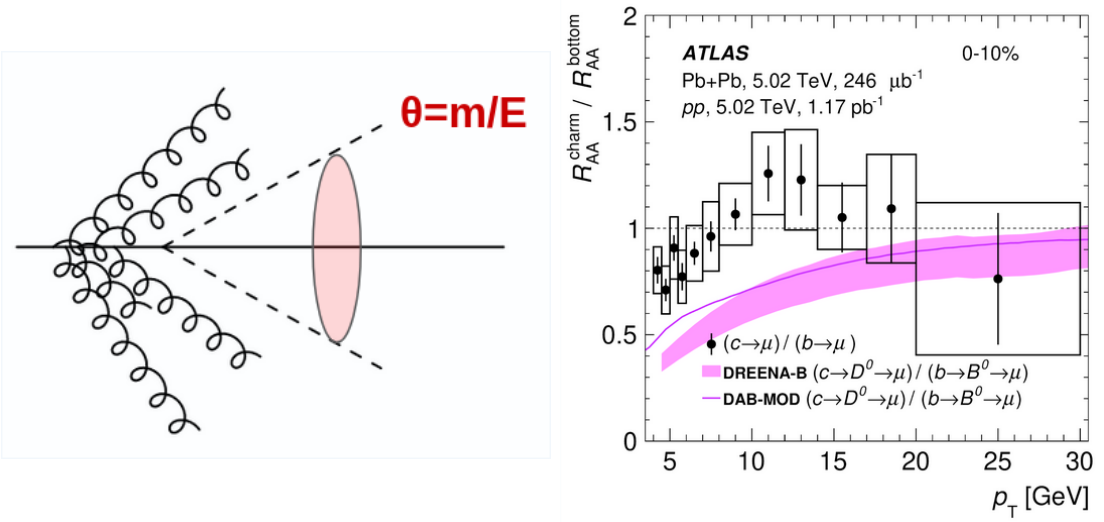

Figure 2.9: Left: Cartoon showing the dead cone effect for a quark traveling from left to right. A cone has an angle of $\theta = m/E$, where m and E are the mass and energy of the quark, respectively. Right: A ratio between the nuclear modification factor of charm and bottom quarks as a function of muon p_{T} for $0-10\%$ centrality interval. Figure is taken from [64].

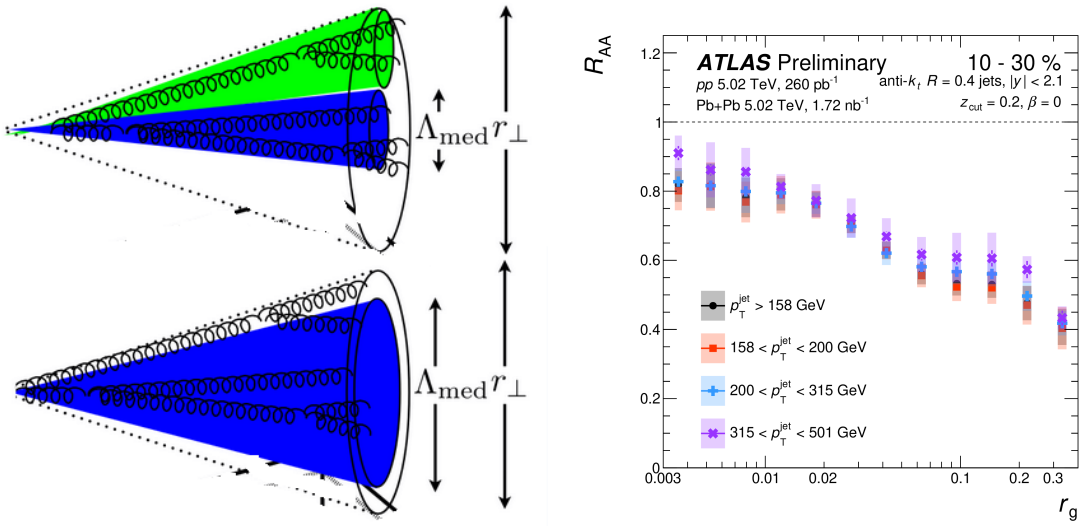

Figure 2.10: Left: Cartoon of the same jet but with different medium resolution Λ_{med}. The top figure represents a medium resolution smaller than the jet's radius, and the bottom figure shows a resolution of approximately the same size as the jet's radius. Figure is taken from [66]. Right: Measurement of nuclear modification factor as a function of r_g, for different jet p_{T} intervals and $10-40\%$ centrality. Figure is taken from [65].

different resolution scales of the medium Λ_{med}. For the top plot, the medium can resolve an internal structure of the jet and effectively sees two smaller sub-jets. For the bottom plot, the resolution is too large to identify an internal structure of a jet. In a recent ATLAS result [65], R_{AA} was studied differentially in the angle between the two sub-jets. This angle is defined as $r_g = \sqrt{\Delta\eta^2 + \Delta\phi^2}$ and the result is shown in Figure 2.10 (right). A steep r_g dependence of the R_{AA} shows that the internal structure plays an important role in the suppression — different colors represent different jet p_{T} and in each bin, they are the same within uncertainties. In general, jets with wider opening angles lose more energy than narrow jets with the same energy.

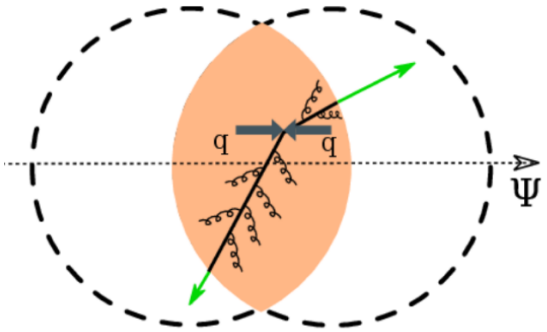

Figure 2.11: Cartoon of two jets produced in a quark-gluon plasma (orange) in an overlap of two nuclei (dashed circles). The vertex position and the non-circular shape of the overlap cause a different path length in the medium. Figure is taken from [66].

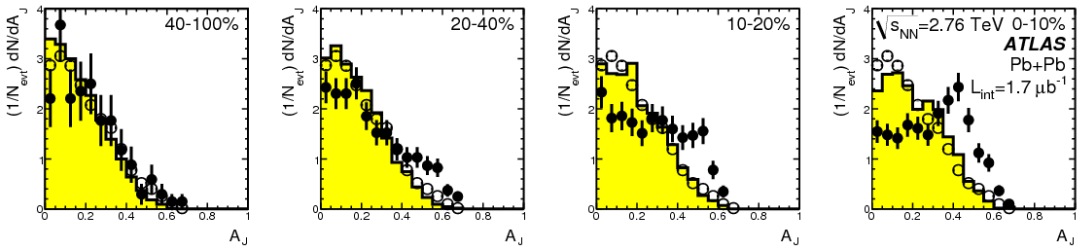

Figure 2.12: A dijet asymmetry A_J distributions for four different Pb+Pb centrality intervals. Full markers represent Pb+Pb data measured at $\sqrt{s_{NN}} = 2.76$ TeV and open markers are pp data at $\sqrt{s} = 7$ TeV. The yellow histogram shows the A_J distribution from MC HIJING generator. Figure is taken from [57].

2.4 Dijet Balance Measurements

Jets are primarily produced in back-to-back pairs (dijets) in $2 \to 2$ processes. The most likely situation in a vacuum is that the two jets in the dijet system have the same energy. This balance can be slightly violated by higher-order processes. Figure 2.11 (left) shows two jets produced in the overlap of two nuclei. In theory, the vertex from where the two jets originate does not have to be in the middle of the QGP droplet, and the dijet system can have any direction. The two jets will therefore have different path lengths in the medium. Studying the dijet system can provide more information about the dependence of path length on energy losses and the role of fluctuations in the medium.

The first dijet balance measurement in heavy-ion collisions at ATLAS was published in 2010 in Ref. [57]. In that measurement, a pp and Pb+Pb sample at a collision energy of 2.76 TeV per nucleon were compared in different Pb+Pb centrality intervals. The study focused on jet pairs in the opposite hemispheres, with an azimuthal separation of $\Delta\Phi > \pi/2$. One jet is the highest transverse energy (E_T) jet in the event, called the leading jet, and the second jet is the second highest E_T jet, called the subleading jet. The analysis measured dijet asymmetry, defined as:

$$A_J = \frac{E_{T,1} - E_{T,2}}{E_{T,1} + E_{T,2}}, \tag{2.10}$$

where $E_{T,1}$ and $E_{T,2}$ are E_T of leading and subleading jet, respectively. The results of this measurement for pp collisions and four Pb+Pb centrality intervals are shown in Figure 2.12. In the peripheral collisions ($40-100\%$ centrality), where the smallest amounts of QGP are created, Pb+Pb distribution is similar to that in pp collisions. A different characteristic is developed for Pb+Pb distribution with increasing centrality, which indicates an increased production rate of highly asymmetric dijets. The A_J distribution broadens, shifts its mean to higher values, and in the most central collisions ($0 - 10\%$), a peak develops at $A_J \approx 0.5$. This enhancement of asymmetric dijet production pointed to a possible interpretation that a hot and dense medium causes these effects.

A subsequent measurement at the same collision energy, also in Pb+Pb collisions, was done in Ref. [14]. Here, two jets forming the dijet were separated in azimuth by $\Delta\Phi > 7/8\pi$. A cartoon depicts this situation in Figure 2.13. The

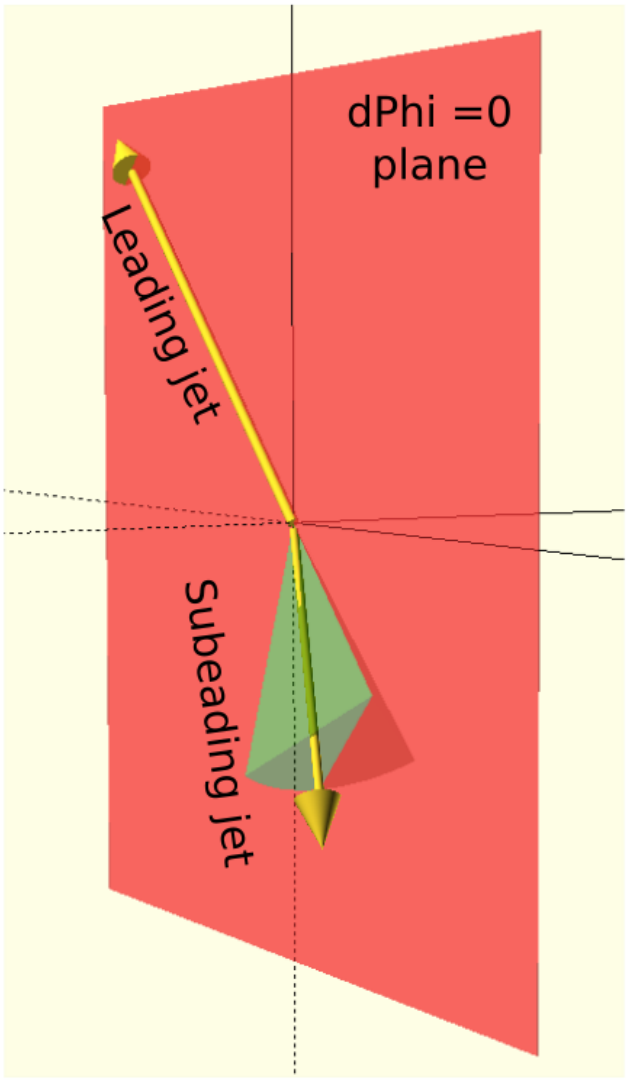

Figure 2.13: A cartoon of a dijet used in Ref. [14, 15] and Xe+Xe analysis presented in Chapter 5. The yellow arrows symbolize the leading and the subleading jet, and the green cone sector represents $|\Delta\Phi| > 7/8\pi$ region. The dijet originates at the coordinate system origin, and no QGP medium is shown.

measured quantity was dijet momentum balance x_{J}, defined as:

$$x_{\mathrm{J}} = \frac{p_{\mathrm{T},2}}{p_{\mathrm{T},1}}, \tag{2.11}$$

where $p_{\mathrm{T},1}$ and $p_{\mathrm{T},2}$ are the transverse momenta (p_{T}) of the leading and subleading jet, respectively. The x_{J} distribution was measured differentially in $p_{\mathrm{T},1}$ (in contrast to the A_{J} measurement above, where all jets with $p_{\mathrm{T},1} > 100$ GeV and $p_{\mathrm{T},2} > 25$ GeV were used). While for the dijets in pp collisions, the most frequent configuration are balanced jets with values near $x_{\mathrm{J}} = 1$, a broadening of the x_{J} distribution is observed in the Pb+Pb collisions. This broadening increases smoothly with centrality, and in the most central collisions, the x_{J} distribution develops a peak at $x_{\mathrm{J}} \approx 0.5$. Figure 2.14 (left) shows a comparison of the per-pair normalized x_{J} distribution for 0–10% Pb+Pb collisions and pp collisions for

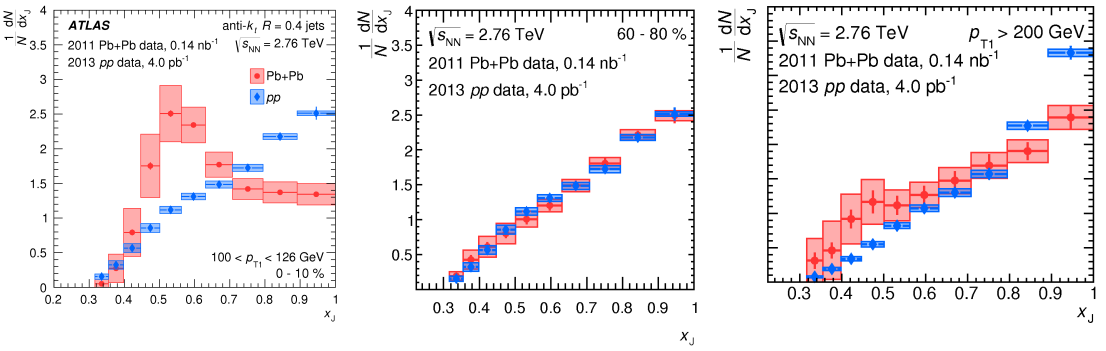

Figure 2.14: The per-pair normalized x_{J} distributions in pp (blue) and Pb+Pb (red) collisions at $\sqrt{s_{\mathrm{NN}}} = 2.76$ TeV for different centrality and $p_{\mathrm{T},1}$ selections. Left: 0–10% centrality and $100 < p_{\mathrm{T},1} < 126$ GeV. Middle: 60–80% centrality and $100 < p_{\mathrm{T},1} < 126$ GeV. Right: 0–10% centrality and $p_{\mathrm{T},1} > 200$ GeV. All figures are taken from [14].

the lowest measured $p_{\mathrm{T},1}$ interval: $100 < p_{\mathrm{T},1} < 112$ GeV. Figure 2.14 (middle) shows the same distribution as the figure on the left, but for peripheral collisions (60–80%), where pp and Pb+Pb data are consistent. With increasing $p_{\mathrm{T},1}$, the differences between the x_{J} distributions in the two systems decrease. This is compatible with the picture in which jets with higher p_{T} lose a lower fraction of their total energy. Figure 2.14 (right) shows the x_{J} distribution in the same centrality interval as the left-most figure (0–10%), but for higher $p_{\mathrm{T},1}$ interval: $p_{\mathrm{T},1} > 200$ GeV.

A similar measurement was performed in Ref. [15], where dijet balance was measured in pp and Pb+Pb collisions at $\sqrt{s_{\mathrm{NN}}} = 5.02$ TeV. The evolution of x_{J} distributions with centrality and $p_{\mathrm{T},1}$ is comparable with the previous result at $\sqrt{s_{\mathrm{NN}}} = 2.76$ TeV [14]. That is, the broadening of the x_{J} distributions is increasing with increasing centrality and decreasing $p_{\mathrm{T},1}$. Figure 2.15 (left) shows x_{J} distributions for pp collisions, and the most central (0–10%) and mid-central (40–60%) Pb+Pb collisions and for $100 < p_{\mathrm{T},1} < 112$ GeV interval.

Up to now, the x_{J} distributions were normalized by the number of dijets. In this normalization, we can only compare relative shapes between the two distributions. In the measurement published in Ref. [15] an absolute normalization was used, where yields in pp collisions were scaled by the integrated luminosity of pp collisions and Pb+Pb yields were scaled by a factor of $T_{\mathrm{AA}}N_{\mathrm{event}}$. Here, T_{AA} is the nuclear thickness function, previously defined in Section 2.1, and N_{event} is the number of events, both in the selected centrality interval. This allows a direct comparison of dijet yields between the individual Pb+Pb centralities. Figure 2.15 (right) shows absolutely normalized x_{J} distributions in pp collisions and five Pb+Pb centrality intervals for $100 < p_{\mathrm{T},1} < 112$ GeV interval. From these, it is apparent that the depletion of balance jets in Pb+Pb collisions is present in comparison with pp collisions, and this depletion increases smoothly with centrality.

In the analysis presented in Chapter 5, the momentum balance x_{J} was measured in xenon-xenon collisions. Quantifying the disbalance in a much smaller

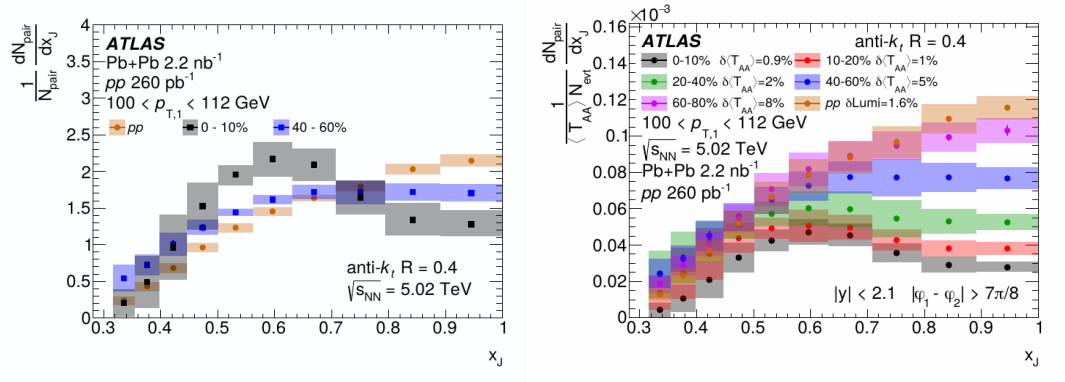

Figure 2.15: Left: The per-pair normalized x_{J} distributions for pp collisions and two Pb+Pb centrality intervals for $100 < p_{\mathrm{T},1} < 112$ GeVinterval. Right: Absolutely normalized x_{J} distribution for pp collisions and five Pb+Pb centrality intervals for $100 < p_{\mathrm{T},1} < 112$ GeV interval. All figures are taken from [15].

system and comparing it with Pb+Pb may provide additional constraints on the path-length dependence of the energy loss and the role of fluctuations.

3. Experimental setup

This thesis discusses a measurement done using the ATLAS detector — one of the main four detectors built on the Large Hadron Collider (LHC). This section describes both the accelerator and the detector itself.

3.1 The Large Hadron Collider

The Large Hadron Collider [67] (LHC) is the largest and the most powerful particle accelerator in the world. Built by the European Organization for Nuclear Research (CERN), the accelerator itself is located underground on the border between France and Switzerland. The tunnel where LHC was constructed previously belonged to the Large electron-positon collider (LEP) — its e^-e^+ predecessor. The approval for a new hadron accelerator was made in 1994 by a the CERN council (before even LEP was built), and the works began in 1998 [68]. The first circulation of the beam took place on 10th September 2008, when the very first collisions of pp were achieved. The original design was for center-of-mass energy of $\sqrt{s} = 14$ TeV and $\sqrt{s_{\mathrm{NN}}} = 5.5$ TeV[1] for pp and Pb+Pb collisions, respectively. Due to various technical faults and accidents, the energy had to be lowered for the first run.

The accelerator tunnel is placed, on average, 100 meters underground, and its circumference is approximately 26.7 km. The ring is divided into eight octants which are depicted in Figure 3.1. The circle is divided into straight and curved sections. Each of the straight sections has a specific purpose: injection, acceleration, physics experiments, beam cleaning, and beam dump. Inside the main tube, two counter-rotating rings are used to speed up the particles. Acceleration is done simultaneously on both beams by 16 radiofrequency cavities with a voltage of 2 MV and a frequency of 400 MHz. In the arc sections, particles are kept on the correct trajectory by 1232 dipole magnets, each having a magnetic field of approximately 8 Tesla. To keep the beam focused inside the vacuum chamber, 474 quadrupole magnets are installed in between the dipoles.

When the accelerated particles (protons or nuclei) are extracted from their source, they are not sent to the LHC right away. The LHC ring is the last step in a series of accelerators. The whole CERN accelerator complex is depicted in Figure 3.2. As this thesis is focused on heavy-ion collisions, we will briefly describe only the acceleration process of the nuclei. The source of Pb gives the nuclei in a partially-stripped state Pb^{27+}. These are accelerated sequentially by Linac 3, Low Energy Ion Ring (LEAR), Proton Synchrotron (PS), and Super Proton Synchrotron (SPS). Before entering the LEAR, the mass spectrometer selects Pb^{54+} ions, and right after PS, a thin aluminum foil provides the final stripping of all the electrons. From the SPS, the nuclei have an energy of approximately 450 GeV and are injected into the LHC rings in both directions.

To increase the collision rate, particles are arranged into bunches. For proton-proton collisions, there are approximately 2500 bunches per ring, with each bunch having about 10^{11} protons. In this setup, the bunch-bunch collision frequency is

[1] Collision energy for nuclei is reported as per-nucleon.

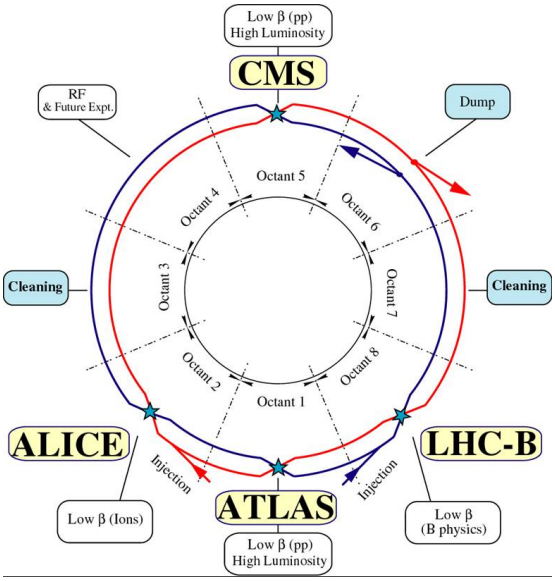

Figure 3.1: A schematics of eight LHC octant. Depicted are four main experiments along with other accelerator parts — injection, beam cleaning, acceleration, and beam dump. Figure from [69].

40 MHz. During Xe+Xe collisions, there were eight bunches per ring [70].

with a bunch-bunch collision frequency 40 MHz, that is, one bunch collision every 25 ns.

A key characteristic of a particle collider is its *instantaneous luminosity* [71]. It is defined as the ratio of the number of particles that collided — $\mathrm{d}N$ to the time period in which they were taken $\mathrm{d}t$, normalized to the process cross-section σ:

$$\mathcal{L} = \frac{1}{\sigma}\frac{\mathrm{d}N}{\mathrm{d}t}. \tag{3.1}$$

Multiplying the instantaneous luminosity by a selected process's cross-section, we get a collision rate for that process. The dimension of the luminosity in SI units is $\mathrm{s}^{-1}\mathrm{cm}^{-2}$. Integrating instantaneous luminosity over a period of time, we get *integrated luminosity*:

$$L_{\mathrm{int}} = \int \mathcal{L}\mathrm{d}t. \tag{3.2}$$

From there, the number of collisions N can be expressed as $N = \sigma L_{\mathrm{int}}$. The integrated luminosity is often reported in barns, where one barn is $10^{-28}\mathrm{m}^2$. The design luminosity for the LHC is $10^{34}\mathrm{cm}^{-2}s^{-1}$ for pp and $10^{27}\mathrm{cm}^{-2}s^{-1}$ for Pb+Pb collisions [72]. Since 2017, LHC has doubled this and held the world record for the largest instantaneous luminosity of $2.14\times10^{34}\mathrm{cm}^{-2}s^{-1}$ [73]. This record was lately broken by SuperKEKB collider [74], having $2.22 \times 10^{34}\mathrm{cm}^{-2}s^{-1}$ [75]. The future high luminosity upgrade is supposed to increase the design value of instantaneous luminosity five times and of the integrated luminosity ten times [76].

To measure the collided particles, four main experiments are situated along the LHC: A Toroidal LHC ApparatuS (ATLAS), Compact Muon Solenoid (CMS) [42], A Large Ion Collider Experiment (ALICE) [77], and Large Hadron Collider beauty (LHCb) [78].

The major success of the LHC and its experiments is the discovery of the Higgs boson [79, 80] in 2012 simultaneously by the ATLAS and CMS experiment.

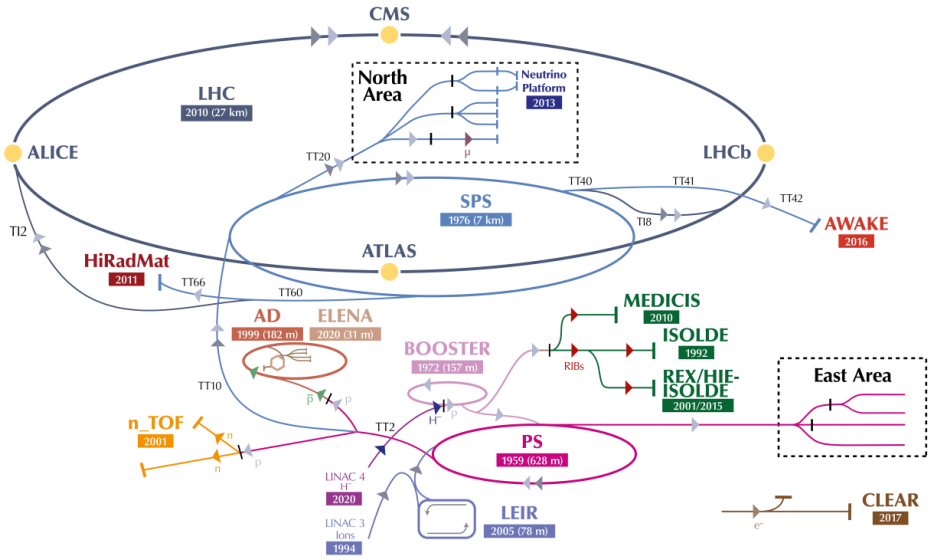

Figure 3.2: A schematic of a complex of CERN accelerators used for accelerating protons and heavy nuclei from the source to the LHC. Figure from [68].

3.2 The ATLAS Detector

A Large Toroidal LHC Apparatus (ATLAS) [72] is an all-purpose particle detector built in Interaction Point 1 (IP1). It has a cylindrical shape with azimuthal symmetry[2] with respect to the beam pipe and forward-backward symmetry with respect to the interaction point. The diameter and length of the cylinder are 25 m and 44 m, respectively. For the detector's overall view, see Figure 3.3. The detector weighs approximately 7000 tons.

The innermost part of ATLAS is called Inner Detector (ID). It is the closest part to the beam pipe and the first one to interact with the collision particles. The ID is "wrapped" by a liquid-argon (LAr) sampling electromagnetic calorimeter, covering pseudorapidity η up to 3.2 in both directions. The next part is the scintillator-tile hadron calorimeter covering $|\eta| < 1.7$. End-caps use LAr technology for both electromagnetic and hadronic calorimeters reaching up to $\eta = 4.9$. The detector ends with muon spectrometers covering $|\eta| < 2.7$. The important part of the detector is the magnetic system, bending the trajectories of particles. A superconducting solenoid encapsulates the ID, providing it with a 2 T magnetic field. Three large toroidal magnets are placed outside the calorimeters, generating a magnetic field of up to 1 T for other detector parts.

3.2.1 The Magnet System

The magnet system consists of one solenoid and three toroidal magnets, capable of storing 1.6 GJ of energy. The toroidal magnets have a central barrel with two end-caps. All the magnets are superconducting and cooled to 4.5 K by liquid

[2]ATLAS uses a right-handed coordinate system with its origin at the nominal interaction point (IP) in the center of the detector and the z-axis along the beam pipe. The x-axis points from the IP to the center of the LHC ring, and the y-axis points upward. The quantities like p_{T}, E_{T}, η, etc. are defined in the footnote in the Introduction.

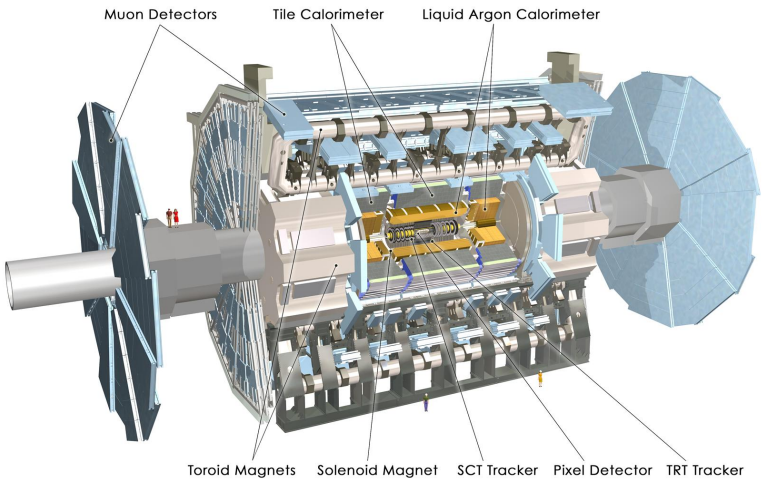

Figure 3.3: Cut-away of the ATLAS detector with its main parts: The Inner Detector, Calorimeters, Muon spectrometer, and magnet systems. Figure taken from [72].

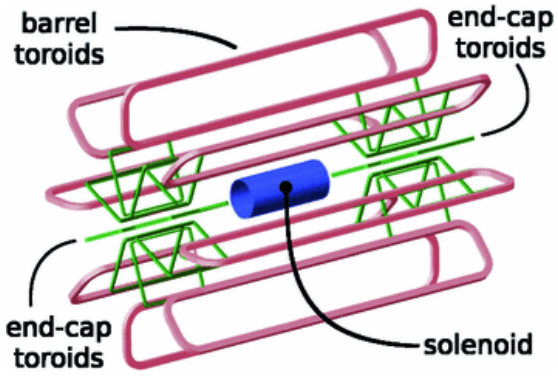

Figure 3.4: ATLAS magnet system: (blue) central solenoid, (red) central barrel toroid, and (green) two end-cap toroids. Figure from [81].

helium. A schematic of the system is in Figure 3.4.

Central solenoid is aligned with the beam axis, having 5.8 m in length and a bore of $\approx$ 2.4 m providing a central magnetic field of 2 T for the ID placed inside it. As this magnet is placed in front of the calorimeter system, an extreme minimization of material is desired. The resulting design has only 0.66 radiation length at nominal incidence. To further reduce the impact on the energy loss, it is placed in the same vacuum chamber as the LAr calorimeter. With a voltage supply of 8 kA, the solenoid is capable of storing up to 40 MJ of energy.

Barell toroid and its two end-caps are each made of 8 separate coils, installed symmetrically around the beam axis. The end-caps and the barrel are rotated by 22.5° with respect to each other. The toroid has approximately 25 meters in length, and its outer and inner diameter is 20 m and 9 m, respectively. The barrel stores energy of 1.1 GJ, and both end-caps together an additional 0.5 GJ, all powered by a 21 kA power supply. The main role of the end-caps is to generate the magnetic field required to optimize the bending power near the end-cap region.

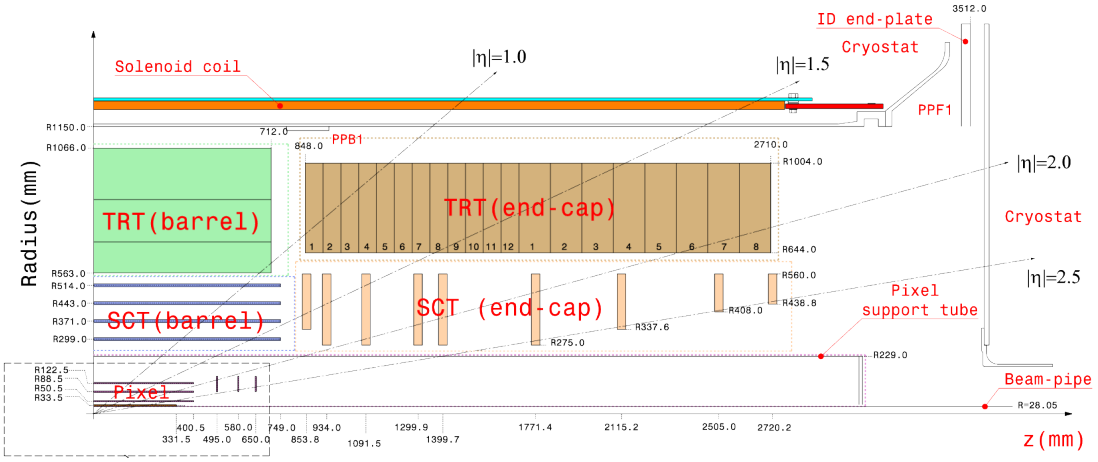

Figure 3.5: Innder Detector cross-section, showing Pixel, SCT, and TRT sub-detectors. Figure from [72].

3.2.2 Inner Detector

The Inner Detector (ID) is the innermost part of ATLAS and is the first point of detection. With over 1000 particles produced every 25 ns, the detector was designed to sustain large doses of radiation. Its main purpose is pattern recognition, primary/secondary vertices identification, and excellent momentum measurement of charged tracks with nominal minimum p_{T} threshold of 500 MeV, all within a pseudorapidity $|\eta| < 2.5$. It also provides electron identification, complementary to LAr calorimeter, over $|\eta| < 2.0$ and energies between 0.5 GeV and 150 GeV. The ID cross-section along the beam axis is shown in Figure 3.5, and a cross-section perpendicular to the beam axis is in Figure 3.6. The construction is a cylinder aligned with the beam axis and an interaction point in the middle, with dimensions 7 m in length and a radius of 1.1 m. As this detector stands in front of the calorimeter systems, minimalization of particle interaction was required. ID is divided into three main parts:

Pixel detector is the innermost part of the detector. It has a barrel part, which originally consisted of three layers. In May 2014, a fourth Insertable B-Layer (IBL) was installed between the beam pipe and the existing Pixel detector [82]. The distance of individual layers from the beam pipe is 33 mm, 50 mm, 88 mm, and 122 mm. Two end-caps consisting of three disks each are installed on both sides of the detector. The barrel and each end-cap have in total 1736 and 288 modules, respectively. These modules consist of 92 million pixels, with individual pixel sizes of 50×250 μm^2 for the IBL layer and 50×400 μm^2 for the outer layers.

SemiConductor Tracer (SCT) is the middle part of ID and can be divided into a barrel with four layers and two end-caps with nine layers each. With over 4088 two-sided modules, SCT has over 6 million readout channels. The design provides a spatial resolution of 15 μm.

Transition radiation tracker (TRT) consisting of over 370 thousand proportional drift tubes, or straws, with 4 mm in diameter. On average, a track hits 36 of these straws. This outer layer improves momentum measurements of particles and provides a calorimeter-independent electron identification. Pixel and SCT parts operate at temperatures below 0 °C, while TRT operates at room

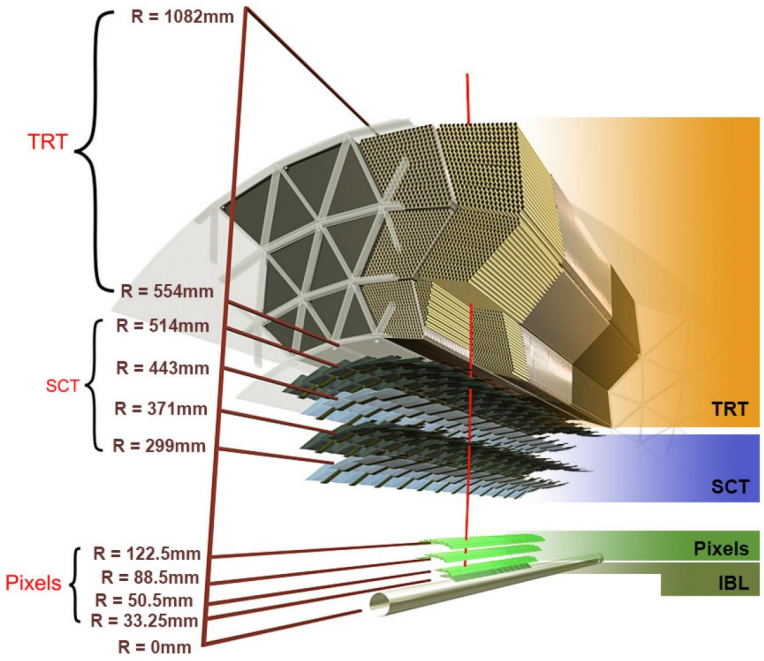

Figure 3.6: ATLAS Inner detector cut-away, showing the beam pipe and all barrel layers. Figure from [72].

temperature.

3.2.3 Calorimeters

ATLAS calorimetric systems cover the range of $|\eta| < 4.9$. The electromagnetic calorimeter has a very fine granularity to be able to do very precise measurements of electrons and photons. The other parts of the detector have a coarser granularity, however, sufficient for the required jet and $E_{\mathrm{T}}^{\mathrm{miss}}$ measurements. The cut-away of the ATLAS calorimeter system is shown in Figure 3.7. The parts of the calorimetric system are:

LAr electromagnetic calorimeter consists of a barrel with a coverage of $|\eta| < 1.475$ and two identical end-caps covering the $1.375 < |\eta| < 3.2$ range. The central barrel is split into two identical parts, 4 mm apart at $z = 0$. The accordion geometry of the layers is displayed in Figure 3.8 (left).

Tile calorimeter is a sampling hadronic calorimeter, using steel as the absorber and scintillating tiles as the active material, with a ratio of 4.7 to 1. The central barrel has a coverage of $|\eta| < 1.0$, and two symmetrically placed end-caps cover $0.8 < |\eta| < 1.7$. Both the barrel and the end caps are divided into 64 azimuthal modules. The tile's inner radius is 2.28 m and reaches up to 4.25 m. A cross-section of the tile is shown in Figure 3.8 (right).

LAr hadronic end-cap calorimeter (HEC) is positioned right outside the electromagnetic end-cap covering range $1.5 < |\eta| < 3.2$ on both sides. Each end-cap consists of two separate wheels.

LAr forward calorimeter (FCal) is covering the most forward regions of the calorimetric system for η values between 1.5 to 4.9. Two parts are positioned at each side of the detector, and each part is divided into three segments:

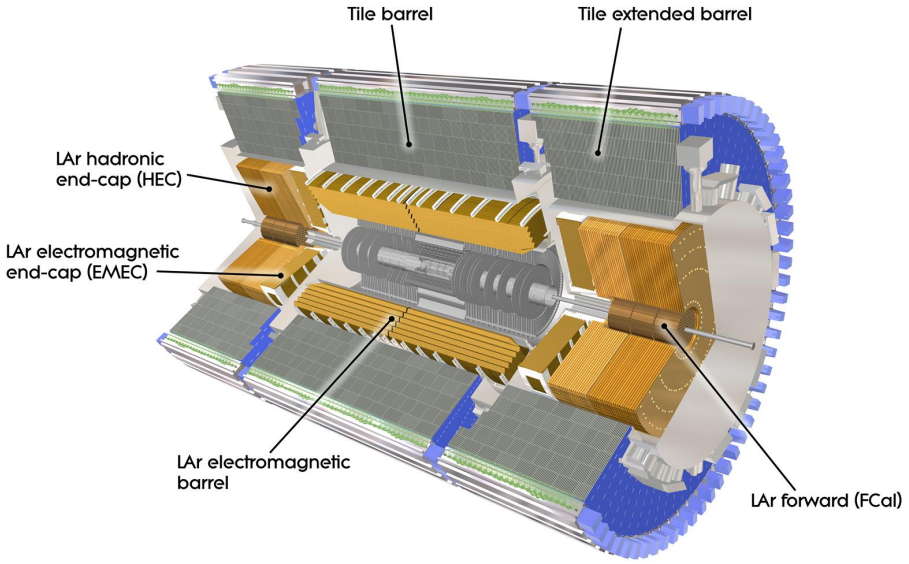

Figure 3.7: ATLAS hadron and electromagnetic calorimeter with a description of the main parts. Figure from [72].

the first one is made out of copper to be optimized for electromagnetic measurements, while the remaining two are made out of tungsten and measure dominantly hadronic interactions.

LAr forward calorimeter (FCal) is covering the most forward regions of the calorimetric system for η values between 1.5 to 4.9. Two parts are positioned at each side of the detector, and each part is divided into three segments: the first one is made out of copper to be optimized for electromagnetic measurements, while the remaining two are made out of tungsten and measure dominantly hadronic interactions.

The EM calorimeter has more than 22 radiation lengths in thickness and 9.7 radiation lengths for electromagnetic+hadronic calorimetry. This provides a good resolution for high-energy objects and lowers the punch-through limit to the muon system.

3.2.4 Muon Spectrometer

ATLAS muon spectrometer is designed to measure charged particles exiting the calorimeter system in pseudorapidity of $|\eta| < 2.7$. On top of that, it can trigger these particles within $|\eta| < 2.4$. Precise measurements of muons with momentum up to 1 TeV are highly desirable. Although the ID can measure muons as well, for high momenta and forward regions, the precision is not sufficient. The MS provides this extra level of required precision. The muon detector consists of chambers arranged in cylindrical barrels with a distance from the beam axis of 5 m, 7.5 m, and 10 m as shown in Figure 3.9. Symmetric end-caps are installed on both sides at a distance of $|z| = 7.4$ m, 10.8 m, 14 m, and 21.5 m. The resolution of muon's momentum is inversely proportional to BL^2, with B being the magnetic field and L the distance traveled. The big dimensions of the detector take advantage of this. Several service gaps are left at $\eta = 0$ to allow repairs and

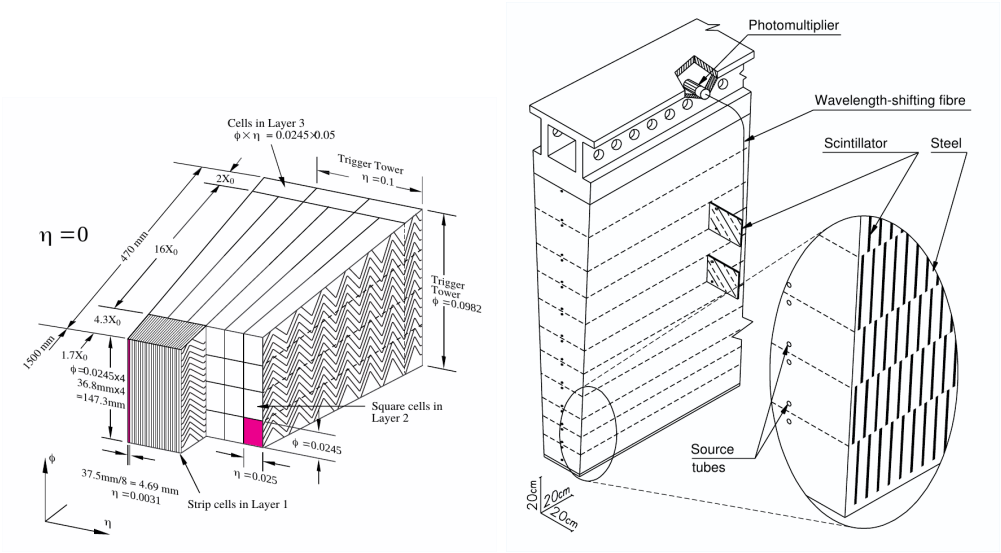

Figure 3.8: (left) A cross-section of LAr calorimeter showing its accordion structure. (right) A cross-section of a hadronic Tile calorimeter. Figure from [72].

maintenance of the inside components. The biggest gap has about 1-2 m or $|\eta| < 0.08$.

Monitor Drift Tube chambers (MDT), depicted in Figure 3.10, are used for precision-momentum measurements. These are made of several layers of drift tubes filled with Ar/CO_2 gas and tungsten-rhenium wire in the middle. A resolution on average is 80 μm per tube and 35 μm per chamber. To achieve such high precision, the position of the individual chambers must be known to 30 μm. This is achieved by a dedicated alignment optical system between the MDT chambers. However, this optical system can detect only relative changes in position. To get an absolute position of the chambers between themselves and the other parts of the detector, a track-based alignment between the ID and the muon system is used.

The innermost end-cap has Cathode-Strip Chambers (CSC) instead of MDTs in the $|\eta| > 2.0$ region. This is due to the much higher expected multiplicity, which would overwhelm the MDTs.

The muon system must be able to trigger for traversing muons. To achieve the necessary speeds required by the L1 trigger system, Resistive Plate Chambers (RPC) and Thin Gap Chambers (TGP) were installed in the barrel and end-cap region, respectively (see Figure 3.9). Tigger and MDT tracks are then matched together, providing a fast and precise measurement of muons. Another benefit of such a second independent system is the background rejection of n/γ-particles in the experimental hall.

3.2.5 Zero Degree Calorimeter

The Zero Degree Calorimeter (ZDC) [83] consists of a sampling calorimeter located 140 m from the IP symmetrically on both sides of the detector. ZDC can detect neutral particles in heavy-ion (HI), pp and pA collisions. One electromagnetic and three hadronic modules per side cover pseudorapidity interval $|\eta| > 8.3$. In HI collisions, ZDC measures primarily spectator neutrons [16] and serves as a

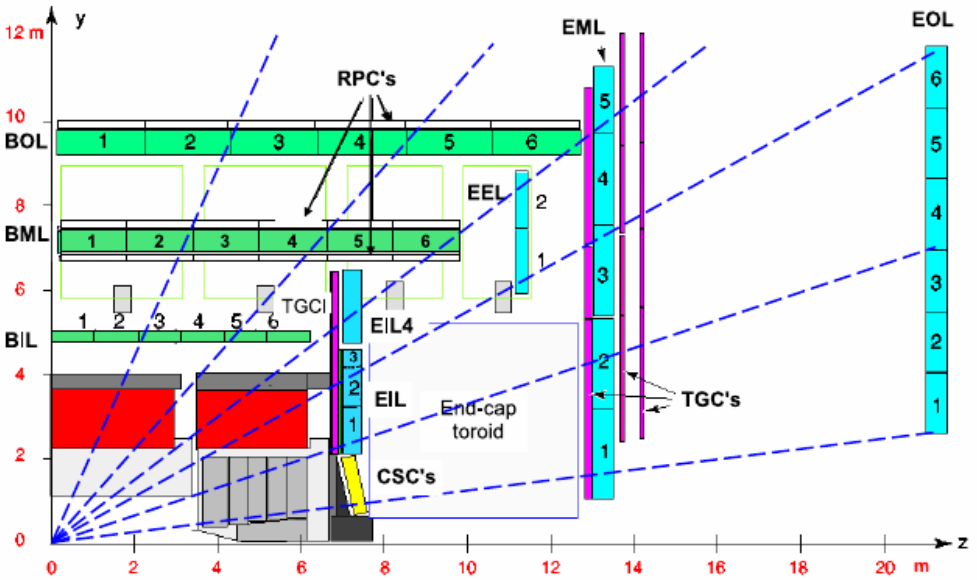

Figure 3.9: Cross section of ATLAS muon system perpendicular (left) and along (right) the beam axis. Figure from [72].

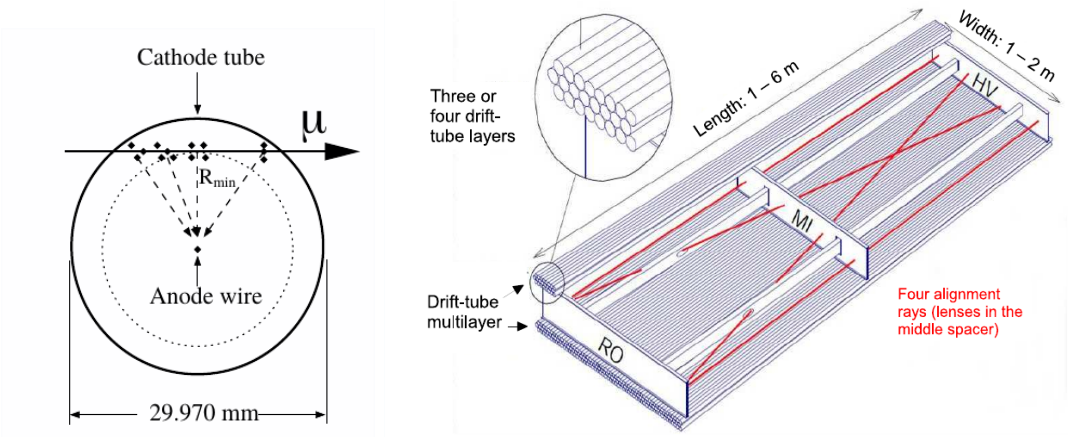

Figure 3.10: (left) MDT drift tube cross-section. Individual chambers have two multi-layers of four or three drift tubes. (right) MDT chamber with 2x3 layers of drift tubes. Red lines show laser beams of the optical alignment system. Figure taken from [72].

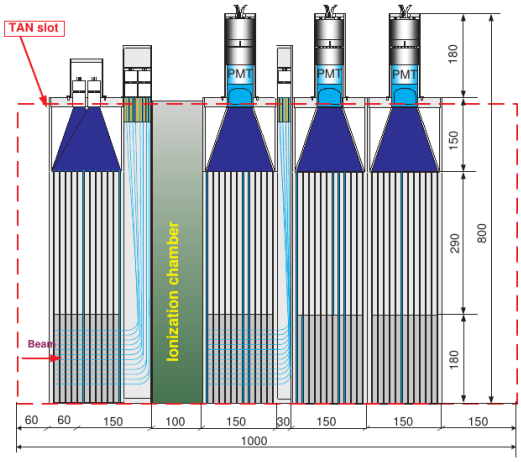

Figure 3.11: Four ZDC modules. Figure is taken from [83].

trigger, especially in ultra-peripheral collisions. Figure 3.11 shows the layout of the ZDC modules. Each module consists of eleven absorber plates located perpendicularly to the beam direction. Between the plates, vertical quartz rods are installed. Singal from these rods is read by photomultiplier tubes located above each module.

3.2.6 ATLAS Triggers and Data Acquisition

ATLAS trigger system consists of two levels [84]. The first level is called the Level-1 trigger (L1) and is implemented in the hardware of the detector. Its primary purpose is to reduce the rate of events from 400 MHz to a maximum of 100 kHz. In each event, topological trigger processors [85] combine information about multiple objects into summary-topological information. This information is used by L1 to improve the background rejection.

The second level is a software-based high-level trigger (HLT). It is used to further decrease the accepted collisions rate down to ≈1.2 kHz. Events that pass the HLT trigger are used for physical analyses. When an event passes the L1 trigger, specific HLT objects, such as jets or leptons, are reconstructed. This procedure is called online reconstruction. The events that pass the HLT trigger are written to the Tier-0 computing center at CERN and are used for physical analyses.

A trigger consists of one or more steps, and each step is encoded as a sequence algorithms. An output of each algorithm is a binary logical decision; either an event passes the trigger requirements or not. Typically, the L1 trigger identifies Regions of Interest (RoI), and each step runs reconstruction algorithms on event-data fragments in RoIs. RoI is usually a rectangular area in $\eta \times \phi$ space. The logical outputs are cached and can be requested by future steps. L1 and HLT triggers have assigned prescale value, p_{L1} and p_{HLT}, respectively. Prescale value can only be equal to or greater than one. The p_{L1} value defines the maximum number of events that pass the L1 trigger and are accepted by HLT. The p_{HLT} is the maximum number of events that pass L1 and are required to be processed by HLT. Triggers for which $p_{\mathrm{L1}} = p_{\mathrm{HLT}} = 1$ are called unprescaled. All L1 and HLT triggers are listed on a trigger menu in Ref. [84].

Minimum Bias Trigger in Xe+Xe Collisions

ATLAS used minimum bias (MB) triggers during the collection of Xe+Xe collisions data. MB trigger is a trigger that selects inelastic hadronic events with the smallest possible bias.

As the first step, L1 evaluates the total E_{T} deposited in the calorimeter, $\sum E_{\mathrm{T}}$. Based on $\sum E_{\mathrm{T}}$, the logical OR operator is used between the following two triggers:

1. `HLT_mb_sptrk_L1VTE4`: If $\sum E_{\mathrm{T}} < 4$ GeV, the HLT trigger requires at least one reconstructed track in the Inner Detector.

2. `HLT_noalg_mb_L1TE4`: If $\sum E_{\mathrm{T}} > 4$ GeV, no other condition is required.

The `TE4` part in the trigger names specify the boundary in the $\sum E_{\mathrm{T}}$. For the first seven luminosity blocks of the Xe+Xe run, the `TE4` triggers were not active and `TE5` triggers, `HLT_noalg_mb_L1TE5` and `HLT_mb_sptrk_L1VTE5`, were used instead. The `TE5` trigger has the same algorithm, but the $\sum E_{\mathrm{T}}$ cut is 5 GeV. The ZDC was not used for triggering in Xe+Xe collisions.

4. Jet Calibration

In this chapter, the calibration of heavy-ion (HI) jets is described in detail. The jet energy scale calibration restores the jet energy to that of jets reconstructed at the particle level. The process for heavy-ion jets is shown in Figure 4.1 and is slightly different from the reconstruction applied on *pp* collisions used by ATLAS. The first step is the removal of an underlying event (UE) and reconstruction of jets with an anti-k_t algorithm. This is followed by numerical inversion (NI), which calibrates jets from electromagnetic (EM) scale to generator-level scale. The last step combines in situ correction derived for jets reconstructed in 13 TeV *pp* collisions and for cross-calibration that relates the JES between the *pp* and HI style reconstructions. The procedure is the same for Pb+Pb and Xe+Xe collisions.

4.1 Jet Reconstruction

The jet reconstruction procedure described in this section is used in all heavy-ion analyses in the LHC Run 2 (2012-2017). It follows the procedure done for *pp* collisions [86] but is slightly modified for significantly higher UE that is present during heavy-ion collisions. Because UE varies event-by-event by several orders of magnitude, it is required to do the subtraction on an event-by-event basis. All heavy-ion jets are reconstructed using `FastJet` package [87] and anti-k_t algorithm [24]. As an input, the algorithm takes logical towers with a constant size of $\Delta\eta \times \Delta\phi = 0.1 \times \pi/32$. The center of each tower has an (ϕ, η) coordinate on the geometric grid, and the total transverse energy (E_{T}) in the tower is a sum of energies in the individual calorimeter cells:

$$E_{\mathrm{T}}^{\mathrm{tower}} = \sum_j w_j E_{\mathrm{T},j}^{\mathrm{cell}}, \tag{4.1}$$

where w_j is a per-cell weight that is equal to the fraction of the overlap between the cell and the tower. The positioning of the towers is selected so that most of the weights are $w_i = 1$. The exceptions are at the edges of the towers and in some layers where one cell can span across several towers.

The energy deposited in the tower contains both signal and background components:

$$\frac{\mathrm{d}^2 E_{\mathrm{T}}^{\mathrm{total}}}{\mathrm{d}\eta \mathrm{d}\phi} = \frac{\mathrm{d}^2 E_{\mathrm{T}}^{\mathrm{UE}}}{\mathrm{d}\eta \mathrm{d}\phi} + \frac{\mathrm{d}^2 E_{\mathrm{T}}^{\mathrm{signal}}}{\mathrm{d}\eta \mathrm{d}\phi}. \tag{4.2}$$

The ultimate goal is to remove the background component (denoted UE) and measure the signal with the best possible precision. The background can be factorized into an η- and ϕ-dependent components:

$$\frac{\mathrm{d}^2 E_{\mathrm{T}}^{\mathrm{UE}}}{\mathrm{d}\eta \mathrm{d}\phi} = A \times \rho(\eta) \times H(\phi) \times \lambda(\eta, \phi), \tag{4.3}$$

where $A = 0.1 \times \pi/32$ is the area of a tower,

$$\rho(\eta) = \left\langle \frac{\mathrm{d}^2 E_{\mathrm{T}}}{\mathrm{d}\eta \mathrm{d}\phi} \right\rangle$$

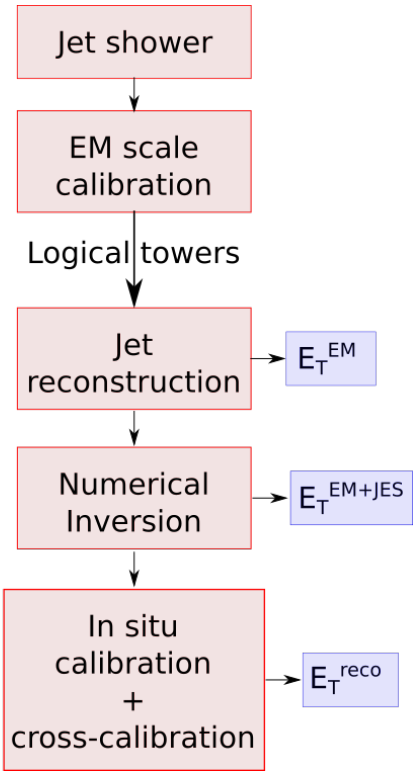

Figure 4.1: The reconstruction procedure steps for heavy-ion jets. Blue boxes show the naming of the objects that are the output of the individual steps.

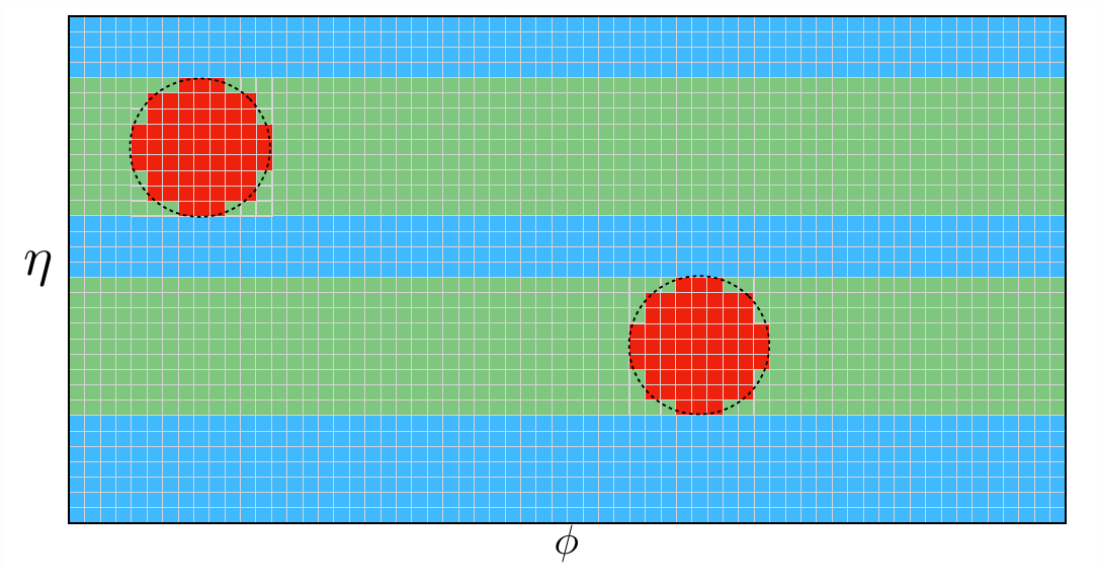

Figure 4.2: A cartoon showing an $\eta - \phi$ map of the logical towers. Towers in red are associated with jet seeds and are excluded from the calculations of all variables. Towers in green are used only for calculations of ρ, and towers in blue are used for all three ρ, ν_n, and Ψ_n. Figure is from [66].

is an average E_{T} density integrated over the whole 2π azimuth, $\lambda(\eta, \phi)$ is a correction accounting for local variations in the detector response, and $H(\phi)$ describes an azimuthal flow modulation. $H(\phi)$ can be decomposed into the following Fourier series:

$$H(\phi) \overset{\text{def.}}{=} 1 + 2 \sum_{n}^{2,3,4} \nu_n \cos\Big[n(\phi - \Psi_n)\Big], \tag{4.4}$$

where index n denotes an order of the harmonic, ν_n is the magnitude of the flow, ϕ is the azimuthal angle of the tower, and Ψ_n is an angle of a reaction plane of the collision. Because the modulation is dominated by the lowest orders, only the lowest three components are used. The highest contribution has the second harmonic ν_2 [52]. The values of ν_n and Ψ_n are defined as:

$$\nu_n \overset{\text{def.}}{=} \sqrt{\langle \sin(n\phi) \rangle^2 + \langle \cos(n\phi) \rangle^2}, \tag{4.5}$$

and

$$\Psi_n \overset{\text{def.}}{=} \frac{1}{n} \tan^{-1} \frac{\langle \sin(n\phi) \rangle}{\langle \cos(n\phi) \rangle}. \tag{4.6}$$

The averaged sin and cos values are determined by equations:

$$\langle \sin(n\phi) \rangle = \frac{\sum\limits_{|\Delta\eta|>0.4} (\frac{E_i}{\lambda_i} \sin(n\phi_i)}{\sum\limits_{|\Delta\eta|>0.4} E_i \lambda_i} \tag{4.7}$$

$$\langle \cos(n\phi) \rangle = \frac{\sum\limits_{|\Delta\eta|>0.4} (\frac{E_i}{\lambda_i} \cos(n\phi_i)}{\sum\limits_{|\Delta\eta|>0.4} E_i \lambda_i} \tag{4.8}$$

where the sums go over all towers indicated in blue in Figure 4.2. The value of ρ is determined by the equation:

$$\rho = \frac{1}{A} \frac{\sum\limits_{\Delta R>0.4} \frac{E_i H_i}{\lambda_i}}{1 - \sum\limits_{\Delta R>0.4} \frac{H_i}{\lambda_i}}, \tag{4.9}$$

and the sum goes over all towers except those indicated in red in Figure 4.2. The UE is subtracted on the level of individual towers using the following formula:

$$E_{\mathrm{T}}^{\mathrm{tower}}|_{\mathrm{subtracted}} = E_{\mathrm{T}}^{\mathrm{tower}}|_{\mathrm{total}} - \frac{\mathrm{d}^2 E_{\mathrm{T}}^{\mathrm{UE}}}{\mathrm{d}\eta \mathrm{d}\phi}. \tag{4.10}$$

To minimize the jets' self-energy bias, an iteration procedure is used. In each iteration, the following steps are performed:

1. Identify jet seeds
2. Compute ρ, ν_n, and Ψ_n using regions of the calorimeter outside the jet seeds.
3. Subtract the UE using Equation 4.10
4. Apply the energy scale calibration procedure

The three iterations are:

1. **Iteration 1**: The subtraction procedure is applied to $R = 0.2$ jet seeds, with $E_{\text{max}}/\langle E\rangle > 4$ GeV and $E\text{max} > 3$ GeV where initial values of ρ^1, ν_n^1, and Ψ_n^1 are estimated. Here, E_{max} is and $\langle E\rangle$ is . Even though the jet seeds are of radius $R = 0.2$, the exclusion region has radius $R = 0.4$.

2. **Iteration 2**: UE from iteration 1 is subtracted, and new jet seeds are identified. These seeds can be of two origins: $R = 0.2$ calorimeter jets with $p_{\text{T}} > 25$ GeV or track jets with $p_{\text{T}} > 7$ GeV[1]. ρ^2, ν_n^2, and Ψ_n^2 are estimated again.

3. **Iteration 3**: UE using new values from the previous step is subtracted, and jets with $R = 0.4$ and $p_{\text{T}} > 25$ GeV are used as jet seeds to estimate a new set of ρ^3, ν_n^3, and Ψ_n^3 quantities again.

The ρ^3, ν_n^3, and Ψ_n^3 from the last iteration are then used to subtract UE from jets of all radii.

4.2 Numerical Inversion

NI is a procedure to calibrate HI jets from the EM scale to the generator-level scale. The procedure is the same as for *pp* jets used in *pp* collisions but calibrates jets that are the results of the procedure described in Section 4.1 above. While there is no event centrality selection for *pp* and *p*+Pb jets, for the Pb+Pb jets, only the peripheral events are used since the underlying event activity is significantly smaller in these.

The central quantity used for calibration is the response:

$$\mathcal{R} = \frac{E_{\text{T}}^{\text{EM}}}{E_{\text{T}}^{\text{truth}}}, \tag{4.11}$$

where E_{T}^{EM} is reconstructed E_{T} at the EM scale, and $E_{\text{T}}^{\text{truth}}$ is the E_{T} of the truth jet from the Monte Carlo (MC) generator. The response is evaluated for all calorimeter jets differentially in p_{T} and η. All jets used to evaluate $\mathcal{R}$ are isolated, meaning that no other jet is in their $\Delta R = \sqrt{(\Delta\eta)^2 + (\Delta\phi)^2} = 0.3$ vicinity.

For each $(\eta; p_{\text{T}})$ bin, the response distribution is fitted with a gaussian, and the gaussian mean is then taken as mean response $\langle\mathcal{R}\rangle$. See Figure 4.3 for examples of some fits. To remove statistical fluctuations, set of points $\{E_{\text{T}}^{\text{EM}}{}_j; \langle\mathcal{R}\rangle_j\}$,where index j runs over $E_{\text{T}}^{\text{truth}}$ bins is then fitted with a function:

$$\mathcal{F}_{\text{calib}}(E_{\text{T}}^{\text{truth}}) = \sum_{i=0}^{N_{\text{max}}} a_i \Big(\ln(E_{\text{T}}^{\text{truth}})\Big)^i, \tag{4.12}$$

where a_i are free parameters of the fit and N_{max} is chosen between 1 and 6, depending on the goodness of the fit. The fit is done separately for each η selection. The calibrated jet energy in the HI scale is then:

$$E_{\text{T,calo}}^{\text{EM+JES}} = \frac{E_{\text{T}}^{\text{EM}}}{\mathcal{F}_{\text{calib}}(E_{\text{T}}^{\text{truth}})}, \tag{4.13}$$

[1]Track jets are anti-k_t $R = 0.4$ jets reconstructed using tracks of charged particles with a chosen p_{T} selection.

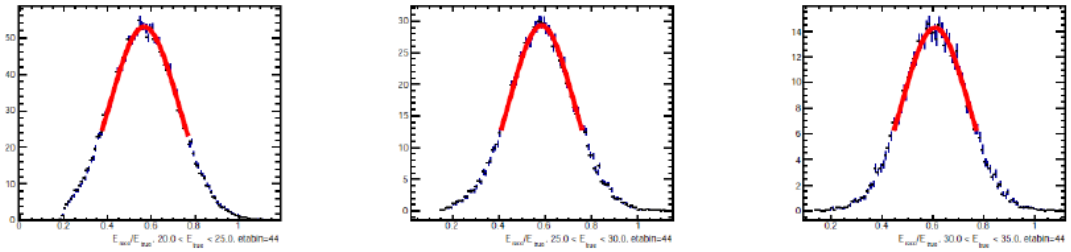

Figure 4.3: An example of gaussian fits of the response $\mathcal{R}$. Blue points represent the distribution, and the red line is a gaussian fit.

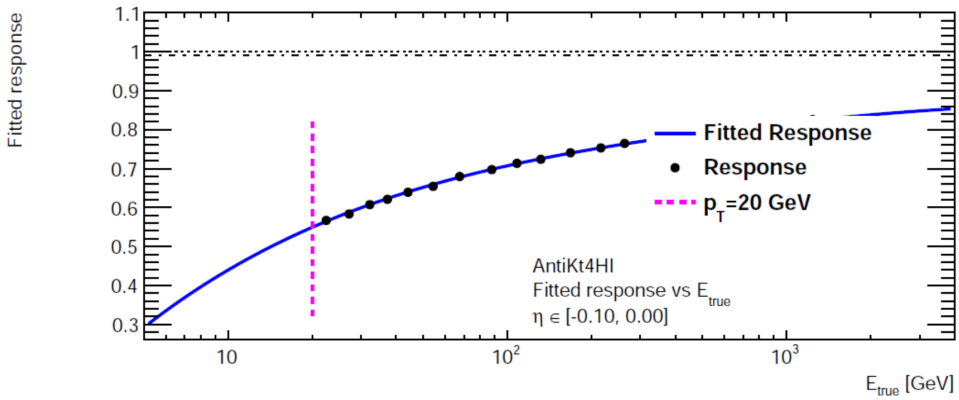

Figure 4.4: The mean response $\langle\mathcal{R}\rangle$ values (black points) and the fit $\mathcal{F}_{\text{calib}}$ (blue line) defined in Equation (4.12) for one selected $-0.1 < \eta < 0$ interval.

where the denominator value is chosen on the jets corresponding η. An example of response and the fit for one η-bin is shown in Figure 4.4.

4.3 Cross-Calibration

The performance of EM+JES jets is well understood in *pp* collisions and is described in detail in Ref. [86]. In *pp* collisions, instead of logical towers, topological clusters are used as input into anti-k_t algorithm. The jet reconstructed with this procedure, so-called EMTopo jets, differs from those reconstructed with the HI algorithm. *In situ* techniques were used to relate the energy of EMTopo jets and well-calibrated reference objects such as Z-boson and γ. The *in situ* corrections cannot be directly derived for heavy-ion runs with the same precision as is done in high statistics *pp* runs. The goal of cross-calibration (CC) is to apply these EMTopo *in situ* factors on HI jets, while the difference in the algorithms has to be taken into account. The differences arise for three reasons: different algorithm inputs, different procedures, and *in situ* calibration, which is applied to EMTopo jets but not to HI ones. The CC procedure is designed to relate the jet energy scale between the two types of reconstructions in the data and MC. It results in additional calibration factors defined as:

$$R = \frac{\left.\frac{p_{\mathrm{T}}^{\mathrm{HI}}}{p_{\mathrm{T}}^{\mathrm{EM}}}\right|_{\mathrm{DATA}}}{\left.\frac{p_{\mathrm{T}}^{\mathrm{HI}}}{p_{\mathrm{T}}^{\mathrm{EM}}}\right|_{\mathrm{MC}}}, \tag{4.14}$$

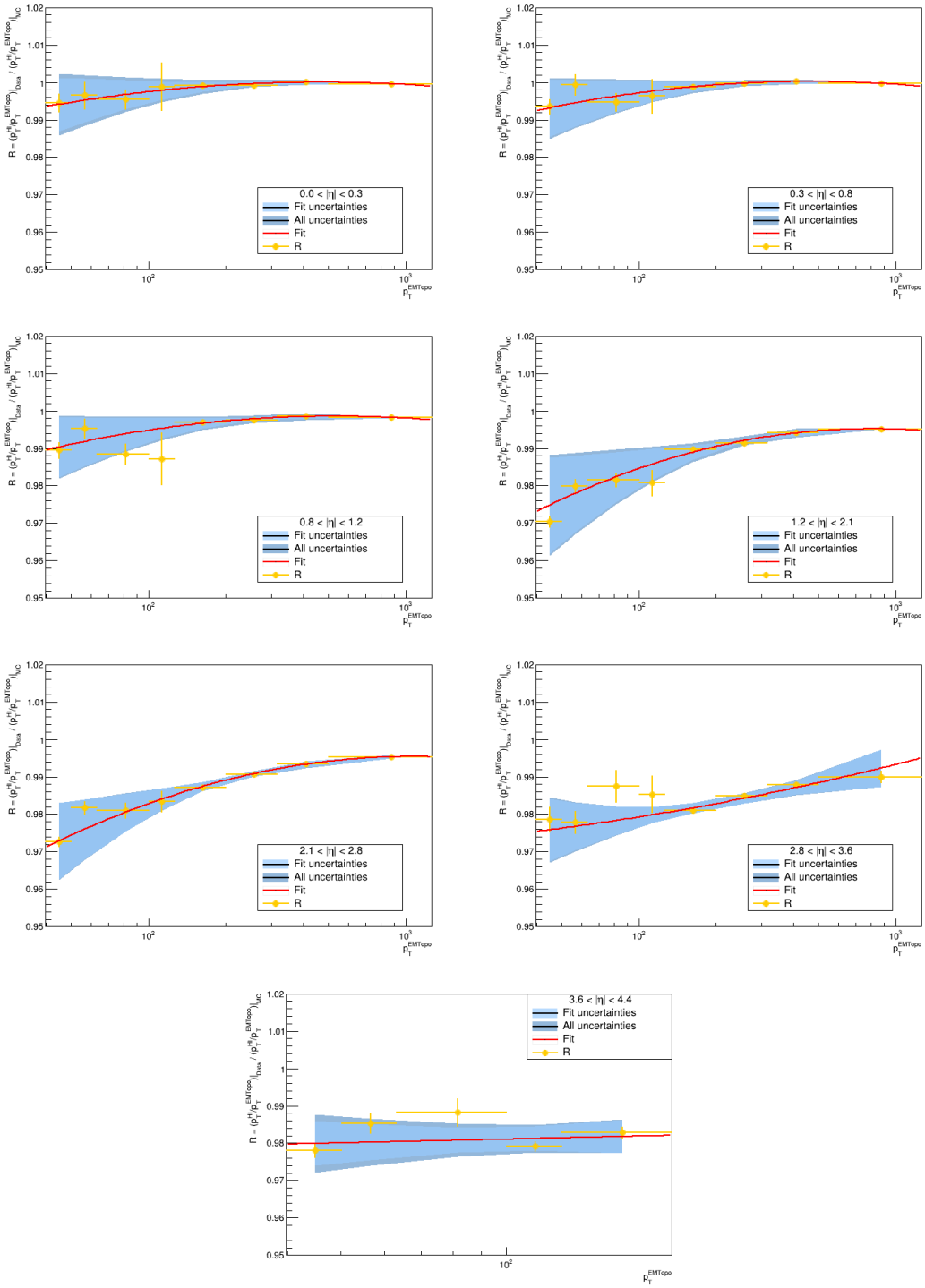

Figure 4.5: Cross-calibration factors (yellow points) as a function of $p_{\mathrm{T}}^{\mathrm{EM}}$ in 7 different η bins. Statistical uncertainties are represented by error bars, and systematic uncertainties are represented by the blue band. The red line represents the fit defined in Equation (4.15).

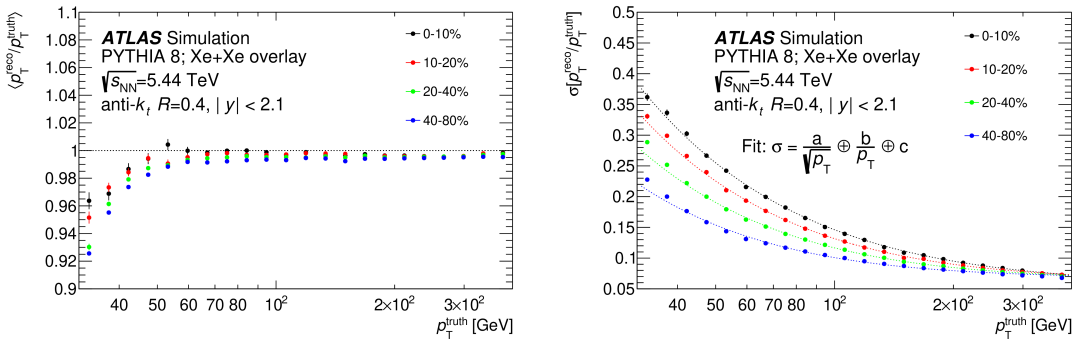

Figure 4.6: (left) Jet energy scale (JES) as a functino of $p_{\mathrm{T}}^{\mathrm{truth}}$. (right) The jet energy resolution (JER) as a function of $p_{\mathrm{T}}^{\mathrm{truth}}$. Dashed lines represent fits defined by Equation 4.18.

where $p_{\mathrm{T}}^{\mathrm{HI}}$ and $p_{\mathrm{T}}^{\mathrm{EM}}$ are the transverse momenta of jets reconstructed by HI and EMTopo algorithms, respectively. The ratio is then fitted using a fit of polynomial in logarithm:

$$\mathcal{CC}(p_{\mathrm{T}}^{\mathrm{EM}}) = c_0 + c_1 \ln(p_{\mathrm{T}}^{\mathrm{EM}}) + c_2 \ln^2(p_{\mathrm{T}}^{\mathrm{EM}}) \tag{4.15}$$

This fit is done for each of the 7 η bins in which the factors are evaluated. Figure 4.5 shows the coefficients and their fits. The energy of HI jets which result from the NI procedure is then scaled using these factors:

$$p_{\mathrm{T,calo}}^{\mathrm{HI+CC}} = \frac{p_{\mathrm{T,calo}}^{\mathrm{EM+JES}}}{\mathcal{CC}(p_{\mathrm{T}}^{\mathrm{HI}})}. \tag{4.16}$$

4.4 Jet Performance

The performance of jet reconstruction is characterized by statistical moments of jet response $p_{\mathrm{T}}^{\mathrm{reco}}/p_{\mathrm{T}}^{\mathrm{truth}}$ in MC, where $p_{\mathrm{T}}^{\mathrm{truth}}$ and $p_{\mathrm{T}}^{\mathrm{reco}}$ are transverse momenta of MC generator-level jets and jets reconstructed using the simulation of jet showering and showers' interaction with the material of the detector, respectively. The first moment is called *jet energy scale* (JES):

$$\mathrm{JES} = \left\langle \frac{p_{\mathrm{T}}^{\mathrm{reco}}}{p_{\mathrm{T}}^{\mathrm{truth}}} \right\rangle \tag{4.17}$$

and is used to evaluate the ability of reconstructed jets to have, on average, the same p_{T} as generator-level jets. The second moment is called *jet energy resolution* (JER) and describes stochastic smearing of the energy due to noise and detector imperfections. It can be parametrized as:

$$\mathrm{JER} = \sigma\left(\frac{p_{\mathrm{T}}^{\mathrm{reco}}}{p_{\mathrm{T}}^{\mathrm{truth}}}\right) = \sqrt{\left(\frac{a}{\sqrt{p_{\mathrm{T}}^{\mathrm{truth}}}}\right)^2 + \left(\frac{b}{p_{\mathrm{T}}^{\mathrm{truth}}}\right)^2 + c^2}, \tag{4.18}$$

where the terms with constants a, b, and c in Equation (4.18) are stochastic, noise, and a constant term, respectively. Parameters a and c are detector specific, and the term b represents fluctuations due to the noise and underlying event. The performance of Xe+Xe jets at $\sqrt{s_{\mathrm{NN}}} = 5.44$ TeV is shown in Figure 4.6.

While the reconstructed jets can be quite easily corrected for JES (by rescaling the jets with the JES ratio), the effects of JER are much harder to remove. The standard option to mitigate the impact of JER is to use the unfolding procedure.

5. Dijet Balance in Xe+Xe Collisions

This chapter describes a dijet balance measurement of Xe+Xe collisions measured at the ATLAS detector. The first Section 5.1 outlines the steps of the analysis, sections 5.3 and 5.4 describe individual steps in more detail. Section 5.2 describes used datasets for both Xe+Xe collisions and Monte Carlo (MC) samples. The systematic uncertainties are discussed in Section 5.5. The final Section 5.6 provides the measurement results with their discussion.

5.1 Analysis Procedure

Figure 5.1 shows a flowchart of individual steps described here. The primary observable in this analysis is a dijet yield

$$\frac{\mathrm{d}^2 N}{\mathrm{d}p_{\mathrm{T},1}\mathrm{d}p_{\mathrm{T},2}}, \tag{5.1}$$

measured differentially in $p_{\mathrm{T},1}$ and $p_{\mathrm{T},2}$, which are transverse momenta of the highest and the second-highest p_{T} jet in the event, respectively. The two jets are referred to as leading and subleading jets. In order to form a dijet, the leading and subleading jets are required to satisfy the following requirements:

- Rapidity selection for both jets: $|y| < 2.1$
- Back-to-back requirement: $\Delta\Phi = |\Delta\Phi_1 - \Delta\Phi_2| > 7/8\pi$
- p_{T} lower boundary: $p_{\mathrm{T},1} > 79$ GeV and $p_{\mathrm{T},2} > 32$ GeV

Events with dijets that do not pass these criteria are not used in the analysis. The final results use leading jets with $p_{\mathrm{T},1} > 100$ GeV and subleading jets with $p_{\mathrm{T},2} > 32$ GeV. To allow for a sufficient number of underflow bins for the unfolding procedure, leading jets start at $p_{\mathrm{T},1} > 79$ GeV.

All dijets that pass the above requirements are filled into two-dimensional $(p_{\mathrm{T},1}, p_{\mathrm{T},2})$ distributions. The distributions have a logarithmic binning with the same bin boundaries along the x— and y— axis. For N bins starting at $p_{\mathrm{T},0}$, and going up to $p_{\mathrm{T},N}$ the bin boundaries are defined as:

$$p_{\mathrm{T},i} = p_{\mathrm{T},0}\alpha^i, \qquad \alpha = \left(\frac{p_{\mathrm{T,N}}}{p_{\mathrm{T},0}}\right)^{1/N}. \tag{5.2}$$

In this analysis, $N = 32$ bins are used starting at $p_{\mathrm{T},0} = 10$ GeV up to $p_{\mathrm{T},N} = 320$ GeV. This binning produces the same bin boundaries as those used in the previous analyses [14, 15], where 40 bins from 10 GeV to 1 TeV were used. This same binning enables to compare new results from Xe+Xe collisions with the previous Pb+Pb ones.

To include the possibility that the leading and subleading jets are swapped due to the detector's resolution effects, we symmetrize the filled histogram with

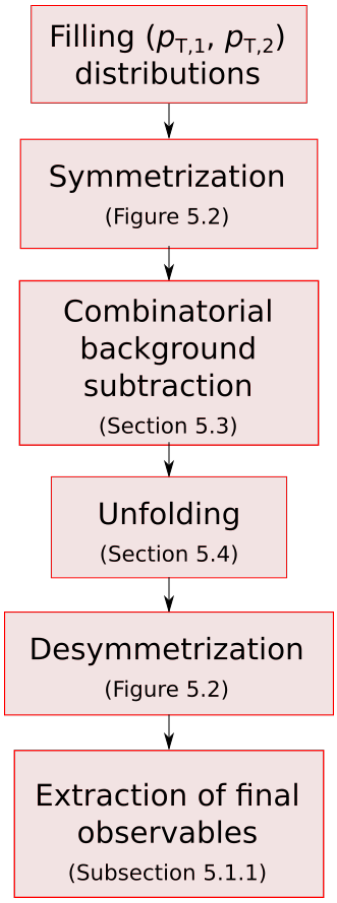

Figure 5.1: A flowchart of the analysis's steps with indicated sections and figures.

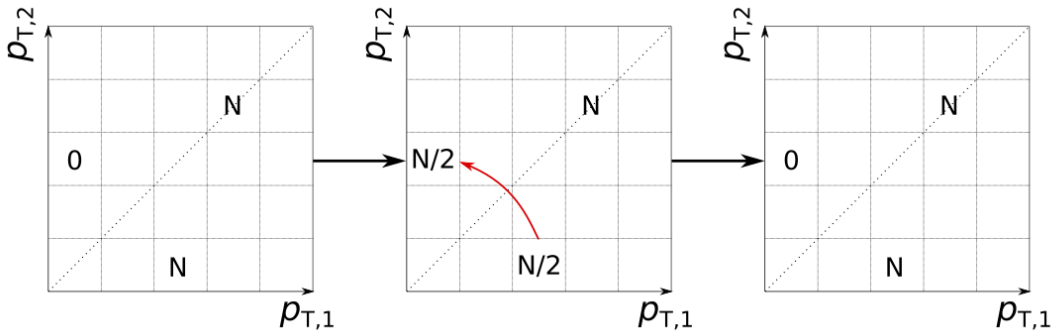

Figure 5.2: Cartoons showing the symmetrization (first to middle) and desymmetrization (middle to right) procedure applied to the $(p_{T,1}, p_{T,2})$ distributions.

respect to the $p_{T,1} = p_{T,2}$ diagonal axis — see Figure 5.2. For each bin in the $p_{T,2} < p_{T,1}$ region, we take half of the value of the bin and move it symmetrically to the bin on the other side of the diagonal. This procedure does not affect bins on the $p_{T,1} = p_{T,2}$ diagonal.

Despite well working background subtraction procedure described in Chapter 4, a residual combinatorial background needs to be subtracted from the $(p_{T,1}, p_{T,2})$ distributions. This subtraction procedure is described in Section 5.3. The subtracted $(p_{T,1}, p_{T,2})$ distributions are then corrected for detector effects using a Bayesian unfolding [88] implemented in `RooUnfold` package [89]. This unfolding procedure is described in detail in Section 5.4. After the unfolding, the $(p_{T,1}, p_{T,2})$ distribution is desymmetrized using the inverse procedure to the symmetrization shown in Figure 5.2. The desymmetrized distributions are used to calculate two final observables, which are described in the following Section 5.1.1.

5.1.1 Extraction of Observables

Although the unfolded $(p_{T,1}, p_{T,2})$ distributions are interesting by themselves, they are used to calculate two other observables, which are easier to interpret and which are reported as the main result. These observables are:

1. Dijet momentum balance — x_J
2. The ratio of pair nuclear modification factors between Xe+Xe and Pb+Pb collisions — $\rho_{Xe,Pb}$

The following text describes how these two observables are calculated.

Dijet momentum balance — x_J

Dijet momentum balance is defined as a ratio between the leading and subleading jet transverse momenta:

$$x_J = \frac{p_{T,2}}{p_{T,1}}. \tag{5.3}$$

The x_J equals to 1 represent two balanced jets and $x_J < 1$ indicates an imbalance. To account for bin-to-bin migration during the unfolding in both the leading and

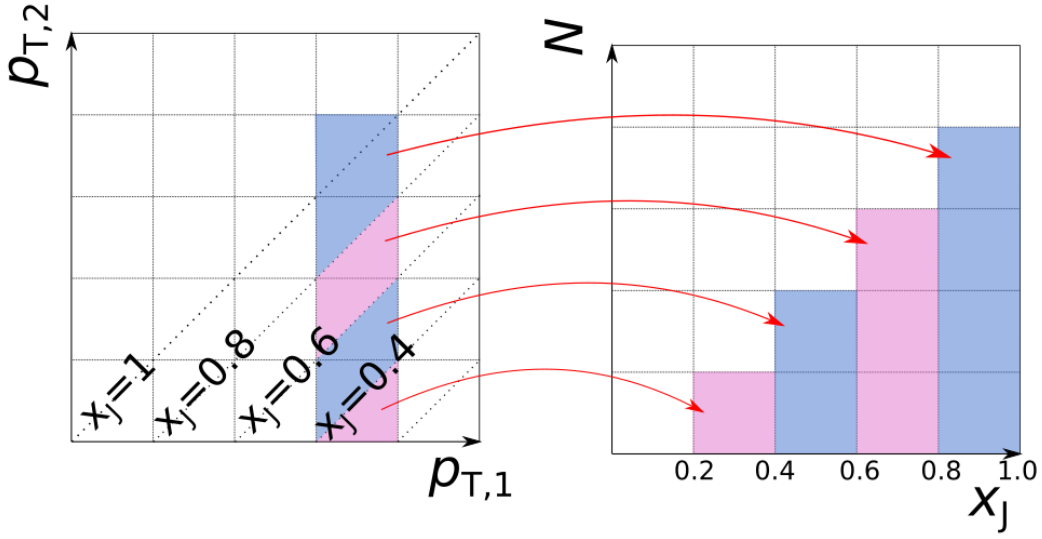

Figure 5.3: Cartoon depicting slicing of the $(p_{\mathrm{T},1}, p_{\mathrm{T},2})$ distributions and projection of the bins into x_{J} distribution.

subleading axis, we do not fill this ratio directly but make a projection from the $(p_{\mathrm{T},1}, p_{\mathrm{T},2})$ distribution as depicted in Figure 5.3. The x_{J} distribution is created by diagonally slicing the unfolded and desymmetrized distribution. The x_{J} bin boundaries are defined as $x_{\mathrm{J},i} = \alpha^{i-N}$, where α was previously defined in Equation 5.2. For this bin selection, individual x_{J} values are diagonals cutting the $(p_{\mathrm{T},1}, p_{\mathrm{T},2})$ distribution bins into halves. For each bin in the $(p_{\mathrm{T},1}, p_{\mathrm{T},2})$ distribution, half of the yield contributes to the upper x_{J} bin and half to the lower x_{J} bin. Diagonal bins, which correspond to $x_{\mathrm{J}} = 1$, are not halved, and their full yield is moved to the highest x_{J} bin. The lowest x_{J} bin contains only one half of one bin from the $(p_{\mathrm{T},1}, p_{\mathrm{T},2})$ distribution. These bottom bins are never used in the analysis due to the appropriate choice of lower boundaries. The lowest reported x_{J} bin is $x_{\mathrm{J}} = 0.32$. The upper boundary $x_{\mathrm{J}} = 1$ stems from the definition of the dijet, as the subleading jet, must always have lower p_{T} than the leading one. Two normalizations of the x_{J} distributions are used, leading to: *per-pair normalized* and *absolutely normalized* x_{J} distributions, and they are described in detail in the Introduction.

A comparison of x_{J} distributions measured in Xe+Xe and Pb+Pb exhibited a difference, as we will show in detail in Section 5.6. This difference may be partially attributed to the difference in hard process cross-section due to the different center-of-mass energy between Xe+Xe and Pb+Pb collisions. To quantify this difference and correct for it, we evaluate the ratio of `PYTHIA8` x_{J} distributions in 5.44 TeV pp collisions to the same quantity in 5.02 TeV pp collisions. The ratio is defined as:

$$\mathcal{C}(x_{\mathrm{J}}) = \frac{1/N \ \mathrm{d}N^{\mathrm{pair}}_{\texttt{PYTHIA8}}(pp, 5.44 \text{ TeV})/\mathrm{d}x_{\mathrm{J}}}{1/N \ \mathrm{d}N^{\mathrm{pair}}_{\texttt{PYTHIA8}}(pp, 5.02 \text{ TeV})/\mathrm{d}x_{\mathrm{J}}}, \tag{5.4}$$

where the normalization factor N is $N_{\mathrm{evt}}\langle T_{\mathrm{AA}}\rangle$ and N_{pair} for absolutely normalized and per-pair normalized distributions, respectively. These coefficients are used to scale Pb+Pb x_{J} distributions bin-by-bin. The factors for absolutely normalized x_{J} distributions are shown in Figure 5.5 (left). Per-pair normalized x_{J}

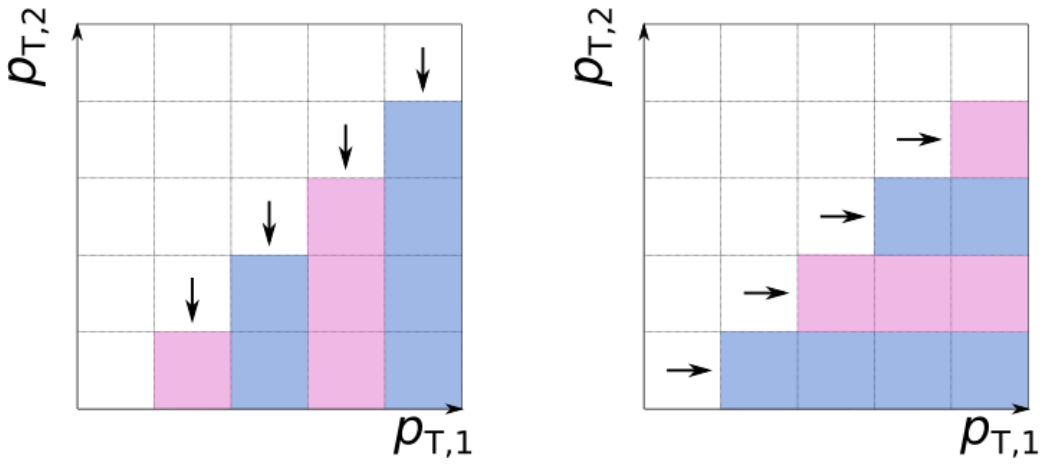

Figure 5.4: Cartoon showing projections of leading (left) and subleading (right) jet yields from 2D $(p_{T,1}, p_{T,2})$ distributions. Content in bins with the same color is added together and projected to the respective axis in the direction of the black arrow.

distributions are not scaled by this factor because the $\mathcal{C}$-factor is consistent with the unity.

The Ratio of pair nuclear modification factors between Pb+Pb and Xe+Xe — $\rho_{\mathbf{Xe,Pb}}$

A comparison between Pb+Pb and Xe+Xe dijet yields is a valuable physical result. Since we already have the unfolded $(p_{T,1}, p_{T,2})$ distributions, we can project them to $p_{T,1}$- and $p_{T,2}$-axis, to produce leading and subleading jet yields, respectively (see Figure 5.4). These can be used in the evaluation of pair nuclear modification factor R_{AA}^{pair} for leading and subleading jets for Xe+Xe collisions at $\sqrt{s_{NN}} = 5.44$ TeV:

$$R_{Xe+Xe}^{pair}(p_{T,1}) = \frac{\frac{1}{\left\langle T_{AA}^{Xe+Xe}\right\rangle N_{evt}^{Xe+Xe}} \int_{0.32\times p_{T,1}}^{p_{T,1}} \frac{d^2N^{pair}(Xe+Xe, 5.44\text{ TeV})}{dp_{T,1}dp_{T,2}} dp_{T,2}}{\frac{1}{L_{pp}} \int_{0.32\times p_{T,1}}^{p_{T,1}} \frac{d^2N^{pair}(pp, 5.44\text{ TeV})}{dp_{T,1}dp_{T,2}} dp_{T,2}} \quad (5.5)$$

and for subleading jets:

$$R_{Xe+Xe}^{pair}(p_{T,2}) = \frac{\frac{1}{\left\langle T_{AA}^{Xe+Xe}\right\rangle N_{evt}^{Xe+Xe}} \int_{p_{T,2}}^{p_{T,2}/0.32} \frac{d^2N^{pair}(Xe+Xe, 5.44\text{ TeV})}{dp_{T,1}dp_{T,2}} dp_{T,1}}{\frac{1}{L_{pp}} \int_{p_{T,2}}^{p_{T,2}/0.32} \frac{d^2N^{pair}(pp, 5.44\text{ TeV})}{dp_{T,1}dp_{T,2}} dp_{T,1}}. \quad (5.6)$$

The logic behind the pair nuclear modification factor R_{AA}^{pair} is the same as for the standard R_{AA} introduced in Section 2.9, but the yields for both heavy-ion and pp are taken from jets forming a dijet. Therefore, it should not be interchanged with an inclusive R_{AA}.

Since pp data are not available for 5.44 TeV, pp reference data at 5.02 TeV, that were used in Pb+Pb analysis, are used instead. The pp yields are corrected for a hard process cross-section by introducing correction factors $\mathcal{C}(p_{\mathrm{T},1})$ and $\mathcal{C}(p_{\mathrm{T},2})$ for leading and subleading jets, respectively. These factors are defined using `PYTHIA8` MC:

$$\mathcal{C}(p_{\mathrm{T},1}) = \frac{\int_{0.32\times p_{\mathrm{T},1}}^{p_{\mathrm{T},1}} \frac{\mathrm{d}^2 N^{\mathrm{pair}}_{\texttt{PYTHIA8}}(pp,\,5.44\text{ TeV})}{\mathrm{d}p_{\mathrm{T},1}\mathrm{d}p_{\mathrm{T},2}}\mathrm{d}p_{\mathrm{T},2}}{\int_{0.32\times p_{\mathrm{T},1}}^{p_{\mathrm{T},1}} \frac{\mathrm{d}^2 N^{\mathrm{pair}}_{\texttt{PYTHIA8}}(pp,\,5.02\text{ TeV})}{\mathrm{d}p_{\mathrm{T},1}\mathrm{d}p_{\mathrm{T},2}}\mathrm{d}p_{\mathrm{T},2}} \tag{5.7}$$

and

$$\mathcal{C}(p_{\mathrm{T},2}) = \frac{\int_{p_{\mathrm{T},2}}^{p_{\mathrm{T},2}/0.32} \frac{\mathrm{d}^2 N^{\mathrm{pair}}_{\texttt{PYTHIA8}}(pp,\,5.44\text{ TeV})}{\mathrm{d}p_{\mathrm{T},1}\mathrm{d}p_{\mathrm{T},2}}\mathrm{d}p_{\mathrm{T},2}}{\int_{p_{\mathrm{T},2}}^{p_{\mathrm{T},2}/0.32} \frac{\mathrm{d}^2 N^{\mathrm{pair}}_{\texttt{PYTHIA8}}(pp,\,5.02\text{ TeV})}{\mathrm{d}p_{\mathrm{T},1}\mathrm{d}p_{\mathrm{T},2}}\mathrm{d}p_{\mathrm{T},2}}. \tag{5.8}$$

Figure 5.5 (middle and right) shows $\mathcal{C}(p_{\mathrm{T},1})$ and $\mathcal{C}(p_{\mathrm{T},2})$ factors along with fits. The values of $\mathcal{C}$-factors increase monotonically with p_{T}, starting at 12% for $p_{\mathrm{T}} = 32$ GeV and increasing to 31% for $p_{\mathrm{T}} = 398$ GeV. To remove statistical fluctuations, the $\mathcal{C}$-factor distributions were fitted with a linear function, and the values from the fits were used in the analysis. Equation (5.5) can be rewritten using the definition (5.7) as:

$$R^{\mathrm{pair}}_{\mathrm{Xe+Xe}}(p_{\mathrm{T},1}) = \frac{\frac{1}{\left\langle T^{\mathrm{Xe+Xe}}_{\mathrm{AA}}\right\rangle N^{\mathrm{Xe+Xe}}_{\mathrm{evt}}} \int_{0.32\times p_{\mathrm{T},1}}^{p_{\mathrm{T},1}} \frac{\mathrm{d}^2 N^{\mathrm{pair}}(\mathrm{Xe+Xe},\,5.44\text{ TeV})}{\mathrm{d}p_{\mathrm{T},1}\mathrm{d}p_{\mathrm{T},2}}\mathrm{d}p_{\mathrm{T},2}}{C^{\mathrm{lead}} \times \frac{1}{L_{pp}} \int_{0.32\times p_{\mathrm{T},1}}^{p_{\mathrm{T},1}} \frac{\mathrm{d}^2 N^{\mathrm{pair}}(pp,\,5.02\text{ TeV})}{\mathrm{d}p_{\mathrm{T},1}\mathrm{d}p_{\mathrm{T},2}}\mathrm{d}p_{\mathrm{T},2}}, \tag{5.9}$$

For Pb+Pb collisions at 5.02 TeV we define pair $R^{\mathrm{pair}}_{\mathrm{AA}}$ for leading jets as:

$$R^{\mathrm{pair}}_{\mathrm{Pb+Pb}}(p_{\mathrm{T},1}) = \frac{\frac{1}{\left\langle T^{\mathrm{Xe+Xe}}_{\mathrm{AA}}\right\rangle N^{\mathrm{Pb+Pb}}_{\mathrm{evt}}} \int_{0.32\times p_{\mathrm{T},1}}^{p_{\mathrm{T},1}} \frac{\mathrm{d}^2 N^{\mathrm{pair}}(\mathrm{Pb+Pb},\,5.02\text{ TeV})}{\mathrm{d}p_{\mathrm{T},1}\mathrm{d}p_{\mathrm{T},2}}\mathrm{d}p_{\mathrm{T},2}}{\frac{1}{L_{pp}} \int_{0.32\times p_{\mathrm{T},1}}^{p_{\mathrm{T},1}} \frac{\mathrm{d}^2 N^{\mathrm{pair}}(pp,\,5.02\text{ TeV})}{\mathrm{d}p_{\mathrm{T},1}\mathrm{d}p_{\mathrm{T},2}}\mathrm{d}p_{\mathrm{T},2}} \tag{5.10}$$

and analogically with (5.6) for subleading jets. To compare Xe+Xe and Pb+Pb collisions, we can define a ratio $\rho_{\mathrm{Xe,Pb}}$ between (5.9) and (5.10):

$$\rho_{\mathrm{Xe,Pb}}(p_{\mathrm{T},1}) = \frac{R^{\mathrm{pair}}_{\mathrm{AA}}(p_{\mathrm{T},1})|_{\mathrm{Xe+Xe}}}{R^{\mathrm{pair}}_{\mathrm{AA}}(p_{\mathrm{T},1})|_{\mathrm{Pb+Pb}}} = \frac{\frac{1}{\left\langle T^{\mathrm{Xe+Xe}}_{\mathrm{AA}}\right\rangle N^{\mathrm{Xe+Xe}}_{\mathrm{evt}}} \int_{0.32\times p_{\mathrm{T},1}}^{p_{\mathrm{T},1}} \frac{\mathrm{d}^2 N^{\mathrm{pair}}(\mathrm{Xe+Xe},\,5.44\text{ TeV})}{\mathrm{d}p_{\mathrm{T},1}\mathrm{d}p_{\mathrm{T},2}}\mathrm{d}p_{\mathrm{T},2}}{\mathcal{C}(p_{\mathrm{T},1}) \times \frac{1}{\left\langle T^{\mathrm{Xe+Xe}}_{\mathrm{AA}}\right\rangle N^{\mathrm{Pb+Pb}}_{\mathrm{evt}}} \int_{0.32\times p_{\mathrm{T},1}}^{p_{\mathrm{T},1}} \frac{\mathrm{d}^2 N^{\mathrm{pair}}(\mathrm{Pb+Pb},\,5.02\text{ TeV})}{\mathrm{d}p_{\mathrm{T},1}\mathrm{d}p_{\mathrm{T},2}}\mathrm{d}p_{\mathrm{T},2}} \tag{5.11}$$

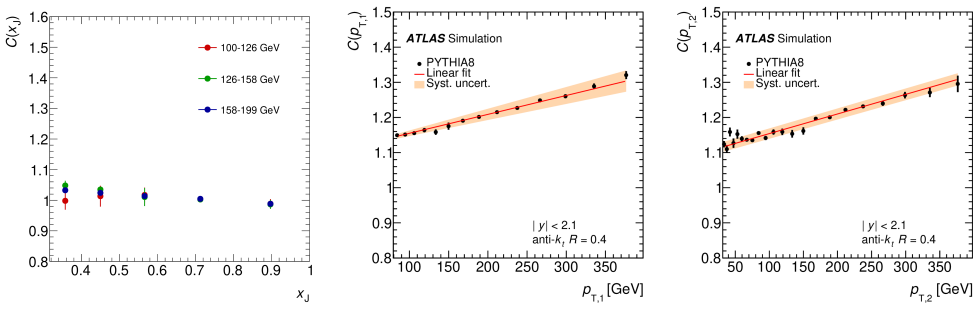

Figure 5.5: Left: $\mathcal{C}(x_{\mathrm{J}})$ as defined in Eq. (5.4) for three different $p_{\mathrm{T},1}$ intervals. The error bars represent the systematic uncertainty. Middle and right: The values and linear fits of $\mathcal{C}(p_{\mathrm{T},1})$ and $\mathcal{C}(p_{\mathrm{T},2})$, respectively. The orange bands represent the systematic uncertainty. The systematic uncertainties are explained in detail in Section 5.5.

and for subleading jets:

$$\rho_{\mathrm{Xe,Pb}}(p_{\mathrm{T},2}) = \frac{R_{\mathrm{AA}}^{\mathrm{pair}}(p_{\mathrm{T},2})|_{\mathrm{Xe+Xe}}}{R_{\mathrm{AA}}^{\mathrm{pair}}(p_{\mathrm{T},2})|_{\mathrm{Pb+Pb}}} = \frac{\frac{1}{\left\langle T_{\mathrm{AA}}^{\mathrm{Xe+Xe}}\right\rangle N_{\mathrm{evt}}^{\mathrm{Xe+Xe}}}\int_{p_{\mathrm{T},2}}^{p_{\mathrm{T},2}/0.32}\frac{\mathrm{d}^2N^{\mathrm{pair}}(\mathrm{Xe+Xe},5.44\ \mathrm{TeV})}{\mathrm{d}p_{\mathrm{T},1}\mathrm{d}p_{\mathrm{T},2}}\mathrm{d}p_{\mathrm{T},1}}{\mathcal{C}(p_{\mathrm{T},2})\times\frac{1}{\left\langle T_{\mathrm{AA}}^{\mathrm{Xe+Xe}}\right\rangle N_{\mathrm{evt}}^{\mathrm{Pb+Pb}}}\int_{p_{\mathrm{T},2}}^{p_{\mathrm{T},2}/0.32}\frac{\mathrm{d}^2N^{\mathrm{pair}}(\mathrm{Pb+Pb},5.02\ \mathrm{TeV})}{\mathrm{d}p_{\mathrm{T},1}\mathrm{d}p_{\mathrm{T},2}}\mathrm{d}p_{\mathrm{T},1}}. \quad (5.12)$$

The $\rho_{\mathrm{Xe,Pb}}$ can be viewed as a ratio of $R_{\mathrm{AA}}^{\mathrm{pair}}$ and the C-factors than as a correction for the difference between pp cross-section at 5.44 TeV and pp cross-section at 5.02 TeV. At the same time, one can interpret $\rho_{\mathrm{Xe,Pb}}$ as a simple ratio of yields where the yields measured in Pb+Pb are corrected for the difference in the center-of-mass energy of the cross-section describing the hard process. This correction, of course, does not correct all the differences between Xe+Xe and Pb+Pb, namely the impact of nPDFs, the impact of the difference in the geometry, etc.

5.2 Monte Carlo and Data Events

This section describes centrality definition, event selection and cleaning applied on measured Xe+Xe data and MC events samples.

5.2.1 Centrality Definition

Centrality is an important concept in heavy-ion collisions. The centrality of the collision is a degree of the overlap of two colliding nuclei that can be quantified by the impact parameter, that is, the distance between the centers of the two nuclei. If they collide head-on, the collision is central; if they just graze each other, we speak about peripheral collisions. We cannot measure the impact parameter to determine the centrality, but we can measure the overall event activity in the collision, characterized, e.g., by the sum of E_{T} measured in forward (FCal)

calorimeters, $\Sigma E_{\mathrm{T}}^{\mathrm{FCal}}$ on both sides of the detector. Central collisions have large $\Sigma E_{\mathrm{T}}^{\mathrm{FCal}}$ deposits, and peripheral have small $\Sigma E_{\mathrm{T}}^{\mathrm{FCal}}$ deposits. A more detailed explanation of the centrality and its calculation is provided in Section 2.2.

The centrality estimation in this analysis follows the procedure used in Pb+Pb collisions. The $\Sigma E_{\mathrm{T}}^{\mathrm{FCal}}$ distribution is divided into percentiles of the total inelastic cross-section for Pb+Pb collisions. The first percentile, $0-10\%$, represents the 10% of collisions with the largest event activity and the smallest impact parameter. The last percentile, $90-100\%$, represents the 10% of collisions where there is the smallest event activity and the largest impact parameter. The $\Sigma E_{\mathrm{T}}^{\mathrm{FCal}}$ distribution with the corresponding quantiles is shown in Figure 5.6, overlaid with the 2015 Pb+Pb distribution since the two collision systems are compared in this analysis.

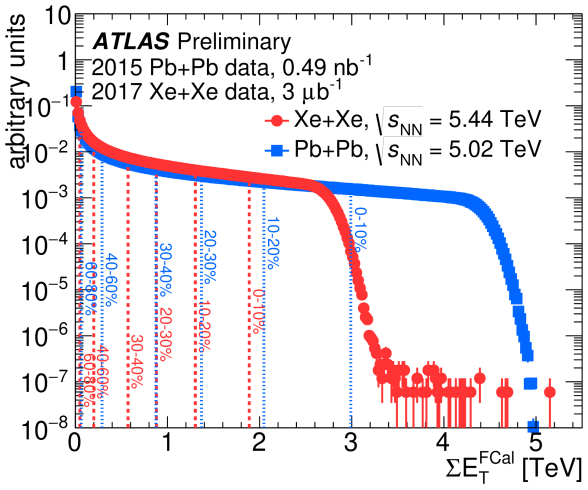

Figure 5.6: The $\Sigma E_{\mathrm{T}}^{\mathrm{FCal}}$ distributions in Xe+Xe collisions at $\sqrt{s_{\mathrm{NN}}} = 5.44$ TeV in circles and Pb+Pb collisions at $\sqrt{s_{\mathrm{NN}}} = 5.02$ TeV in square points. Dashed lines on the figure indicate the respective centrality intervals for each collision system: $0-10\%$, $10-20\%$, $20-30\%$, $30-40\%$, $40-60\%$, and $60-80\%$.

The results of Xe+Xe collisions are reported in the following four centrality intervals: $0-10\%$, $10-20\%$, $20-40\%$, $40-80\%$. The corresponding $\Sigma E_{\mathrm{T}}^{\mathrm{FCal}}$ values are shown in Table 5.1. These results are compared with Pb+Pb results evaluated in the same centrality bins.

The Xe+Xe results are compared to Pb+Pb results in Pb+Pb centralities as well. That is, we take Pb+Pb centrality intervals and apply their $\Sigma E_{\mathrm{T}}^{\mathrm{FCal}}$ boundaries to Xe+Xe collisions. This compares the two systems in events with the same event activity. Centrality and $\Sigma E_{\mathrm{T}}^{\mathrm{FCal}}$ interval boundaries for this compaison are summarized in Table 5.2.

5.2.2 Event Selection of Xe+Xe Data

The Xe+Xe data used in this analysis was taken during a short run in the 2017 data-taking period at $\sqrt{s_{\mathrm{NN}}} = 5.44$ TeV with a total luminosity of $3\,\mu\mathrm{b}^{-1}$. The Xe+Xe events are selected with two minimum-bias triggers that are described in Section 3.2.6. These triggers are fully efficient for all jets used in this analysis.

Xe+Xe Cent. [%]	$\Sigma E_{\mathrm{T}}^{\mathrm{FCal}}$ [TeV]	$N_{\mathrm{coll}}^{\mathrm{Xe+Xe}}$	$\left\langle T_{\mathrm{AA}}^{\mathrm{Xe+Xe}} \right\rangle$ [mb^{-1}]
$0-10$	>1.887	879.15 ± 35.03	12.38 ± 0.08
$10-20$	1.887–1.303	535.17 ± 20.91	7.54 ± 0.09
$20-40$	1.303–0.572	249.66 ± 10.35	3.52 ± 0.09
$40-80$	0.572–0.049	44.71 ± 2.69	0.63 ± 0.04

Table 5.1: Centrality ranges for Xe+Xe collisions used in the analysis with their corresponding $\Sigma E_{\mathrm{T}}^{\mathrm{FCal}}$, $N_{\mathrm{coll}}^{\mathrm{Xe+Xe}}$, and $\left\langle T_{\mathrm{AA}}^{\mathrm{Xe+Xe}} \right\rangle$ values. Values are taken from [90].

Pb+Pb Cent. [%]	$\Sigma E_{\mathrm{T}}^{\mathrm{FCal}}$ [TeV]	$N_{\mathrm{coll}}^{\mathrm{Pb+Pb}}$	$\left\langle T_{\mathrm{AA}}^{\mathrm{Xe+Xe}} \right\rangle$ [mb^{-1}]
$10-20$	2.056–3.00	926.47 ± 37.05	13.05 ± 0.08
$20-40$	0.885–2.056	457.97 ± 17.85	6.45 ± 0.09
$40-60$	0.296–0.885	128.86 ± 6.14	1.81 ± 0.07
$60-80$	0.066–0.296	25.81 ± 1.85	0.36 ± 0.03

Table 5.2: Centrality ranges for Pb+Pb used to compare with Xe+Xe in the analysis with their corresponding $\Sigma E_{\mathrm{T}}^{\mathrm{FCal}}$, $N_{\mathrm{coll}}^{\mathrm{Pb+Pb}}$, and T_{AA} values for Xe+Xe collisions. Values are taken from [90, 91].

The events were also required to pass the standard ATLAS event-level selection criteria:

- All the sub-detector systems were required to be fully functional: all the data were required to pass the official good run list:
  `data17_hi.periodAllYear_DetStatus-v97-pro21-14_PHYS_StandardGRL_All_Good.xml`.
- All events are required to have a good reconstructed primary vertex.
- Additional event cleaning to remove additional detector imperfections (problematic events due to LAr, Tile, SCT, incomplete events) using ATLAS standard methods.
- The pile-up constribution is removed ($\approx 0.1\%$ events). These are events with multiple inelastic scatterings during one bunch crossing.

The cut to remove a small number of pileup events is made through a simple cut based on a tight correlation between the $\Sigma E_{\mathrm{T}}^{\mathrm{FCal}}$ and the number of reconstructed tracks. This correlation is shown in Figure 5.7 along with a line representing the cut where anything below the line is rejected. Formally, this cut is the following:

$$\mathrm{FCal}\ E_{\mathrm{T}} < 0.21047 + 0.0015335 \cdot N_{\mathrm{trk}},$$

where N_{trk} is number of tracks with $p_{\mathrm{T}} > 0.5$ GeV that pass standard track selections. This cut was derived previously for the centrality estimate. The right panel of Figure 5.7 shows the fraction of events without pileup after the rejection has been applied and indicates that the fraction of removed events is very small for the majority of $\Sigma E_{\mathrm{T}}^{\mathrm{FCal}}$ values. Where it is the largest, i.e. for events with $\Sigma E_{\mathrm{T}}^{\mathrm{FCal}} \sim 2.9\,\mathrm{TeV}$, around 1% contamination is present, while events with lower $\Sigma E_{\mathrm{T}}^{\mathrm{FCal}}$ exhibit even smaller contamination.

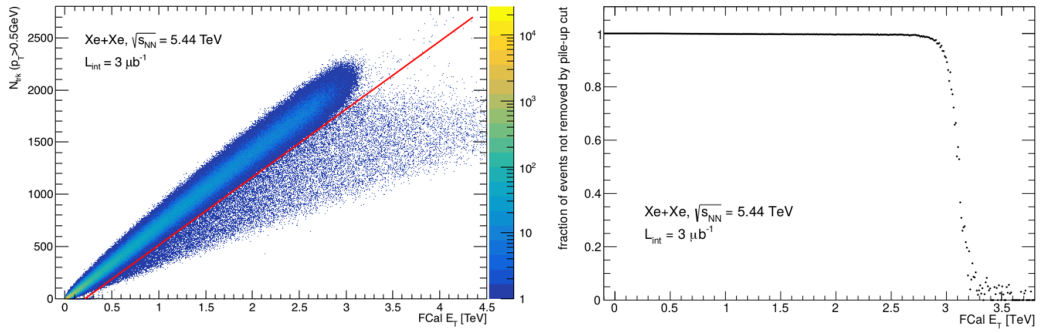

Figure 5.7: Left: Correlation between $\Sigma E_{\mathrm{T}}^{\mathrm{FCal}}$ and track multiplicity. The line represents a cut to remove pileup events. Right: The fraction of events without pileup. All for Xe+Xe collisions at $\sqrt{s_{\mathrm{NN}}} = 5.44$ TeV.

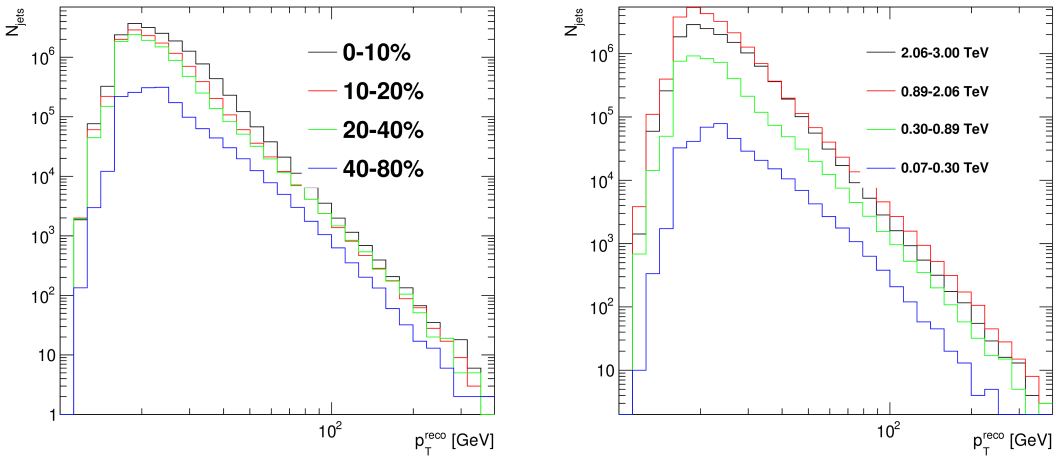

Figure 5.8: The p_{T} spectrum of inclusive reconstructed jets in Xe+Xe collisions at $\sqrt{s_{\mathrm{NN}}} = 5.44$ TeV for four centrality intervals (left) and four $\Sigma E_{\mathrm{T}}^{\mathrm{FCal}}$ intervals (right).

There were 15.3 million events recorded after applying the event selection criteria. The trigger sampled 82.4% of the total inelastic cross-section in Xe+Xe with an uncertainty of 1% [92, 93].

Figure 5.8 shows inclusive jet p_{T} spectrum in four centrality, and four $\Sigma E_{\mathrm{T}}^{\mathrm{FCal}}$ intervals for Xe+Xe collisions data.

5.2.3 Monte Carlo Samples

Pythia

The analysis of 2017 Xe+Xe data uses the `PYTHIA8` [94] pp jet events at $\sqrt{s} = 5.44$ TeV with the A14 tune [95] and the NNPDF23LO parton distribution functions [96]. This signal is then overlaid with the real minimum bias 5.44 TeV Xe+Xe data. The definitions of the overlay MC samples can be found in Tab. 5.3.

There is a difference between data and MC $\Sigma E_{\mathrm{T}}^{\mathrm{FCal}}$ spectra due to a difference in the trigger between the full dataset and the data used for the overlay.

JZ	$R = 0.4$ $p_{\mathrm{T}}^{\mathrm{truth}}$ [GeV]	σ [nb] $\times\epsilon$	# events
1	20–60	$(6.87\times 10^{7}) \times (3.35\times 10^{-3})$	$3 * 10^{6}$
2	60–160	$(7.21\times 10^{5}) \times (4.51\times 10^{-3})$	$4 * 10^{6}$
3	160–400	$(5.52\times 10^{3}) \times (5.64\times 10^{-3})$	$4 * 10^{6}$

Table 5.3: `PYTHIA8` MC generator samples used in the Xe+Xe dijet balance analysis. The table shows MC generator-level jets p_{T} ranges ($p_{\mathrm{T}}^{\mathrm{truth}}$), cross-sections ($\sigma$), filtering efficiencies (ϵ), and number of events per JZ slice.

To take into account this diffference, MC `PYTHIA8` samples were reweighted by a DATA/MC $\Sigma E_{\mathrm{T}}^{\mathrm{FCal}}$ ratio. Figure 5.9 shows this ratio as well as individual MC and Xe+Xe data $\Sigma E_{\mathrm{T}}^{\mathrm{FCal}}$ distributions. For $\Sigma E_{\mathrm{T}}^{\mathrm{FCal}} \gtrsim 3$ TeV, the ratio is subject to very high fluctuations coming from low statistics. These fluctuations were removed by replacing the higher values with a constant value. The constant was chosen as a value of the last bin used from the distribution before the fluctuations were present. More than 99.9% of both data and MC events are below $\Sigma E_{\mathrm{T}}^{\mathrm{FCal}} < 3$ TeV — therefore, this simple removal of the fluctuations is a sufficient replacement.

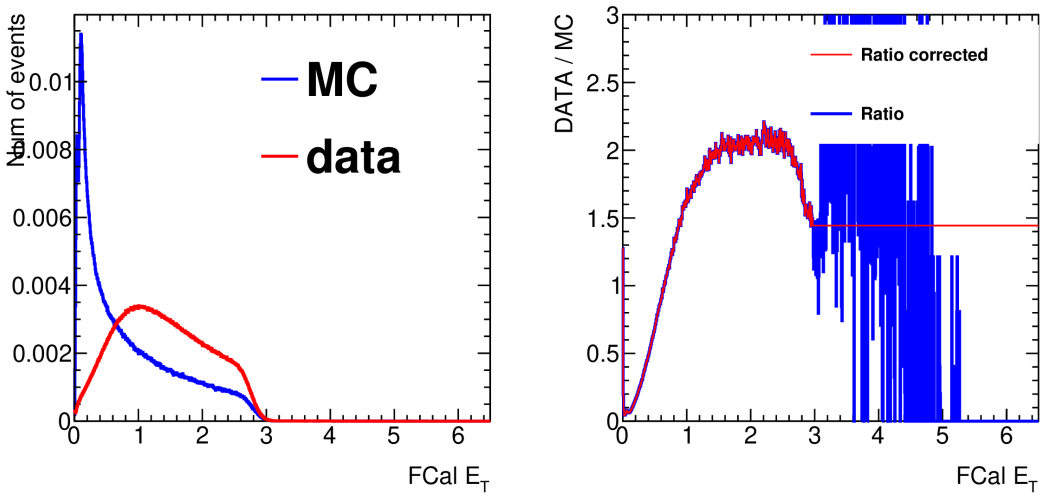

Figure 5.9: Left: `PYTHIA8` MC (blue) and Xe+Xe data (red) $\Sigma E_{\mathrm{T}}^{\mathrm{FCal}}$ distribution at $\sqrt{s_{\mathrm{NN}}} = 5.44$ TeV. Right: The ratio of Xe+Xe data to `PYTHIA8` MC — the blue line represents the ratio, and the red line is the ratio corrected for statistical fluctuations.

Herwig

A different MC generator — `HERWIG7` was used to generate events with the same setting as `PYTHIA8`. `HERWIG7` samples also consisted of three JZ samples, each containing 10^6 events. This `HERWIG7` sample is used to generate systematic uncertainties as discussed in Section 5.5.

5.3 Combinatorial Background

The $(p_{\mathrm{T},1}, p_{\mathrm{T},2})$ distributions need to be corrected for the presence of the combinatorial background coming from jet pairs not originating in the same hard process and from spurious jets from fluctuations of the UE. The background subtraction procedure consisting of two steps was developed. The first step is to subtract the combinatorial background yields in each $(p_{\mathrm{T},1}, p_{\mathrm{T},2})$ bin. The method for the estimation of the size of the background is described in detail in Section 5.3.1. This subtraction, however, has an inefficiency, which results in an over-subtraction. This effect was corrected by efficiency correction in the second step, which is described in the next Section 5.3.2. The values of corrected yields, N^{corr}, in each $(p_{\mathrm{T},1}, p_{\mathrm{T},2})$ bin, are given by the following equation:

$$N^{\mathrm{corr}} = \frac{1}{\epsilon}(N^{\mathrm{raw}} - B), \tag{5.13}$$

where B and ϵ are the size of the combinatorial background dijet yield and the size of the efficiency correction, respectively. N^{raw} is a raw dijet yield in a given bin before any correction.

5.3.1 Background Subtraction

The combinatorial background yield B from Equation (5.13) is estimated as a yield of subleading jets in $1.0 < \Delta\Phi < 1.4$ window, where $\Delta\Phi$ is the absolute difference in Φ of the two jets. This boundary was selected to minimize the contribution from correlated dijet pairs, which have a maximum at $\Delta\Phi = \pi$, and to minimize the contribution from split jets in the vicinity of $\Delta\Phi = 0$.

The performance of the subtraction procedure was checked in a well-controlled environment of MC, where dijet yields could be divided into two disjoint groups:

1. *Signal dijets* — dijets where both leading and subleading jets are required to be matched to a truth jet.

2. *Combinatorial dijets* — dijets where the leading jet is required to be matched to a truth jet, and the subleading jet is required to have no truth jet in its $\Delta R = 0.35$ radius.

To verify that no bias from residual hydrodynamical flow is present, a $\Delta\Phi$ distribution of combinatorial dijets was investigated. Such a distribution is expected to be flat in the absence of the residual flow. Distributions for a few selected bins are shown in Figure 5.10 along with a constant function fit. Because the distributions show no $\Delta\Phi$ dependence, no elliptic flow modulation is observed, and no Φ-dependent correction on the background is needed. The background is, therefore, only a scale factor, subtracted from the measured $(p_{\mathrm{T},1}, p_{\mathrm{T},2})$ distributions on a bin-by-bin basis. The size of the background in the background window is scaled by a factor of $(\pi/8)/0.4$ to account for the difference in the area of the fiducial region of the measurement and the area of the region where the background is determined.

Figure 5.11 shows $\Delta\Phi$ distributions of signal and combinatorial dijets for a few selected bins in MC generator `PYTHIA8`. This figure demonstrates that in our background window $1.0 < |\Delta\Phi| < 1.4$, dijets consist primarily of combinatorial

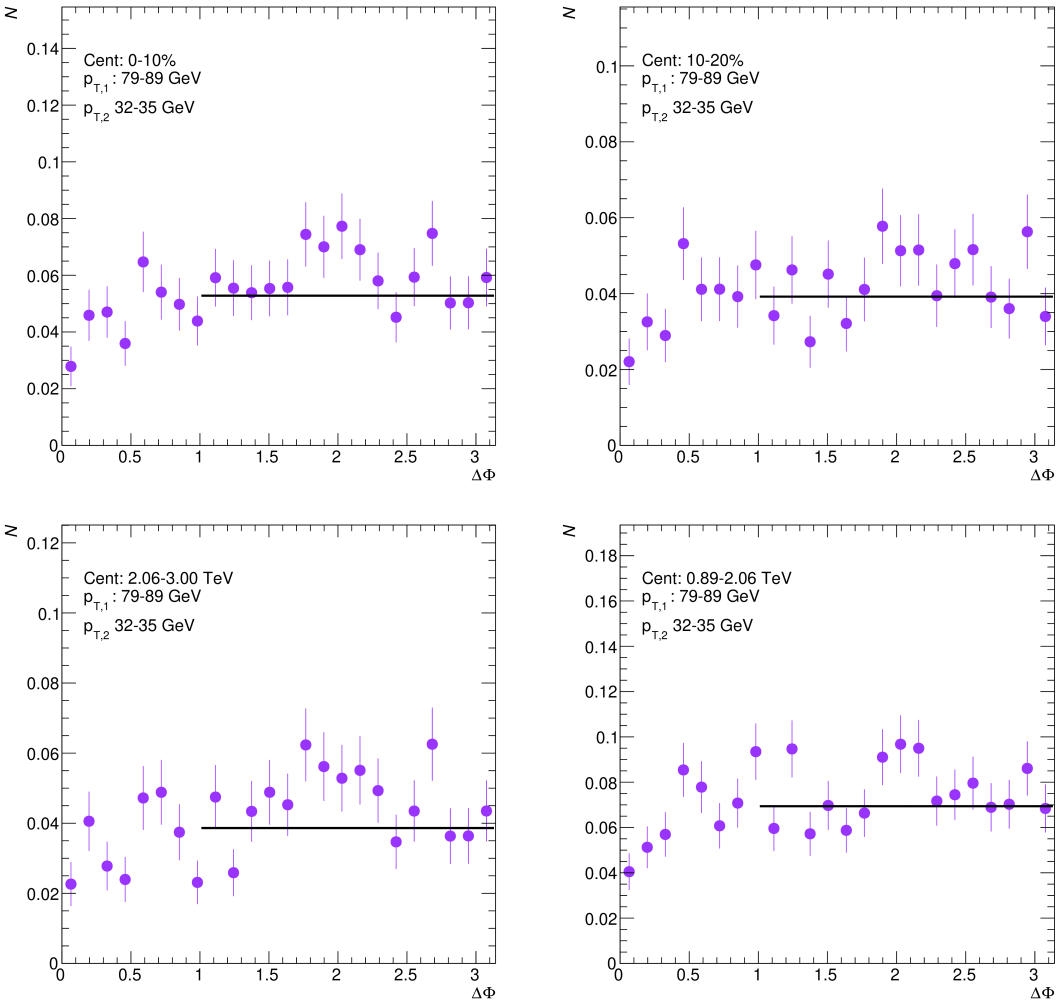

Figure 5.10: Distribution of combinatorial dijets in MC PYTHIA8 at $\sqrt{s_{\mathrm{NN}}} = 5.44$ TeV for two centrality and two $\Sigma E_{\mathrm{T}}^{\mathrm{FCal}}$ bins for one $(p_{\mathrm{T},1}, p_{\mathrm{T},2})$ bin. The distributions are fitted with a constant function, shown as a black line.

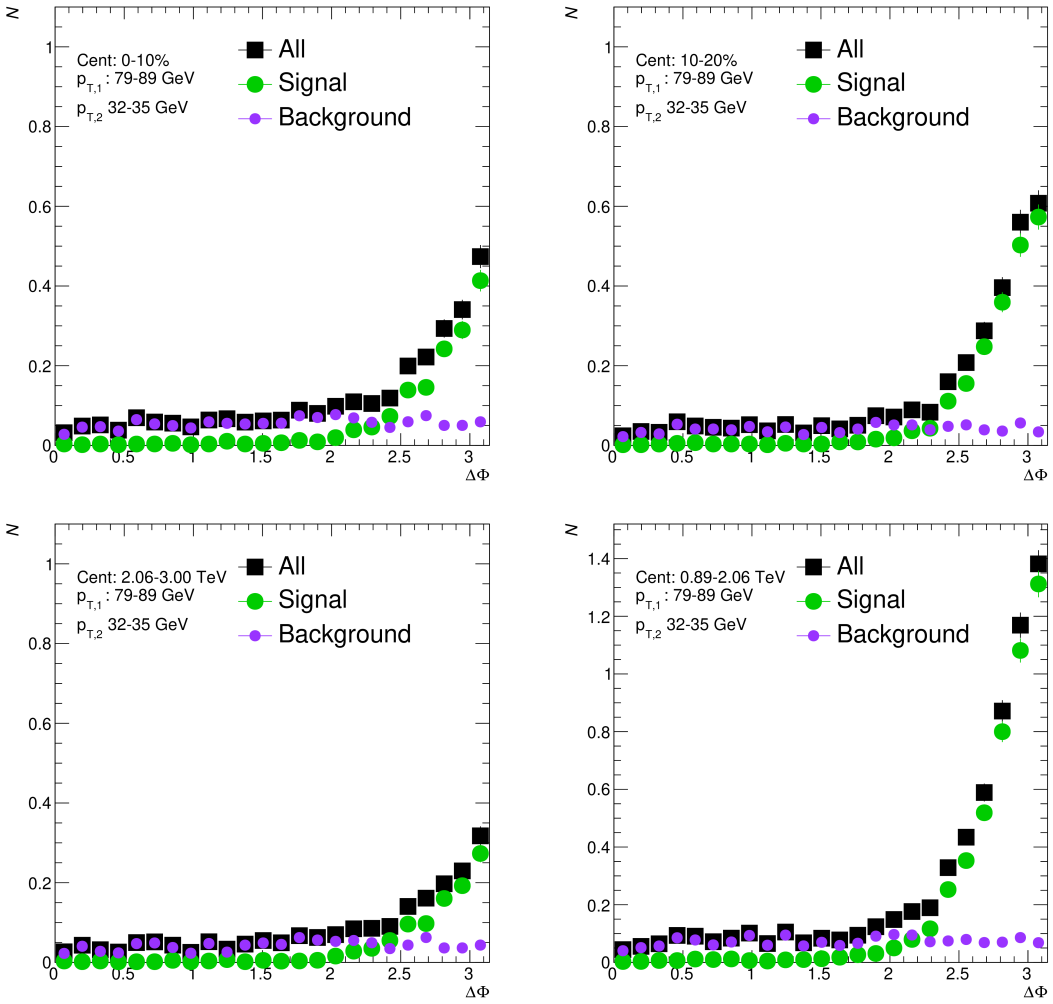

Figure 5.11: Two different bins of $\Delta\phi$ distribution in MC PYTHIA at $\sqrt{s_{\mathrm{NN}}} = 5.44$ TeV. Black — all dijets; green — signal dijets; purple — background dijets (the purple distribution in this figure is the same as the distribution in Figure 5.10).

dijets. The absolute size of the background compared to the signal in Xe+Xe collisions is shown in Figure 5.12 — here, the $(p_{\mathrm{T},1}, p_{\mathrm{T},2})$ distribution is projected onto the $p_{\mathrm{T},2}$ axis, and four $p_{\mathrm{T},1}$ bins with the most dominant background are shown. The background subtraction correction is the largest in the most central collisions and at low-p_{T} where it reaches 18%. For $p_{\mathrm{T},1} > 100$ GeV and $p_{\mathrm{T},2} > 40$ GeV the correction is smaller then 4% in the most central collisions. In other centrality bins, the background contribution is smaller than 3% for all $p_{\mathrm{T},1}$ and $p_{\mathrm{T},2}$ bins. The background size compared to the signal in MC `PYTHIA8` is shown in Figure 5.12 — here the $(p_{\mathrm{T},1}, p_{\mathrm{T},2})$ distribution is projected onto the $p_{\mathrm{T},2}$ axis, and four $p_{\mathrm{T},1}$ bins with the most dominant background are shown. The relative size of combinatorial background to signal in Xe+Xe collisions in 0–10% centrality interval is shown in Figure 5.13. This correction is the largest in the most central collisions and at low p_{T}. In 0–10% centrality interval, for $p_{\mathrm{T},1} > 100$ GeV and $32 < p_{\mathrm{T},2} < 50$ GeV, it subtracts up to 15% of dijets yields while for all other centrality and p_{T}bins, the correction subtracts less than 4% of dijet yields.

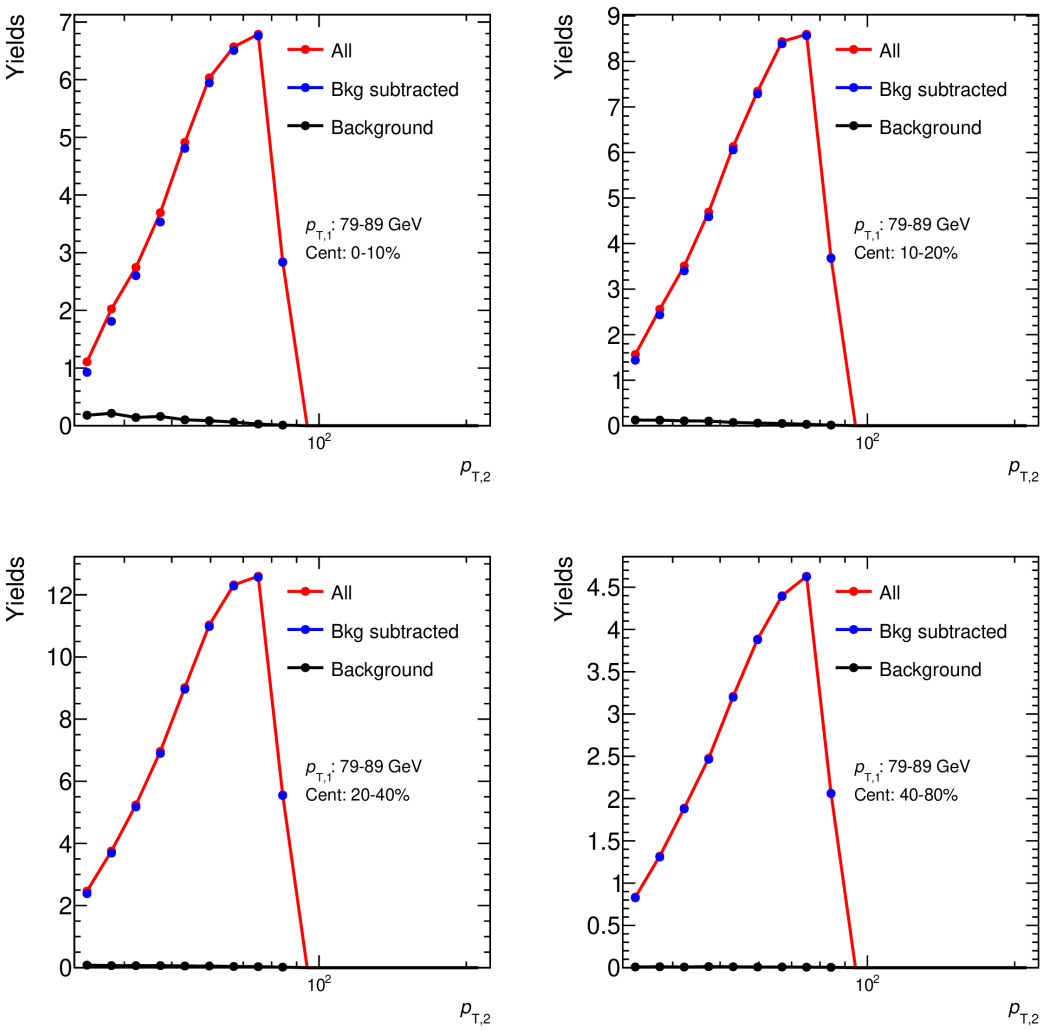

Figure 5.12: The background distribution evaluated as a function of $p_{\mathrm{T},2}$ in MC PYTHIA8 at $\sqrt{s_{\mathrm{NN}}} = 5.44$ TeV (black) compared to the signal (blue). Distributions are evaluated for four centrality intervals and for the lowest $p_{\mathrm{T},1}$ selection, where the background is the most significant.

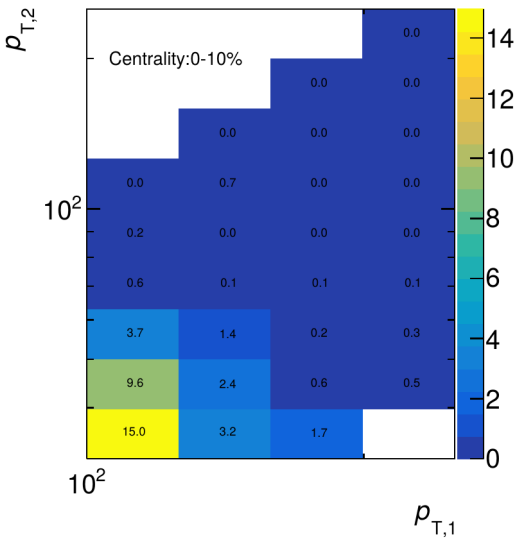

Figure 5.13: A relative size in percentage of combinatorial background in Xe+Xe collisions for 0–10% centrality interval.

5.3.2 Efficiency Correction

The combinatorial background subtraction described in the previous section leads to inefficiency because there are real pairs that have a subleading jet that has lower p_{T} than the combinatoric subleading jet. This causes the pair to be subtracted as a background when it is actually a real pair and should be considered a signal. The inefficiency was calculated by first estimating the rate at which a jet is in an event above a particular p_{T} value using the inclusive jet spectrum from the data. This rate was then used to calculate the probability this occurred zero times using the Poisson distribution for zero number of occurrences:

$$\epsilon(p_{\mathrm{T},2}) = e^{-\int_{p_{\mathrm{T}}}^{\infty} \frac{\Delta\Phi}{2\pi} \frac{\mathrm{d}N_{\mathrm{jets}}}{\mathrm{d}p_{\mathrm{T}}} \mathrm{d}p_{\mathrm{T}}}.$$

The spectrum over which one integrates is shown in Figure 5.8. This efficiency is defined as the probability for a particular value of $p_{\mathrm{T},2}$ and is independent of $p_{\mathrm{T},1}$.

Evaluated efficiencies for centrality and $\Sigma E_{\mathrm{T}}^{\mathrm{FCal}}$ intervals can be seen in Figure 5.14. The effect is the strongest in the most central collisions, and for the lowest jet $p_{\mathrm{T},2}$. With increasing $p_{\mathrm{T},2}$ the efficiency quickly approaches the unity and above $p_{\mathrm{T},2} \approx 40$ GeV is below 1% in all centralities.

The final test that gives us confidence in the whole combinatorial background procedure is shown in Figure 5.15. Here we compared signal dijets with dijets where no truth information was used. We refer to the latter as *unmatched dijets*, that is, dijets consisting of reconstructed jets, where no truth matching is applied. A closure distribution shown in the bottom panel is defined as a ratio between the selected x_{J} distribution with respect to the signal x_{J} distribution. In the figure, the closure for unmatched dijets deviates from unity more than 15% for low x_{J}. This indicates that the background contribution is the highest for low x_{J} or low $p_{\mathrm{T},2}$. After the combinatorial background subtraction is applied, the

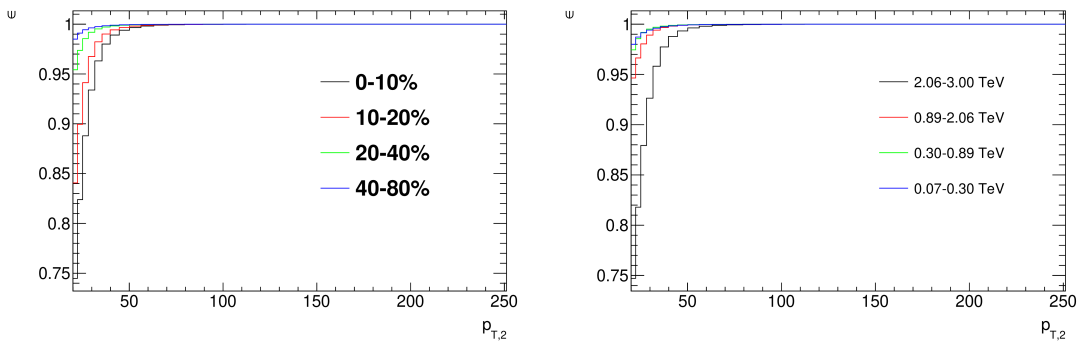

Figure 5.14: A size of efficiency correction $\epsilon(p_{\mathrm{T},2})$ in four different centrality (left) and four different $\Sigma E_{\mathrm{T}}^{\mathrm{FCal}}$ intervals (right) in Xe+Xe collisions.

closure test for subtracted x_{J} distribution is much closer to unity, and the small over subtraction is corrected by the pair efficiency correction.

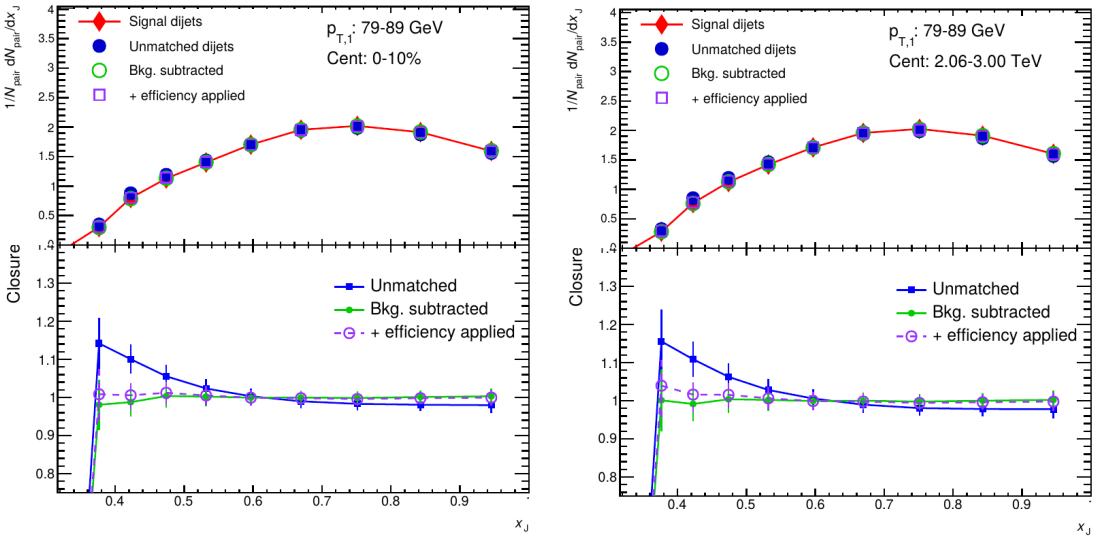

Figure 5.15: Left: Background subtraction is shown for the lowest $p_{\mathrm{T},1}$ bins used in the analysis 79-100 GeV and the most central collision interval $(0-10\%)$ as the background is the strongest for these selections. (left top) x_{J} for MC reconstructed jets: red — dijets consisting of reconstructed matched jets; blue — reconstructed all jets; green — reconstructed all jets after the background subtraction; purple — green + the efficiency correction. (left bottom) The closure test is evaluated as a ratio to the reconstructed matched distribution (red) from the top panel: Blue — closure of the unmatched reconstructed jets; green — closure after the background subtraction; purple — closure after background subtraction and the efficiency correction. Right: The same as in the left panel, but for the lowest $\Sigma E_{\mathrm{T}}^{\mathrm{FCal}}$ interval.

5.4 Unfolding

This section describes in detail the unfolding procedure used in the analysis. The unfolding has a crucial impacton on the shapes of the final distributions and the correction implementation of the unfolding was one of the most difficult parts of the analysis.

5.4.1 Response Matrix

Response matrix was represented by RooUnfoldResponse object in RooUnfold package. Because the unfolded distributions were two-dimensional, the response matrix was a four-dimensional object. The matrix was filled with `PYTHIA8` MC samples for all three JZ samples. In each event, two truth jets with the highest p_{T} were selected and tested against the following criteria:

1. both jets need to have $|y| < 2.1$
2. leading jet $p_{\mathrm{T},1} > 20$ GeV
3. subleading jet $p_{\mathrm{T},2} > 10$ GeV
4. back-to-back requirement $\Delta\Phi = |\Phi_1 - \Phi_2| > 7/8\pi$

These are the same criteria as those imposed on reconstructed jets in the analysis, with the difference that the p_{T} thresholds were lower to allow for a better matching with reconstructed jets. Dijets not fulfilling the above criteria are not used in the analysis. Both truth jets were matched to the closest reconstructed jet in $\eta \times \phi$ space with a maximum distance of $\Delta R = 0.35$. Both reconstructed jets were then matched against the criteria mentioned in the list in section 5.1. If both, truth and reco jets have required properties, the event was used and filled in the Response matrix. The filling was done symmetrically in truth and reco, to account for the switching of leading and subleading jet due to detector resolution. If the truth jets passed the requirements, but the reco jets did not (or both did not exist), the response matrix was corrected for this inefficiency.

Underlying $(p_{\mathrm{T},1}, p_{\mathrm{T},2})$ measured and truth distributions of the response matrix for four different centrality intervals are shown in Figure 5.16 and 5.17, respectively.

5.4.2 Reweighting the Response Matrix

Because `PYTHIA8` does not simulate heavy-ion environment, our measured distributions are different from the distributions in data. Thus, the reweighting procedure was applied. The weight was evaluated as a ratio between Xe+Xe data and MC `PYTHIA8` at the level of $(p_{\mathrm{T},1}, p_{\mathrm{T},2})$ distributions. This weight was then used as a function of p_{T} truth when filling the response matrix. In the edge bins where the truth distribution is populated but the reconstructed is not, the weight is extrapolated using information from higher p_{T} bins. This weight is then smoothed to remove any statistical fluctuations. Figure 5.18 shows the weight for four different centrality intervals. The effect of the reweighting on the measured x_{J} distributions is shown in Figure 5.19, where the x_{J} distribution is shown

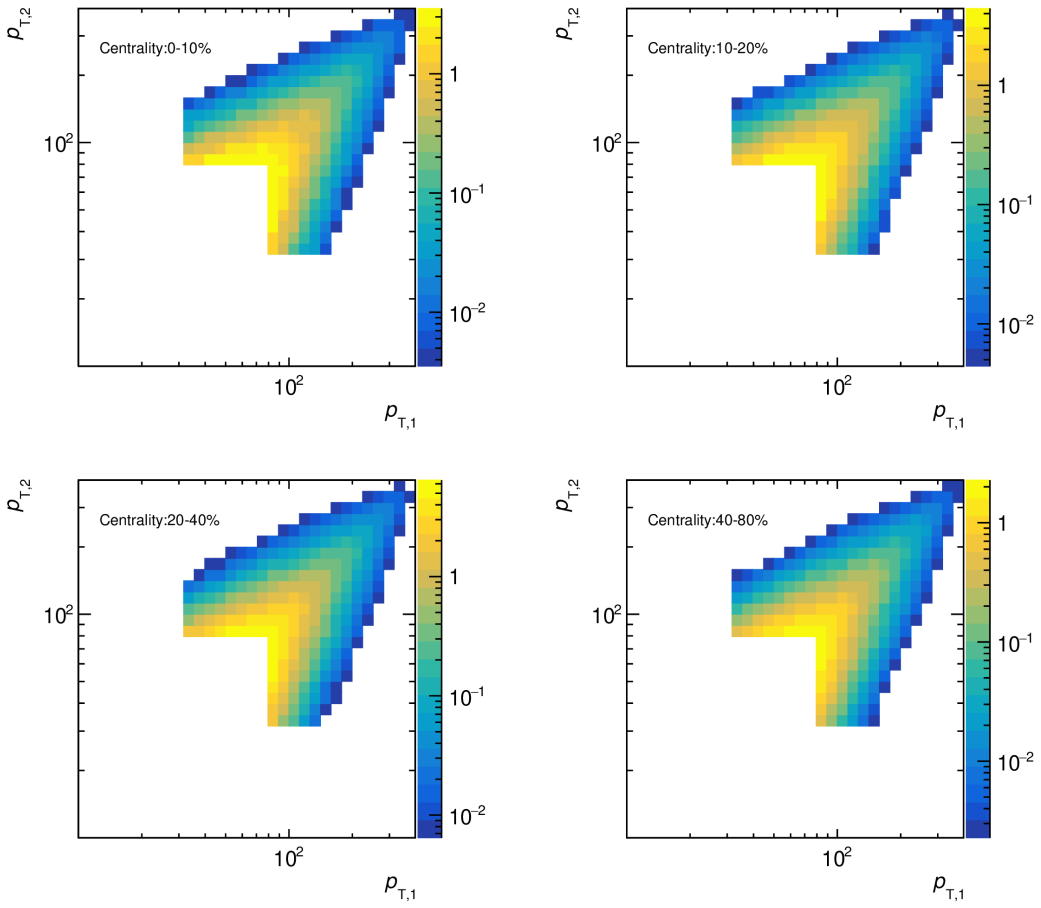

Figure 5.16: Underlying measured distributions from the response matrix in four centralities in PYTHIA8.

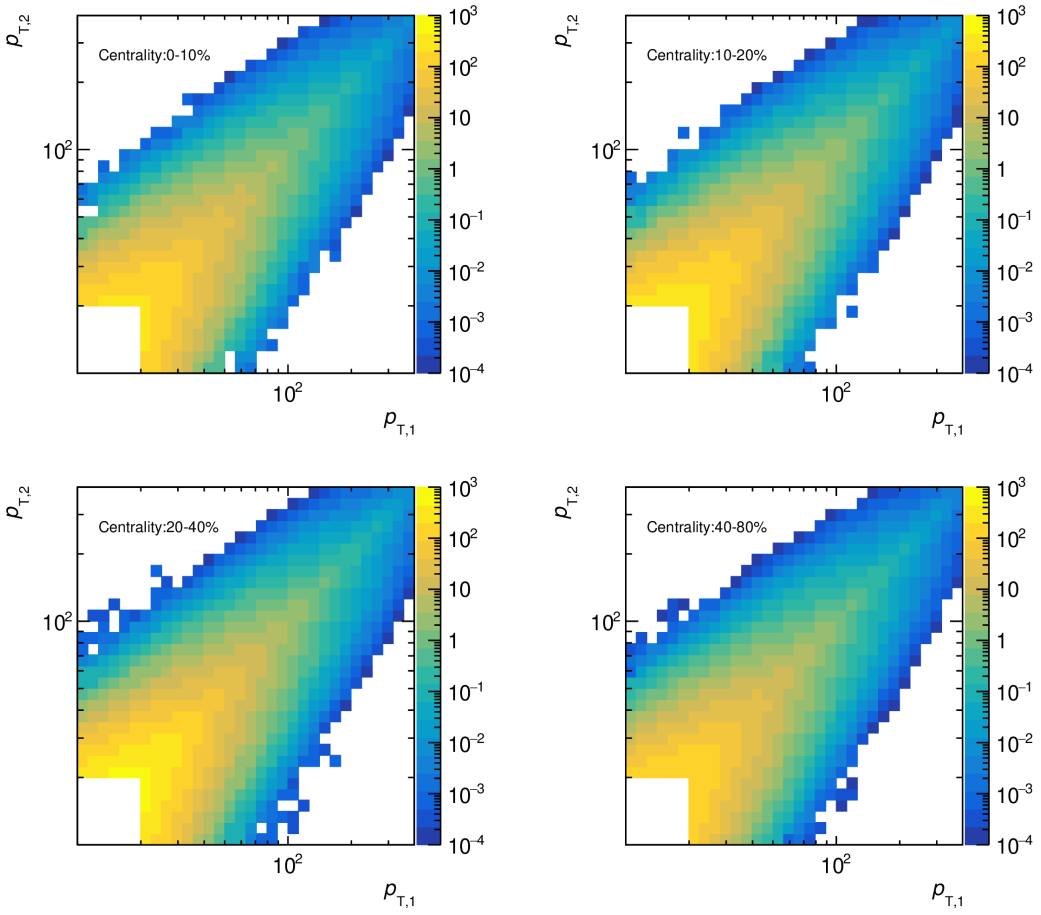

Figure 5.17: Underlying truth distributions from the response matrix in four centralities in PYTHIA8.

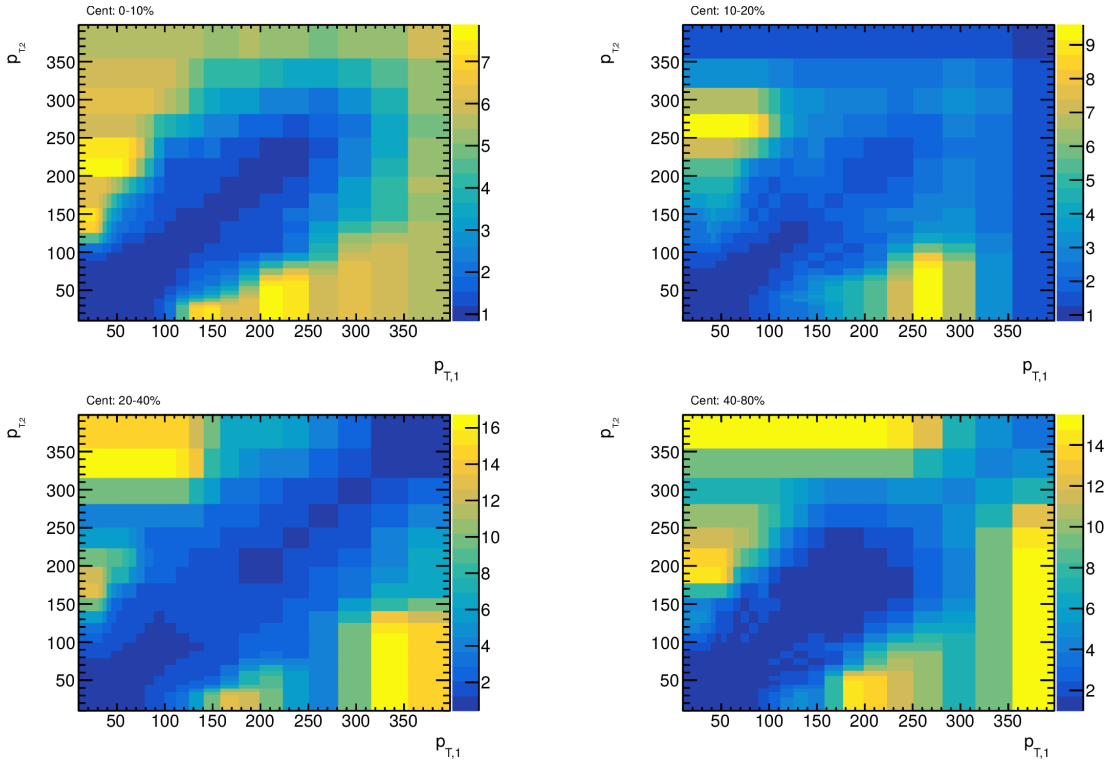

Figure 5.18: Values of the weights used to reweight the response matrix for four centrality intervals. The weights are scaled so that in each histogram, $(p_{\mathrm{T},1}, p_{\mathrm{T},2}) = (100\ \mathrm{GeV}, 100\ \mathrm{GeV})$ bin is unity.

before and after weighting as well as in measured distributions in data. From the Figure 5.19 one can see that the reweighted distribution in MC approximates the data very well. For the rest of the document, we only use the reweighted response matricies.

5.4.3 Statistical Uncertainties

This section explains how the statistical uncertainties are calculated for the unfolded results. The statistical uncertainties were evaluated with the use of pseudo-experiments, and there are two sources which contribute to the uncertainty: the reconstructed data and the response matricies. To cover these sources, two procedures were applied:

1. **Smearing of the reconstructed 2D histogram** 100 times and then unfolding each smeared version separately with the nominal response matrix. The statistical variation $\mathrm{Var}(X)$ and the standard deviation σ were calculated in each bin from the 100 different results using the standard formulas [97]:

$$\mathrm{Var}(X) = \frac{\sum X^2 - \frac{(\sum X)^2}{N}}{N-1}, \qquad \sigma = \sqrt{\mathrm{Var}(X)},$$

where X is the variable of interest and N is the sample size ($N = 100$ in our case). This smearing must reflect the initial symmetry of the $(p_{\mathrm{T},1}, p_{\mathrm{T},2})$ distributions, and therefore the smearing of the values was done symmetrically with respect to the $p_{\mathrm{T},1} = p_{\mathrm{T},2}$ diagonal.

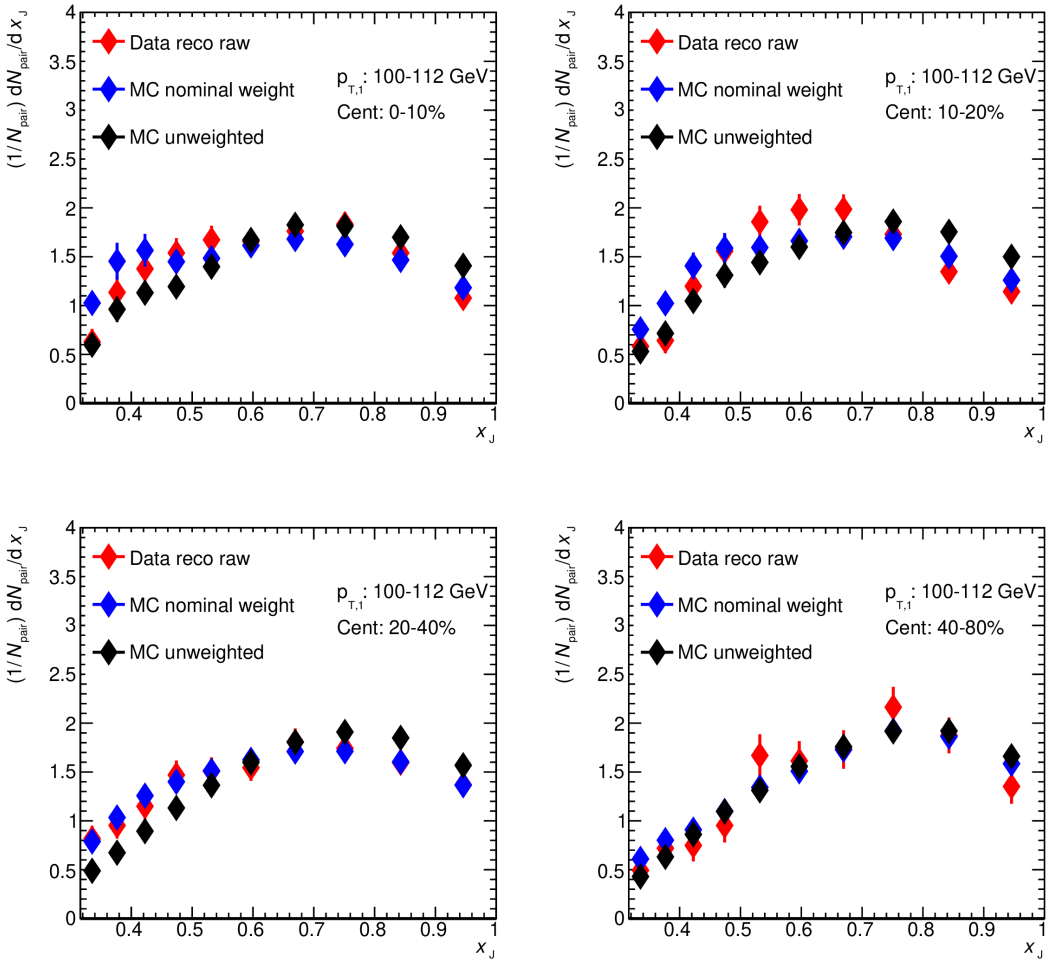

Figure 5.19: The x_{J} distributions for four different centralities and $100 < p_{\mathrm{T},1} < 112$ GeV interval. (black) and (red) is, respectively, unweighted MC and Xe+Xe data. (blue) represents weighted MC distribution using the weights from Figure 5.18.

2. **Smearing of the response matrix** 100 times and using them to unfold the nominal reconstructed $(p_{\mathrm{T},1}, p_{\mathrm{T},2})$ histogram. The same approach with the sample variance calculation was used.

Both components were summed in quadrature to get the final statistical uncertainty:

$$\sigma^{\mathrm{stat}} = \sqrt{\sigma^2_{\mathrm{hist}} + \sigma^2_{\mathrm{resp}}}.$$

Figure 5.20 shows a contribution from the two sources in a few selected bins as well as their quadrature sum. In general, the magnitude of the statistical uncertainty due to the statistical imprecision of the reconstructed data is larger than the one due to the response matrix. Figure 5.20 also shows the uncertainty evaluated by the Roounfold package. When comparing the size of the uncertainties between the RooUnfold and our method using pseudo-experiments, we see that uncertainties from the RooUnfold package are systematically underestimated. The difference between the two methods demonstrates the necessity of the pseudo-experiment procedure.

5.4.4 Selecting the Number of Iterations

As the Bayesian unfolding is an iterative procedure, some finite number of iterations has to be chosen. This is done by combining two properties:

1. The overall difference in the unfolded distributions between i^{th} and $(i-1)^{\mathrm{th}}$ iteration

$$\delta_i^{\mathrm{val}} = \sum_k^{N_{\mathrm{bins}}} \left(N_{i,k}^{\mathrm{pair}} - N_{i-1,k}^{\mathrm{pair}} \right), \tag{5.14}$$

   summed over all p_{T} bins. This quantifies the overall convergence of the unfolding.

2. The sum (again over all p_{T}) of statistical uncertainties for the i-th iteration

$$\delta_i^{\mathrm{stat}} = \sum_k^{N_{\mathrm{bins}}} \delta_{i,k}^{\mathrm{stat}}. \tag{5.15}$$

   This optimizes the total statistical uncertainty that might be significantly increased with the high number of iterations. The statistical uncertainty calculation, as described in the previous Section 5.4.3, had to be repeated for each iteration separately.

Because both δ_i^{val} and δ_i^{stat} are evaluated at the level of $(p_{\mathrm{T},1}, p_{\mathrm{T},2})$ distributions, the result is applicable to x_{J} and $\rho_{\mathrm{Xe,Pb}}$ final projections. The two distributions are summed in quadrature into the final δ_i^{tot} distribution:

$$\delta_i^{\mathrm{tot}} = \sqrt{(\delta_i^{\mathrm{val}})^2 + (\delta_i^{\mathrm{stat}})^2} \tag{5.16}$$

The final number of iterations is chosen as the minimum of the δ_i^{tot} distribution. For this analysis, δ_i^{tot} was evaluated for each iteration between 1 and 10, and 3 iterations were chosen for all centrality and $\Sigma E_{\mathrm{T}}^{\mathrm{FCal}}$ intervals. The values of δ_i^{tot} in 4 different centrality intervals are shown in Figure 5.21 and values for the $\Sigma E_{\mathrm{T}}^{\mathrm{FCal}}$ intervals are in the Appendix A, Figure A.2.

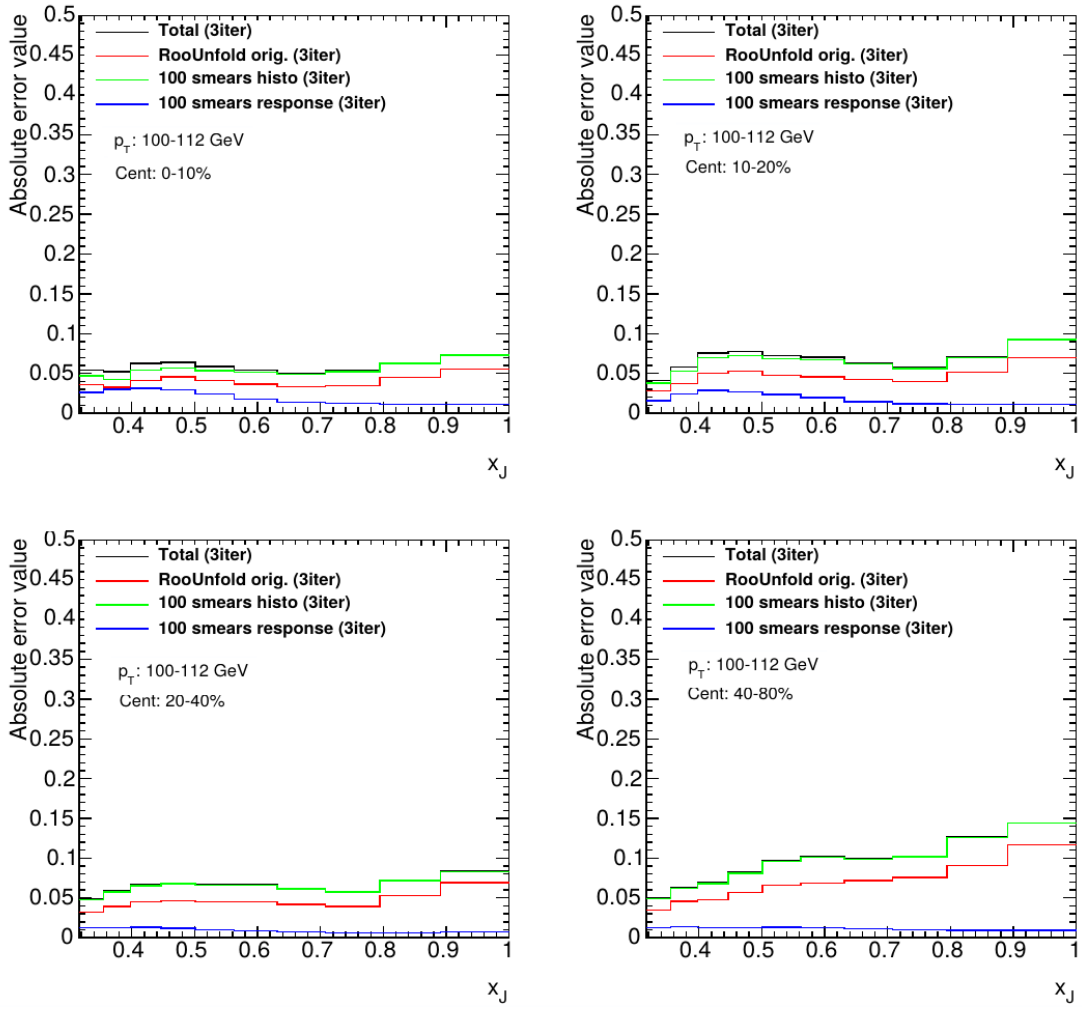

Figure 5.20: Statistical uncertainties and their components for four different centrality bins and $100 < p_{\mathrm{T},1} < 112$ GeV in Xe+Xe collisions for three iterations of the Bayesian unfolding. Green and blue lines represent components of the statistical uncertainty from the smearing histogram and response matrix, respectively, and the black line is their quadrature sum. The red line is the statistical uncertainty given by RooUnfoldBayes.

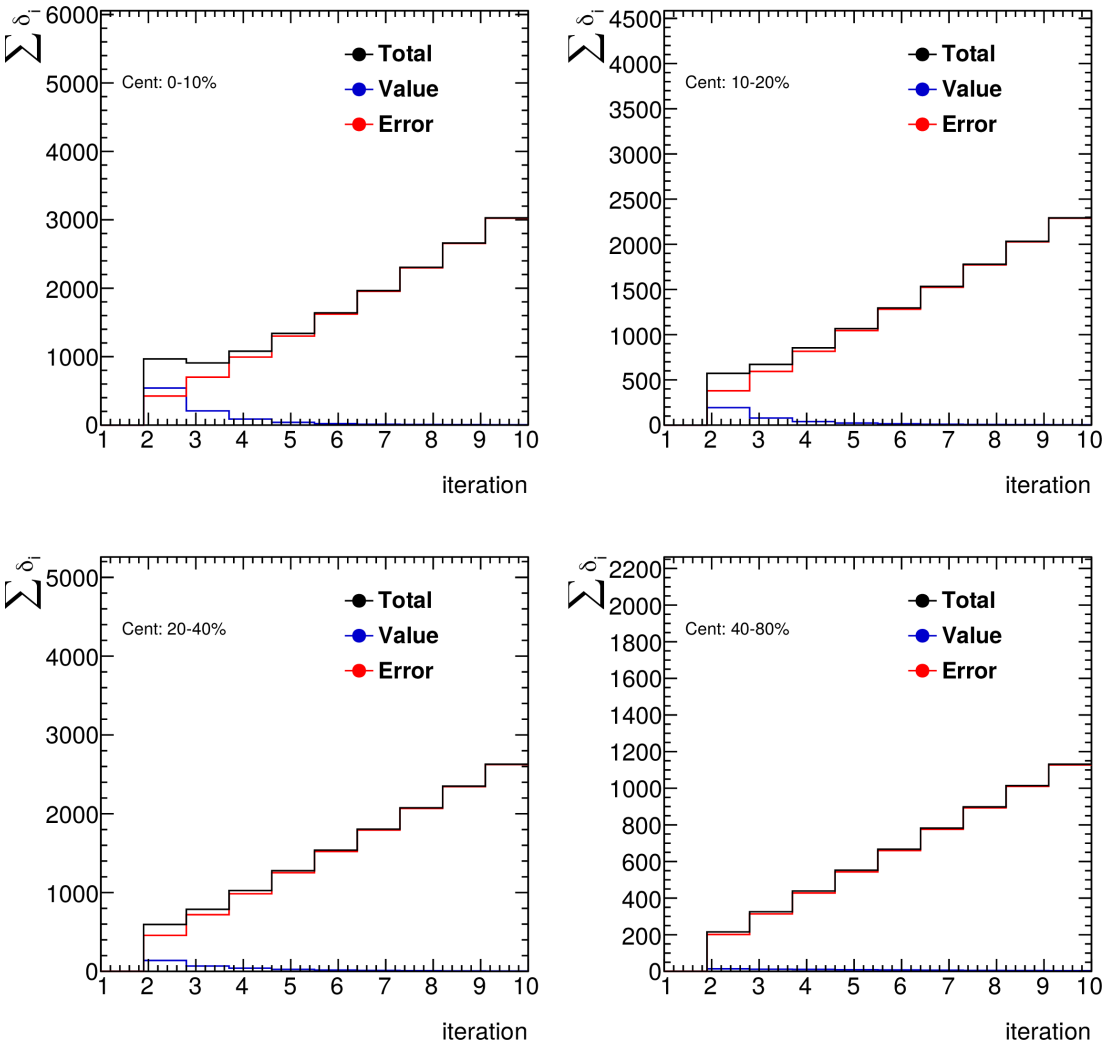

Figure 5.21: Convergence of the Bayesian unfolding in 4 centralities in Xe+Xe collisions. Blue is δ_i^{val}, red is δ_i^{stat}, and black is δ_i^{tot}; defined in Eqs. (5.14), (5.15), and (5.16).

5.4.5 MC Closure Test

In order to establish whether the unfolding procedure removes the detector resolution effects, two tests were done. We will refer to them as a *full-full* test and *half-half* test. The first one is the *full-full* test, which populates the response matrix and the measured distribution with the whole PYTHIA8 MC sample. This is a very basic test and should tell if there is any inconsistency in the treatment of the unfolding and closure. The closure, which is the ratio between the unfolded and the truth distribution, tests how good the unfolding procedure is. A good closure, well consistent with one, was observed in the full-full test.

A more informative test is the *half-half* test. Here, half of the events from the MC are used to fill the response matrix and the other half to fill the $(p_{\mathrm{T},1}, p_{\mathrm{T},2})$ measured distribution. The two halves are disjoint and statistically independent. Closure is not expected to be the exact unity, but a better unfolding procedure will be closer to it than a worse one. A closure tests result for the most central collisions $0-10\%$ and $2.06-3.0$ TeV $\Sigma E_{\mathrm{T}}^{\mathrm{FCal}}$ values are shown in Figure 5.22. The remaining centralities are in Appendix A. The most problematic region is the low-x_{J} region, where due to small absolute values of the yields, a small fluctuation can cause big non-closure (non-closure is a deviation from the unity of the closure test). Another effect is the enhanced sensitivity to the statistical variations in the response matrix due to a large number of bins being used. Due to this, the response matrix may suffer from statistical fluctuations, which then affect the closure.

As can be seen from all the closure histograms, the deviation from the unity is not always covered by statistical uncertainty, and due to this, we are taking the non-closure (that is, an absolute difference between 1 and the actual values of closure) bin-by-bin and apply it as a relative systematic on the final distributions.

5.4.6 Refolding of MC and Data

A refolding procedure is an inverse procedure to the unfolding — it applies the response matrix to the unfolded distribution. The result is a *refolded distribution* which can be compared with the raw (not unfolded) measured distribution. Such a comparison for PYTHIA8 is shown in Figure 5.23 for 0–10% centrality and $2.06-3.0$ TeV $\Sigma E_{\mathrm{T}}^{\mathrm{FCal}}$ interval. The ratio in bottom panels is well consistent with the unity except for a few bins, which can be understood as a result of statistical fluctuations in a ratio of small yields.

Figure 5.24 shows the same refolding test for Xe+Xe collisions. As expected, the ratio between the refolded and the raw distribution deviates from the unity a little bit more than for the test in PYTHIA8, but still shows good values in general. Large refolding differences from the raw measured spectrum can be mainly explained by fluctuations in data.

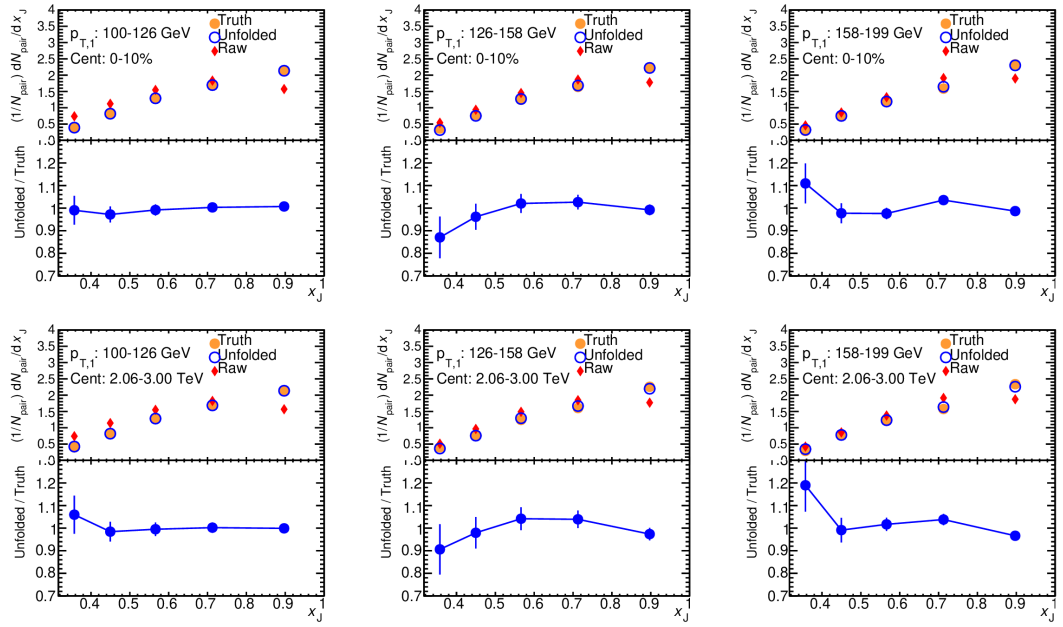

Figure 5.22: Half-half unfolding closure in PYTHIA8 for three different $p_{T,1}$ intervals. The top three panels are for $0-10\%$ centrality, and the bottom three panels are for ΣE_T^{FCal} $2.06-3.0$ TeV interval. In each panel, the top section shows truth distribution in orange circles and unfolded distribution in blue circles. The bottom section is then their closure, which is defined as a ratio of the two.

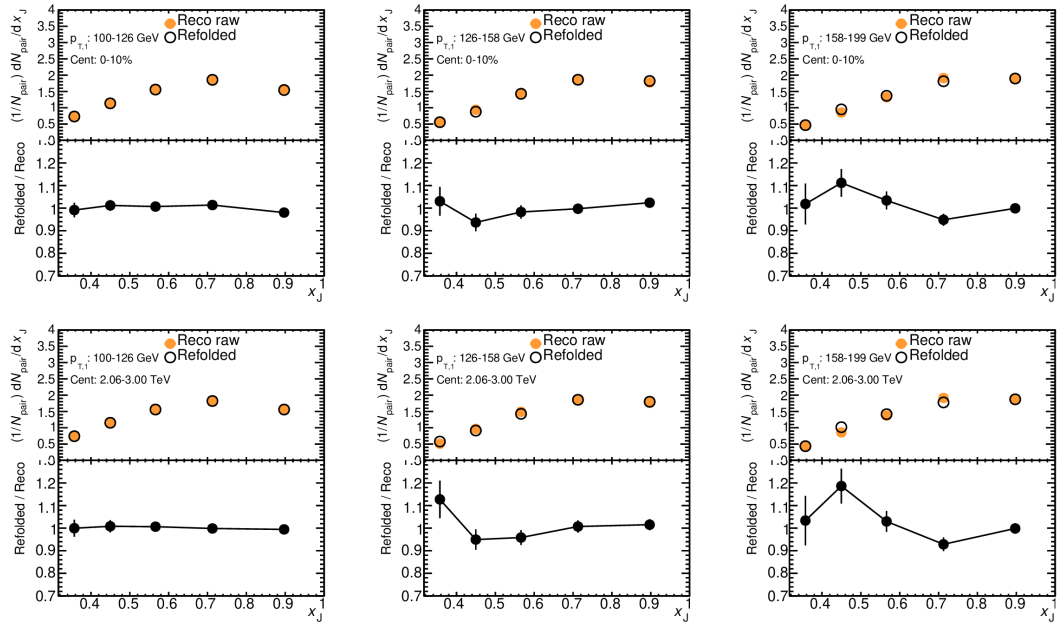

Figure 5.23: Refolding test in PYTHIA8 for $0-10\%$ centrality (top panels) and for $2.06-3.0$ TeV ΣE_T^{FCal} (bottom panels) and three different $p_{T,1}$ bins. The top panel shows the reconstructed raw x_J distribution (orange) and refolded distribution (black). The bottom panel shows the ratio refolded/reconstructed from the top panel.

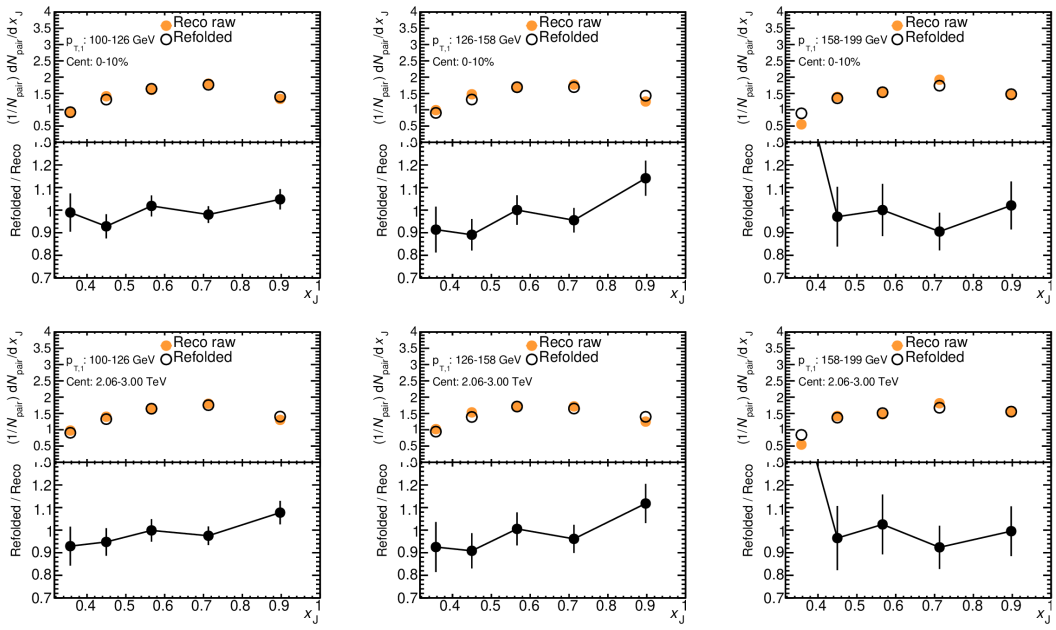

Figure 5.24: Refolding test in Xe+Xe collisions for $0-10\%$ centrality (top panels) and for $2.06-3.0$ TeV $\Sigma E_{\mathrm{T}}^{\mathrm{FCal}}$ (bottom panels) and three different $p_{\mathrm{T},1}$ bins. The top panel shows the reconstructed raw x_{J} distribution (orange) and refolded distribution (black). The bottom panel shows the ratio refolded/reconstructed from the top panel.

5.5 Systematic Uncertainties

This section discusses in detail all systematic uncertainties applied in the analysis. A summary is provided by the following list:

- Uncertainties related to jet reconstruction
  - Jet energy scale (JES)*
  - Jet energy resolution (JER)*
- Unfolding related uncertainties
  - Prior sensitivity*
  - Non-closure in MC half-half test
- Combinatorial background
  - Change in background $\Delta\Phi$ window*
  - Pair efficiency correction*
- Glauber model systematics
  - Systematic uncertainty on T_{AA} and N_{coll}
- $\rho_{\mathrm{Xe,Pb}}$ specific uncertainties

– Uncertainty on C-factors

All components of the uncertainties were evaluated and summed in quadrature to obtain the final systematic uncertainty. Uncertainties for x_{J} and $\rho_{\mathrm{Xe,Pb}}$ distribution were calculated separately. For each systematic uncertainty marked with an asterisk(*), the whole analysis procedure was repeated, including the combinatorial background subtraction and the unfolding. The uncertainty was taken as a difference between the nominal value and the value obtained after changing a specific aspect of the analysis. For uncertainties without the asterisk, the analysis does not need to be repeated, and the uncertainties were evaluated by a different method, as described below.

Jet energy scale (JES) systematic uncertainty. The uncertainty follows the recommendations used in all HI jets and consists of three main components. The first component is common with uncertainties on EMTopo jets, which are the jets used in 13 TeV *pp* collisions. The second component is specific to the heavy-ion (HI) jets and collision energies (for flavor-related uncertainties). The third part is specific to HI jets in HI collisions and reflects a modification of parton showers by the QCD matter.

The first component is established by calibrating HI jets with respect to jets reconstructed with the EMTopo procedure in nominal condition 13 TeV *pp* collisions. The component contains a set of 20 nuisance parameters, which are applied to HI reconstructed jet transverse momentum p_{T}, shifting it according to

$$p_{\mathrm{T}}^{\mathrm{jet,shifted}} = p_{\mathrm{T}}^{\mathrm{jet}} \times (1 \pm U^{\mathrm{JES}}(p_{\mathrm{T}}, \eta)),$$

where $U^{\mathrm{JES}}(p_{\mathrm{T}}, \eta)$ is JES uncertainty as evaluated by the `HIJESUncertaintyProvider` tool which is a part of ATLAS software. A cross-calibration (CC) procedure, described in Section 4.3, adds an additional cross-calibration-specific uncertainty component.

The heavy-ion-specific components are from the limitations of the CC procedure and the jet flavor uncertainties at 5.44 TeV. The former is applied using the official `JetUncertainties`tool, which is also a part of ATLAS software. The flavor-related uncertainties account for limited knowledge of the quark to gluon fractions and their responses. The uncertainty is evaluated in a standard way based on the difference between two MC generators — `PYTHIA8` and `HERWIG7`. The mean response $\langle R \rangle$ is defined as:

$$\langle R \rangle = f_{\mathrm{g}} * \langle R_{\mathrm{g}} \rangle + (1 - f_{\mathrm{q}}) * \langle R_{\mathrm{q}} \rangle, \tag{5.17}$$

where f_{g} and f_{q} are fractions of jets initiated by gluons and quarks, respectively. $\langle R_{\mathrm{g}} \rangle$ and $\langle R_{\mathrm{q}} \rangle$ are response matrices for gluons and quarks, respectively. By using the standard error propagation formula on $\langle R \rangle$ and setting quark variation to zero, because their contribution is largely accounted for in the first component, we arrive at two non-zero uncertainties:

$$\sigma_{\mathrm{response}} = \left| f_{\mathrm{g}}^{\mathrm{PYTHIA}} (R_{\mathrm{g}}^{\mathrm{PYTHIA}} - R_{\mathrm{g}}^{\mathrm{HERWIG}}) \right| \tag{5.18}$$

and

$$\sigma_{\mathrm{flavor}} = \left| (R_{\mathrm{g}}^{\mathrm{PYTHIA}} - R_{\mathrm{q}}^{\mathrm{PYTHIA}})(f_{\mathrm{g}}^{\mathrm{PYTHIA}} - f_{\mathrm{g}}^{\mathrm{HERWIG}})/\langle R \rangle \right|. \tag{5.19}$$

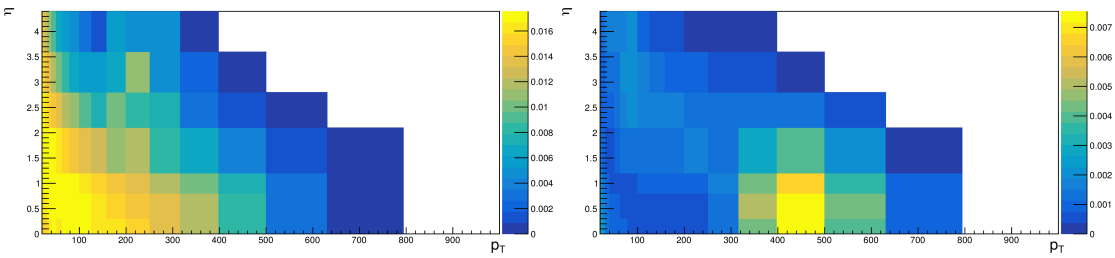

Figure 5.25: Flavour uncertainties as a function of η and p_{T}. The z-axis shows the relative uncertainty of (left) flavor response and (right) flavor fraction.

Figure 5.25 shows η- and p_{T}-dependence of uncertainties as they are defined in Equations (5.18) and (5.19).

The last component is the centrality-dependent "quenching" component that reflects a modification of parton showers by the HI environment. The resulting jets may have different flavor compositions or, more generally, different particle content. The impact of this on the JES was estimated using a data-driven study of the ratio of p_{T} of the calorimeter jet to the p_{T} of the corresponding track jet. The recommendation is to include uncertainty on the jet energy scale, which is a linear function of the event centrality. The uncertainty was adapted from Pb+Pb collisions and was applied as a function of $\Sigma E_{\mathrm{T}}^{\mathrm{FCal}}$ on Xe+Xe data. The uncertainty is a linear function of the event centrality — 1.25% in the most central 0–1% Pb+Pb collisions with linear decrease as a function of $\Sigma E_{\mathrm{T}}^{\mathrm{FCal}}$ to 0% uncertainty for events corresponding to 80% centrality in Pb+Pb.

The Xe+Xe data is unfolded with altered response matrices, and the variation in the unfolded yields is taken as the systematic uncertainty. For the x_{J} distributions, the size of JES uncertainty is approximately 1–8% with the maximum for $x_{\mathrm{J}} \approx 0.32$ in the most central 0–10% collisions. The uncertainty decreases with x_{J} but increases again for the last bin at $x_{\mathrm{J}} = 1$, where it reaches about 2%. For the $\rho_{\mathrm{Xe,Pb}}$ distributions, the JES systematic shows weak $p_{\mathrm{T},1}$ or $p_{\mathrm{T},2}$ dependence and reaches maximal values of 5%.

Jet energy resolution (JER) systematic uncertainty. The unfolding procedure was repeated with a modified response matrix to account for systematic uncertainties due to disagreement between the jet energy resolution in data and MC. The matrix was generated by repeating the MC study with modifications to the Δp_{T} for each matched reconstructed-truth jet pair. The procedure to generate modified migration matrices follows the recommended procedure at ATLAS. The `JetUncertainties` tool was used to retrieve uncertainty on the fractional resolution, $\sigma_{\mathrm{JER}}^{\mathrm{syst}}$, as a function of jet p_{T} and η. A simple JER set of parameters is used. An additional HI jet-specific uncertainty from the cross-calibration of the HI jet collections is applied to jets in Xe+Xe collisions. This involves modifications of every component to account for missing Global Sequential Calibration in the HI calibration sequence and from a dedicated uncertainty accounting for the difference in relative resolutions between HI and EMTopo jets in MC and data.

The reconstructed jet transverse momentum p_{T} was smeared by the official

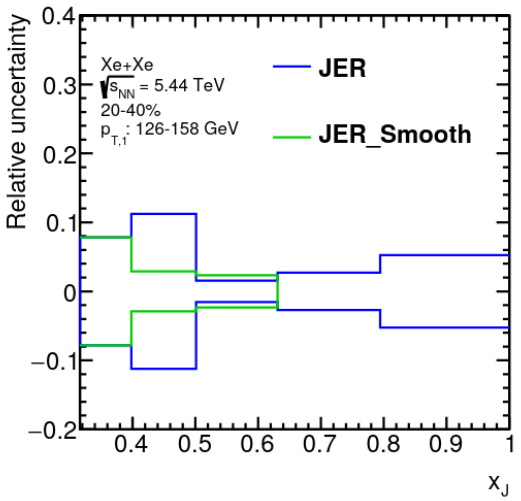

Figure 5.26: Example of smoothing procedure in one selected p_{T} and centrality bin. The blue line represents original JER relative uncertainties, while the green line is the uncertainty after the smoothing procedure.

`JetUncertainties` tool according to the equation:

$$p_{\mathrm{T}}^{\mathrm{jet,smear}} = p_{\mathrm{T}}^{\mathrm{jet}} \times (1 \pm \mathcal{N}_{\mathrm{JER}}^{\mathrm{syst}}(1, \sigma_{\mathrm{JER}}^{\mathrm{sys}})),$$

where $\mathcal{N}_{\mathrm{JER}}^{\mathrm{syst}}(1, \sigma_{\mathrm{JER}}^{\mathrm{syst}})$ is the normal distribution with an effective resolution $\sigma_{\mathrm{JER}}^{\mathrm{eff}} = \sqrt{(\sigma_{\mathrm{JER}} - \sigma_{\mathrm{JER}}^{\mathrm{sys}})^2 - \sigma_{\mathrm{JER}})}$. The resulting JER uncertainty is then symmetrized so that up and down variations have the same size but different signs. For comparison, JES can have different sizes for up and down variations.

Individual JER components are summed in quadrature and a sliding window smearing procedure was used to remove statistical fluctuations. Figure 5.26 shows an example of JER uncertainties before and after the smoothing in one selected bin.

The JER uncertainty for x_{J} distributions is approximately 9% for $x_{\mathrm{J}} \approx 0.32$ in the most central collisions. The uncertainty decreases with x_{J}, except for the last two bins, where it increases again to values of approximately 5%. For the $\rho_{\mathrm{Xe,Pb}}$ distributions, the JER uncertainty is at most 2% and shows weak p_{T} dependence.

The final JES uncertainty and smoothed JER uncertainty were summed in quadrature to obtain the combined JES+JER uncertainty that we show in the final figures.

Prior sensitivity. The unfolding procedure should not depend on the choice of the prior, but because of the limited statistics, statistical fluctuations are present. This systematic uncertainty should cover this imperfection. The whole analysis is repeated for an unweighted response matrix, as opposed to the nominal response matrix, which is weighted by the weight described in Section 5.4.2. The difference between the two is taken as a systematic uncertainty. The uncertainty is then symmetrized to have up and down components. The maximum contribution from this uncertainty is about 10% for the x_{J} distributions and approximately 5% for $\rho_{\mathrm{Xe,Pb}}$ distributions.

Non-closure in MC. To quantify some additional imperfections of the Bayesian unfolding procedure, an additional uncertainty based on the half-half unfolding closure test was added. This should cover the unknown uncertainties which are coming from the unfolding and should complement the prior sensitivity uncertainty above. The size of the uncertainty is the size of the non-closure unfolding test shown in Figure 5.22.

Change in the background window. The systematic is evaluated by changing the background window we use to evaluate the combinatorial background. The nominal $\Delta\Phi$ background window, $1.0 < \Delta\Phi < 1.4$, was shifted to an alternative window, $1.1 < \Delta\Phi < 1.5$. This change varies the contribution of the flow modulation and any residual contribution from the dijet signal leaking into the background region. The whole analysis is repeated with this shifted background, and the difference in the final unfolded result is taken as the uncertainty. This uncertainty typically does not exceed 5% contribution for both x_{J} and $\rho_{\mathrm{Xe,Pb}}$ distributions. At low x_{J} the uncertainty can reach a few tens of percents due to statistical fluctuations in the non-closure.

Pair efficiency correction. The correction itself was discussed in Section 5.3.2. Since the correction is small and based on a statistical estimate of the effect, for the systematic uncertainty, the whole analysis is repeated without this correction. The difference in the final unfolded results between with and without the correction is taken as a systematic uncertainty. Like the previous one, this uncertainty is subdominant in all bins used in the analysis and does not exceed 2%.

Systematic uncertainties coming from T_{AA} and N_{coll}. The uncertainty on the T_{AA} and N_{coll} arise from geometric modeling uncertainty (e.g., Woods-Saxon parameterization of the nucleon positions, nucleon-nucleon inelastic cross-section) and the uncertainty on the fraction of selected inelastic Xe+Xe and Pb+Pb collisions (the "efficiency" uncertainty). This uncertainty does not depend on jet kinematics and only affects the overall normalization. The values of these uncertainties are tabulated in Table 5.1 for Xe+Xe and Table 5.2 for Pb+Pb.

Collision Energy. This uncertainty comes from an uncertainty of $\mathcal{C}(p_{\mathrm{T},1})$, $\mathcal{C}(p_{\mathrm{T},2})$ and $\mathcal{C}(x_{\mathrm{J}})$ coefficients. The coefficients were evaluated in two MC generators: `HERWIG7` and `PYTHIA8`. Both were applied to the distributions separately, and the difference in the final result was taken as an absolute uncertainty. The uncertainty was then symmetrized to obtain up and down variations. This uncertainty is below 2% for all p_{T} intervals and is independent of the event centrality.

5.5.1 Systematic Uncertainty on the x_{J} Distribution

The above-discussed systematic uncertainties were computed for the x_{J} distribution, and the results for per-pair normalized x_{J} distributions for all centrality and p_{T} bins are presented in Figure 5.27. Systematic uncertainties for per-pair normalized x_{J} distributions in $\Sigma E_{\mathrm{T}}^{\mathrm{FCal}}$ intervals, absolutely normalized x_{J} distribution in centrality intervals, and absolutely normalized x_{J} distributions in $\Sigma E_{\mathrm{T}}^{\mathrm{FCal}}$ inter-

vals are shown in Appendix A and Figures A.3, A.4, and A.5, respectively. There is no difference between the per-pair and absolutely normalized x_{J} distributions, except that the absolutely normalized ones have an additional uncertainty on T_{AA}. Systematic uncertainties are dominated by JES+JER and prior sensitivity uncertainties in all $p_{\mathrm{T},1}$ and centrality bins. MC closure systematic has a bigger contribution in more central collisions. High values of the relative uncertainties at low x_{J} bins are caused by low yields in these bins, where a small difference in absolute yields will cause a high relative difference. For $x_{\mathrm{J}} \gtrapprox 0.5$, total systematic uncertainty is smaller than 10%.

5.5.2 Systematic Uncertainty on the $\rho_{\mathrm{Xe,Pb}}$ Ratio

When evaluating systematic uncertainties on the $\rho_{\mathrm{Xe,Pb}}$ ratio, JES and JER uncertainties were correlated between Xe+Xe and Pb+Pb systems. They were calculated with the formula for a function of the ratio of two quantities, $f = A/B$:

$$\delta f^{\pm}|_{\mathrm{C}} = \frac{A \pm \delta A}{B \pm \delta B} - \frac{A}{B}. \tag{5.20}$$

All other systematic uncertainties were uncorrelated between the two systems, and for their calculation, the following formula was used instead:

$$\delta f = \frac{A}{B}\sqrt{\left(\frac{\delta A}{A}\right)^2 + \left(\frac{\delta B}{B}\right)^2}. \tag{5.21}$$

Figures 5.28 and 5.29 show the relative uncertainties for centrality and $\Sigma E_{\mathrm{T}}^{\mathrm{FCal}}$ intervals, respectively. Systematics in $\rho_{\mathrm{Xe,Pb}}$ are dominated by JES+JER uncertainties. In selected bins, MC non-closure also has a significant contribution. Systematics do not show any trend and are smaller than approximately 10% in all reported p_{T} and centrality bins.

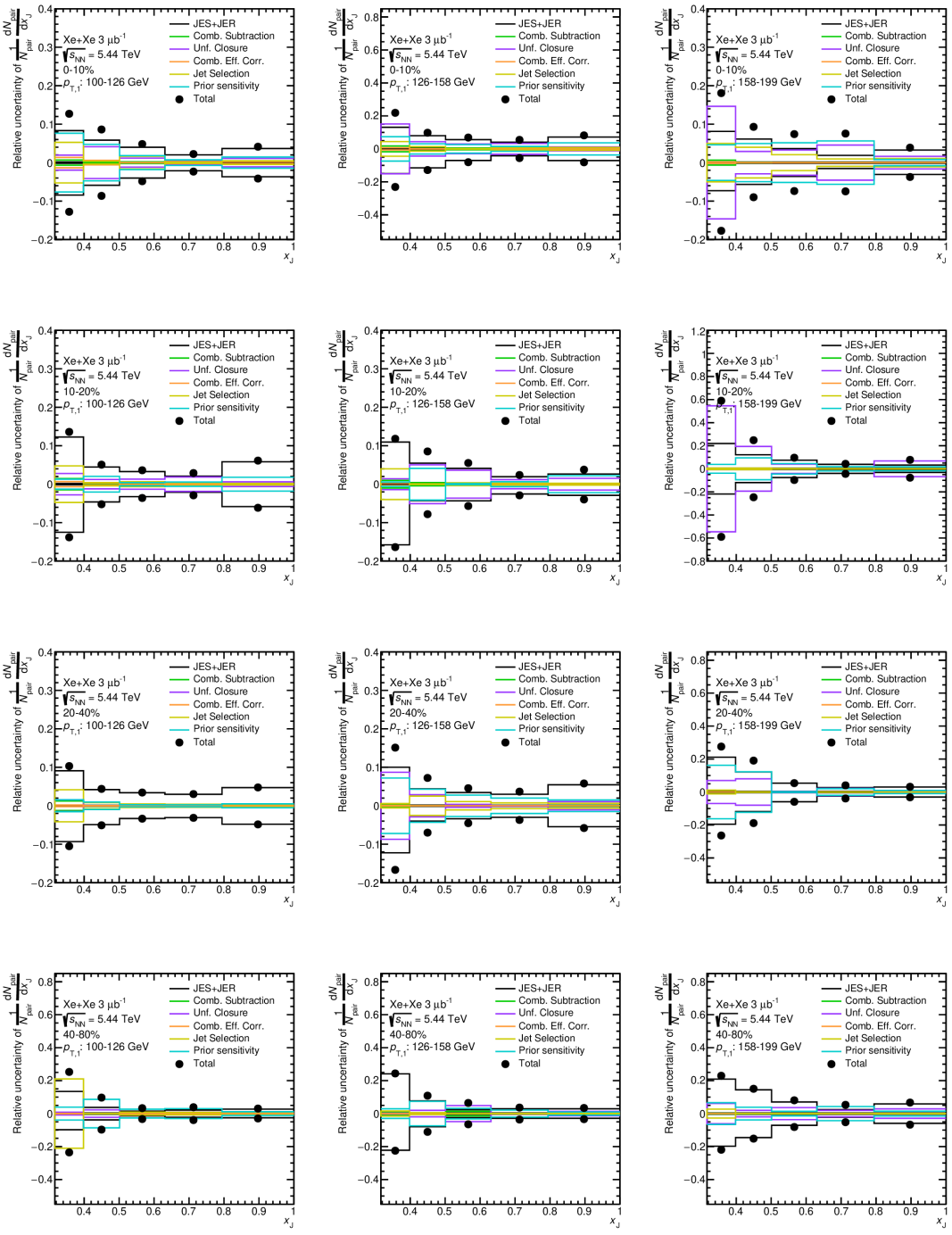

Figure 5.27: Systematic uncertainties on x_J distribution for four different centralities and three different leading jet p_T in Xe+Xe collisions at $\sqrt{s_{NN}} = 5.44$ TeV.

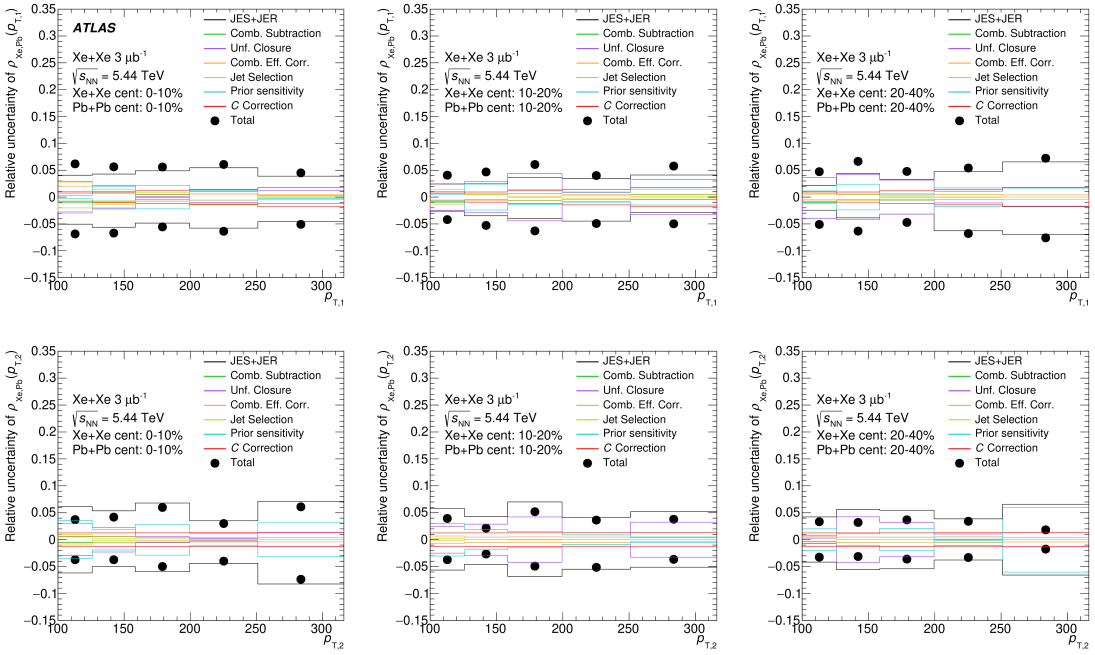

Figure 5.28: Systematic uncertainties on $\rho_{\mathrm{Xe,Pb}}$ in Xe+Xe collisions at $\sqrt{s_{\mathrm{NN}}} = 5.44$ TeV. The top and the bottom row shows leading and subleading jets, respectively, for three centrality intervals.

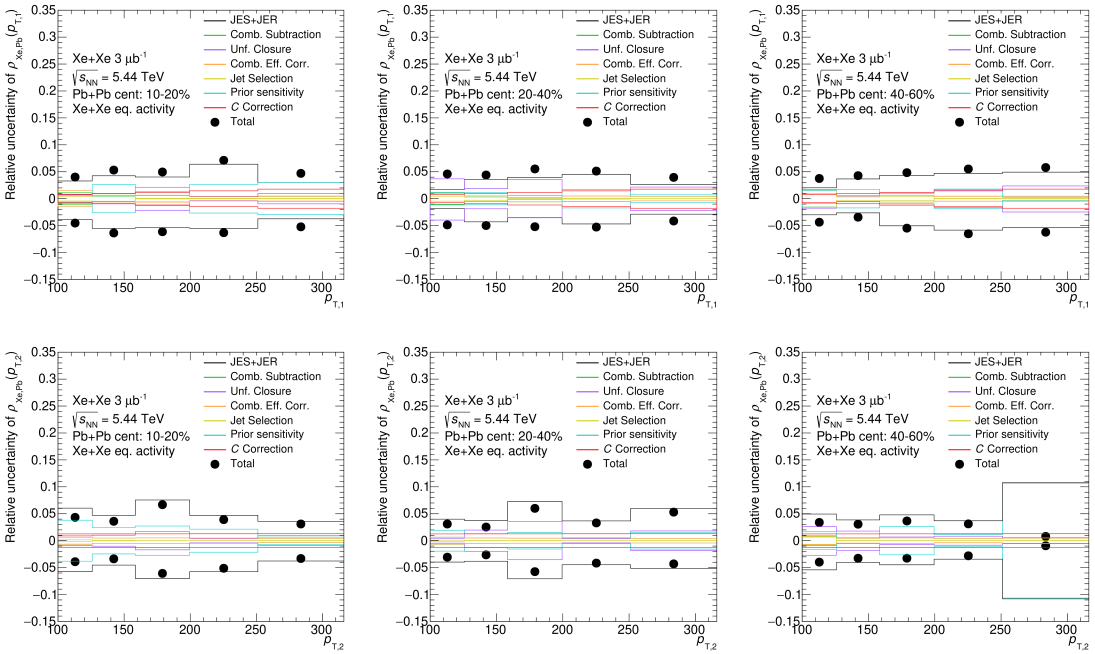

Figure 5.29: Systematic uncertainties for $\rho_{\mathrm{Xe,Pb}}$ in Xe+Xe collisions at $\sqrt{s_{\mathrm{NN}}} = 5.44$ TeV. The top and the bottom row shows leading and subleading jets, respectively, for three $\Sigma E_{\mathrm{T}}^{\mathrm{FCal}}$ intervals.

5.6 Results

Figure 5.30 shows the unfolded per-pair normalized x_J distributions evaluated in four centrality intervals: 0–10%, 10–20%, 20–40%, and 40–80%, and three $p_{T,1}$ intervals: $100 < p_{T,1} < 126$ GeV, $126 < p_{T,1} < 158$ GeV, and $158 < p_{T,1} < 199$ GeV. A substantial difference in the shape of x_J distributions is seen between the most central collisions (0–10%) and the most peripheral collisions (40–80%). In peripheral collisions, the most frequent configurations are balanced dijets, while in central collisions, the rate of imbalanced dijets is the same or higher than the rate of balanced dijets. Narrowing of the x_J distribution with increasing $p_{T,1}$ is also observed for all centrality classes. These features were observed in Pb+Pb collisions as well [15]. The peak structure at $x_J = 0.6$ previously measured in 0–10% Pb+Pb collisions is, however, not present in 0–10% Xe+Xe collisions, which may be connected with a smaller overlapping region of colliding nuclei in Xe+Xe compared to Pb+Pb collisions. The evolution between the central and peripheral Xe+Xe collisions is not as pronounced as in Pb+Pb collisions. The absence of a clearly visible evolution is connected with a worse statistical precision of the Xe+Xe measurement compared to Pb+Pb measurement.

Figure 5.31 shows the same distributions as Figure 5.30, but evaluated in four ΣE_T^{FCal} intervals. A similar broadening of the x_J distribution is seen when comparing central ($2.06 - 3$ TeV) and peripheral collisions ($0.07 - 0.3$ TeV).

Figure 5.32 shows a comparison between Xe+Xe and Pb+Pb in matching centrality intervals (e.g., $0 - 10\%$ for both Xe+Xe and Pb+Pb collisions) for three centrality and three $p_{T,1}$ intervals. The biggest difference between the two systems is in the most central collisions (0–10%) and the lowest $p_{T,1}$ interval $100 < p_{T,1} < 126$ GeV, where the above-mentioned peak at $x_J \approx 0.6$ in Pb+Pb collisions is not seen in the Xe+Xe collisions. The smaller systematic uncertainties reported for lower statistic Xe+Xe collisions are connected with the coarser binning used in Xe+Xe data, which brought smaller bin-to-bin migrations and, consequently, smaller systematic uncertainties related to the unfolding procedure.

To compare the x_J distribution between Xe+Xe and Pb+Pb in an unbiased way, the x_J distributions were evaluated in intervals of the same event activity,

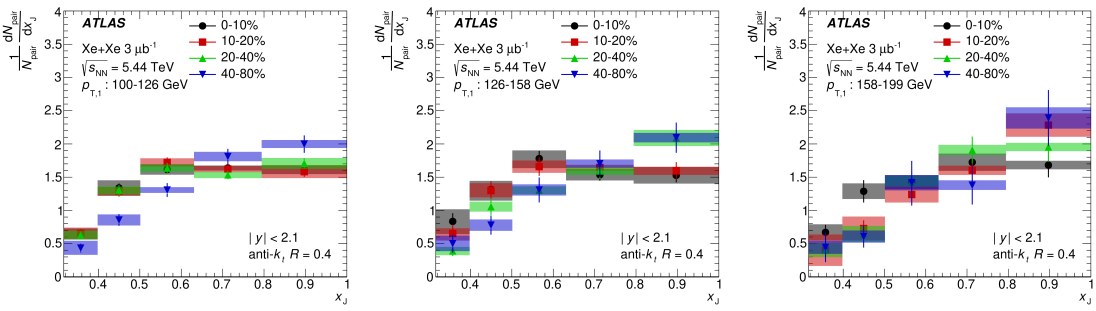

Figure 5.30: The unfolded per-pair normalized x_J distribution evaluated in four centrality intervals and three $p_{T,1}$ intervals : $100 < p_{T,1} < 126$ GeV (left), $126 < p_{T,1} < 158$ GeV (middle), and $158 < p_{T,1} < 199$ GeV (right). Statistical and systematic uncertainties are represented by error bars and colored boxes, respectively.

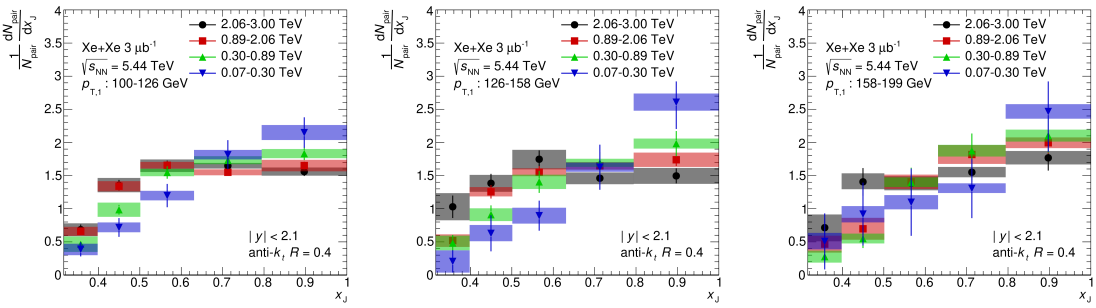

Figure 5.31: The unfolded per-pair normalized x_{J} distribution evaluated in four $\Sigma E_{\mathrm{T}}^{\mathrm{FCal}}$ intervals and three $p_{\mathrm{T},1}$ intervals: $100 < p_{\mathrm{T},1} < 126$ GeV (left), $126 < p_{\mathrm{T},1} < 158$ GeV (middle), and $158 < p_{\mathrm{T},1} < 199$ GeV (right). Statistical and systematic uncertainties are represented by error bars and colored boxes, respectively.

quantified by $\Sigma E_{\mathrm{T}}^{\mathrm{FCal}}$. The choice of $\Sigma E_{\mathrm{T}}^{\mathrm{FCal}}$ intervals matches those measured in Pb+Pb for centrality intervals 10–20%, 20–40%, and 40–60%. The corresponding centrality intervals in Xe+Xe collisions are given in Table 5.2. The most central Pb+Pb interval (0–10%) cannot be used since the equivalent event activity is not present in Xe+Xe collisions. The Xe+Xe to Pb+Pb comparison of per-pair normalized x_{J} distributions is presented in Figure 5.33 in three centrality and three $p_{\mathrm{T},1}$ intervals: $100 < p_{\mathrm{T},1} < 126$ GeV, $126 < p_{\mathrm{T},1} < 158$ GeV, and $158 < p_{\mathrm{T},1} < 199$ GeV. The distributions measured within the same event activity interval are consistent between Xe+Xe and Pb+Pb collisions.

Figure 5.34 shows the absolutely normalized distribution of x_{J} evaluated for the same centrality and $p_{\mathrm{T},1}$ selection as in Figure 5.30. It is observed that the relative enhancement of imbalanced dijet topologies seen in Figure 5.30 is due to the depletion in the absolute yield of balanced dijets — an observation valid also in the Pb+Pb measurement. Results in Figure 5.34 exhibit a clear centrality evolution where the suppression of balanced dijet yield gradually decreases from central to peripheral collisions.

The comparison of absolutely normalized x_{J} distributions between Pb+Pb and Xe+Xe in the same event activity intervals is presented in the upper panels of Figure 5.35. A clear difference between Xe+Xe and Pb+Pb distributions can be seen, with Xe+Xe having a larger absolute yield than Pb+Pb. This difference may be partially attributed to the difference in hard process cross-section due to the different center-of-mass energy of the initial hard scattering between Xe+Xe and Pb+Pb collisions. To estimate the impact of the difference in the center-of-mass energy, the absolutely normalized x_{J} distributions in Pb+Pb collisions are scaled by $\mathcal{C}(x_{\mathrm{J}})$ defined in Equation (5.4). The scaled result is shown in the bottom panels of Figure 5.35. After correcting for the difference in the center-of-mass energy of the initial hard scattering, the absolutely normalized x_{J} distributions agree between the two systems within uncertainties. The same conclusion is also found for other $p_{\mathrm{T},1}$ intervals, which are shown in Appendix A (Figures A.6 and A.7). While the observed agreement could arise due to canceling effects and large uncertainties, a natural explanation for this behavior is that the difference in the energy of the hard scattering process plays a significant role in

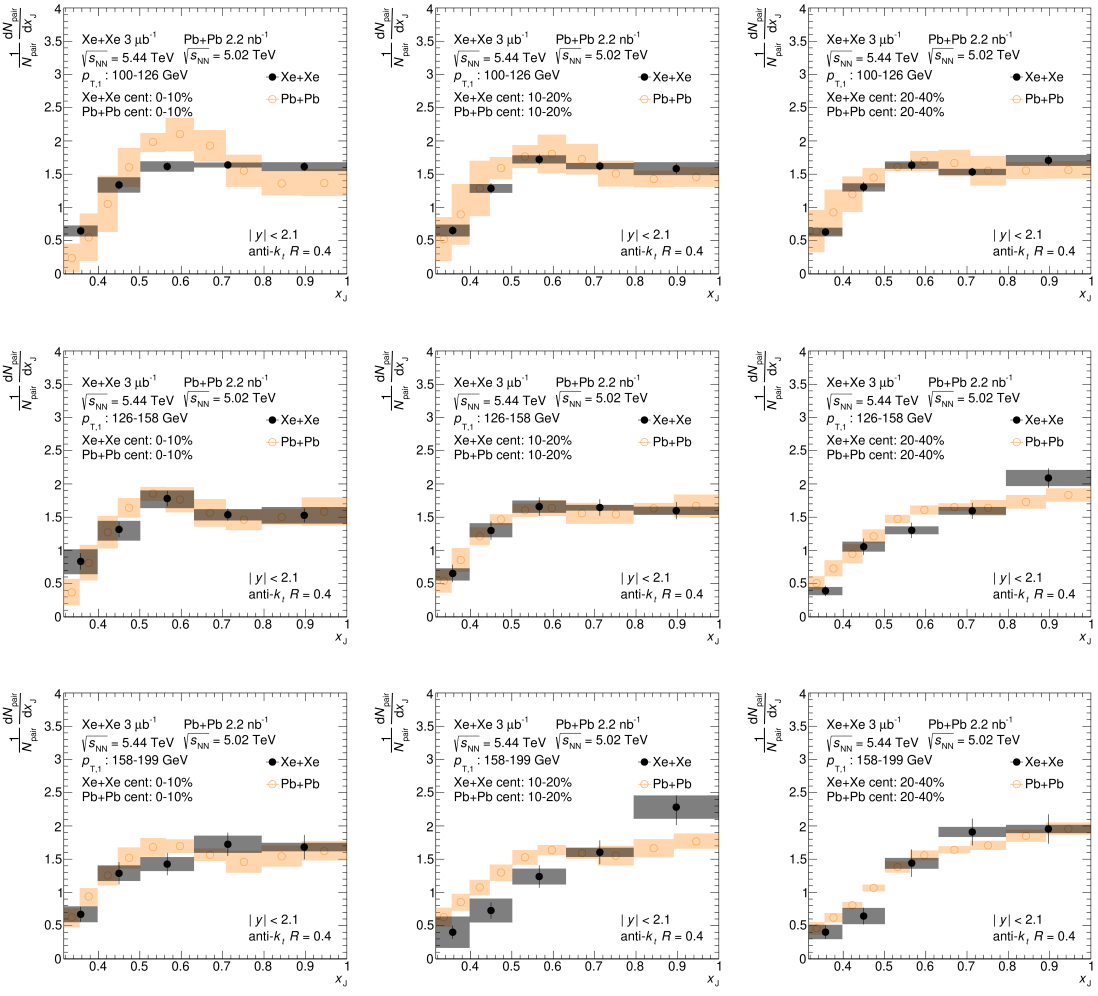

Figure 5.32: Comparison of Xe+Xe (black) and Pb+Pb (orange) per-pair normalized x_{J} distribution in three $p_{\mathrm{T},1}$ intervals (rows: $100 < p_{\mathrm{T},1} < 126$ GeV (top), $126 < p_{\mathrm{T},1} < 158$ GeV (middle), and $158 < p_{\mathrm{T},1} < 199$ GeV (bottom)) and three Xe+Xe centrality intervals (columns: 10–20% (right), 20–40% (middle), 40–60% (right)) and in the same Pb+Pb centrality intervals. Statistical and systematic uncertainties are represented by error bars and colored boxes, respectively.

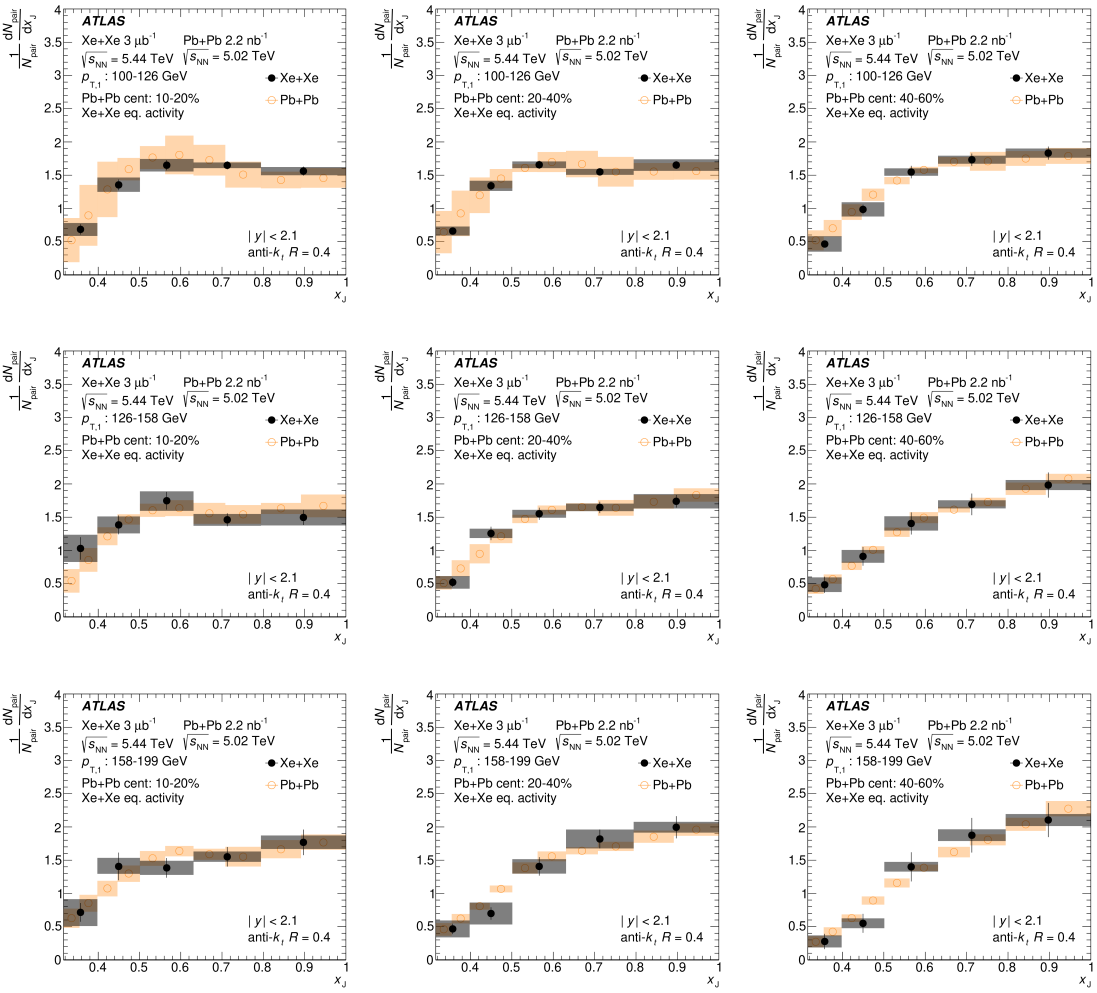

Figure 5.33: Comparison of Xe+Xe (black) and Pb+Pb (orange) per-pair normalized x_{J} distribution in three different $p_{\mathrm{T},1}$ intervals (rows: $100 < p_{\mathrm{T},1} < 126$ GeV (top), $126 < p_{\mathrm{T},1} < 158$ GeV (middle), and $158 < p_{\mathrm{T},1} < 199$ GeV (bottom)) and three Pb+Pb centrality intervals (columns: 10–20% (right), 20–40% (middle), 40–60% (right)) and in the corresponding Xe+Xe $\Sigma E_{\mathrm{T}}^{\mathrm{FCal}}$ intervals. Statistical and systematic uncertainties are represented by error bars and colored boxes, respectively.

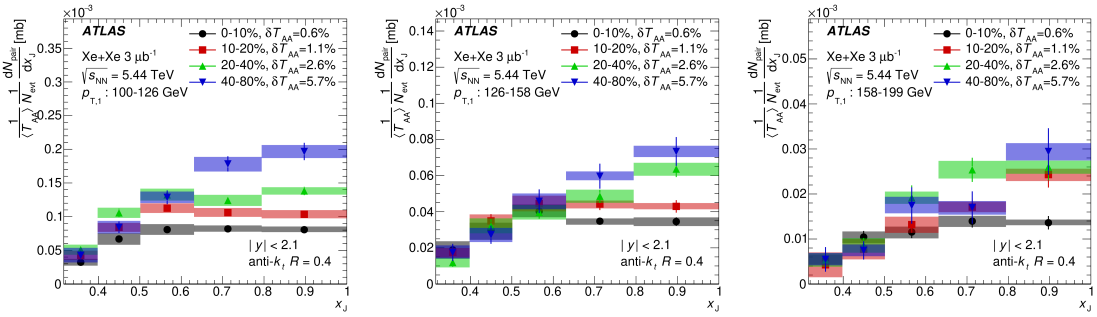

Figure 5.34: Absolutely normalized x_{J} distribution evaluated in four centrality intervals and three $p_{\mathrm{T},1}$ intervals: $100 < p_{\mathrm{T},1} < 126$ GeV (left), $126 < p_{\mathrm{T},1} < 158$ GeV (middle), and $158 < p_{\mathrm{T},1} < 199$ GeV (right). Statistical and systematic uncertainties are represented by error bars and colored boxes, respectively.

absolutely normalized x_{J} distributions.

In the case of per-pair normalized x_{J} distributions, the correction factor $\mathcal{C}(x_{\mathrm{J}})$ was found to be consistent with unity. This agrees with observing an agreement of per-pair normalized x_{J} distributions between Xe+Xe and Pb+Pb collisions.

To characterize the differences between Xe+Xe and Pb+Pb dijet suppression in a more quantitative way, we evaluate the Xe+Xe to Pb+Pb ratio of pair nuclear modification factors, $\rho_{\mathrm{Xe,Pb}}$ defined in Section 5.1. The $\rho_{\mathrm{Xe,Pb}}(p_{\mathrm{T},1})$ and $\rho_{\mathrm{Xe,Pb}}(p_{\mathrm{T},2})$ evaluated in the same Xe+Xe and Pb+Pb centrality intervals are shown in Figure 5.36. The obtained $\rho_{\mathrm{Xe,Pb}}$ values are systematically larger than unity typically by 10% to 20% depending on centrality. The $\rho_{\mathrm{Xe,Pb}}$ distributions evaluated in the same event activity intervals are shown in Figure 5.37. In contrast to the centrality-based comparison, $\rho_{\mathrm{Xe,Pb}}$ values are consistent with unity within statistical and systematic uncertainties. This implies that the pair nuclear modification factor in Xe+Xe collisions at $\sqrt{s_{\mathrm{NN}}} = 5.44$ TeV is consistent with the same quantity measured at $\sqrt{s_{\mathrm{NN}}} = 5.02$ TeV in Pb+Pb collisions, which suggests that the suppression of dijets does not differ in a significant way between Xe+Xe and Pb+Pb collisions when measured in the same event activity intervals.

Despite the above-mentioned consistency of $\rho_{\mathrm{Xe,Pb}}$ with the unity, we note that it is not possible to directly interpret the difference between the pair R_{AA} evaluated as a function of $p_{\mathrm{T},1}$ and $p_{\mathrm{T},2}$ as the difference between the overall suppression of leading and subleading jets. The reason is that the yields entering the pair R_{AA} are conditional yields mutually dependent on kinematic selection criteria. Consequently, any interpretation of $\rho_{\mathrm{Xe,Pb}}(p_{\mathrm{T},1})$, $\rho_{\mathrm{Xe,Pb}}(p_{\mathrm{T},2})$ and $R_{\mathrm{AA}}^{\mathrm{pair}}(p_{\mathrm{T},1})$, $R_{\mathrm{AA}}^{\mathrm{pair}}(p_{\mathrm{T},2})$ needs to be done within theoretical model predictions, which directly follow the dijet definition and projection procedures described in this publication.

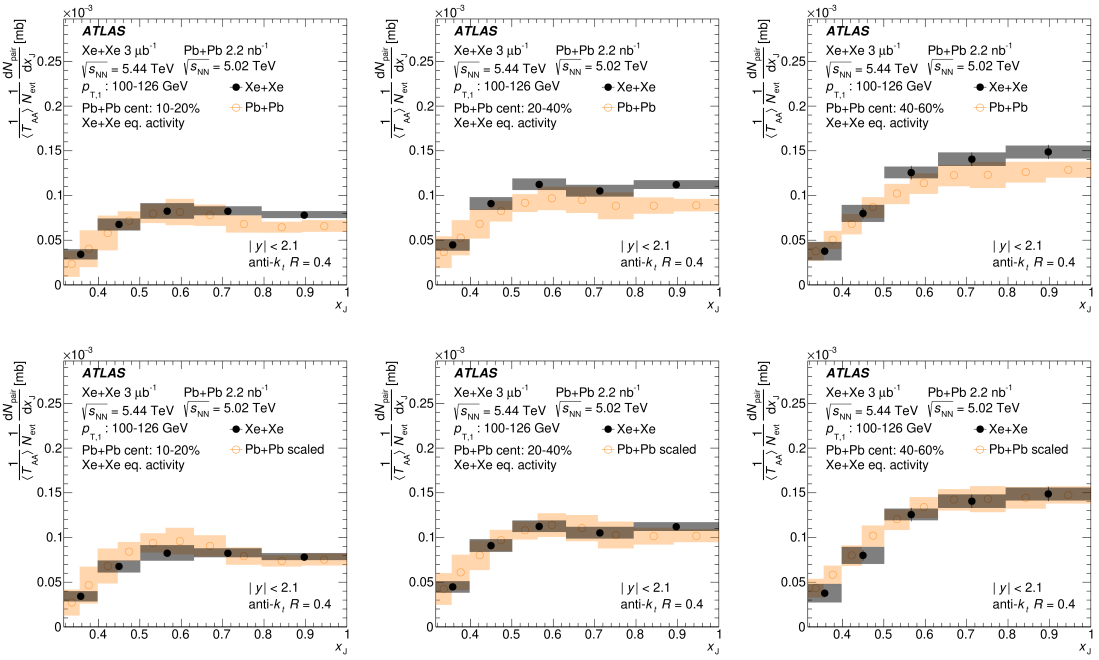

Figure 5.35: Comparison of Xe+Xe (black) and Pb+Pb (orange) absolutely normalized x_{J} distribution in $100 < p_{\mathrm{T},1} < 126$ GeV and 10–20%, 20–40%, and 40–60% Pb+Pb centrality interval and in the corresponding Xe+Xe $\Sigma E_{\mathrm{T}}^{\mathrm{FCal}}$ intervals. The upper panels show directly measured distributions. The lower panels show Pb+Pb distribution corrected for the impact of the difference in the center-of-mass energy of the hard scattering process between Xe+Xe and Pb+Pb collisions (see text). Statistical and systematic uncertainties are represented by error bars and colored boxes, respectively.

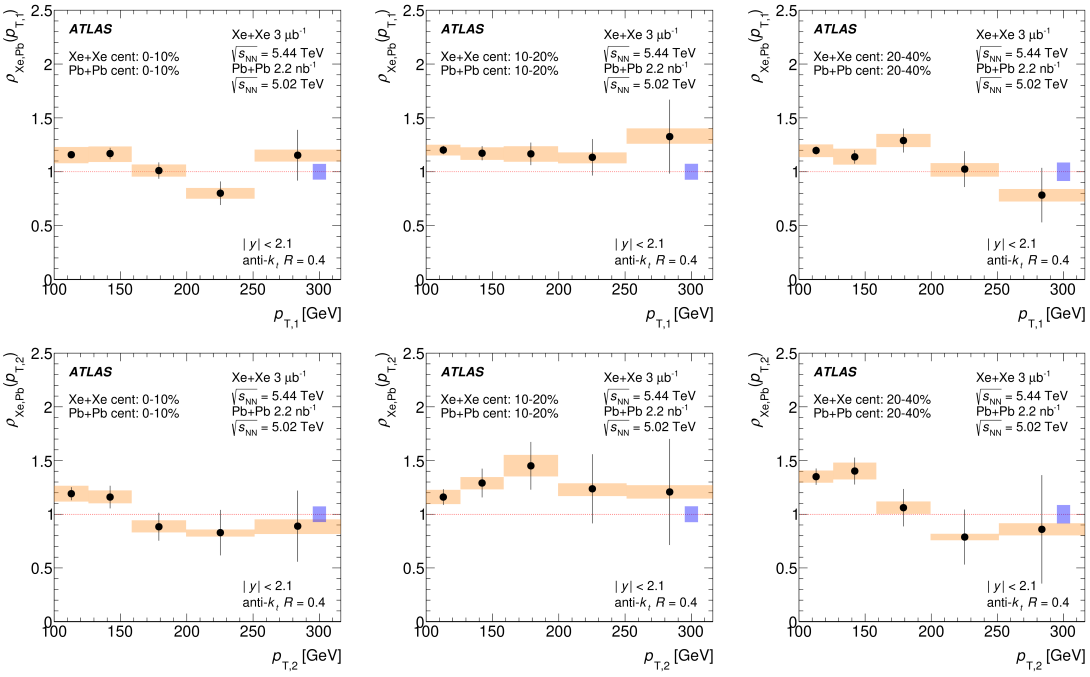

Figure 5.36: Ratio of Xe+Xe and Pb+Pb pair nuclear modification factors, $\rho_{\mathrm{Xe,Pb}}$, evaluated as a function of $p_{\mathrm{T},1}$ (upper panels) and $p_{\mathrm{T},2}$ (lower panels) in the same centrality intervals. Statistical and systematic uncertainties are represented by error bars and colored boxes, respectively. The blue box represents systematic uncertainty on $\langle T_{\mathrm{AA}} \rangle$.

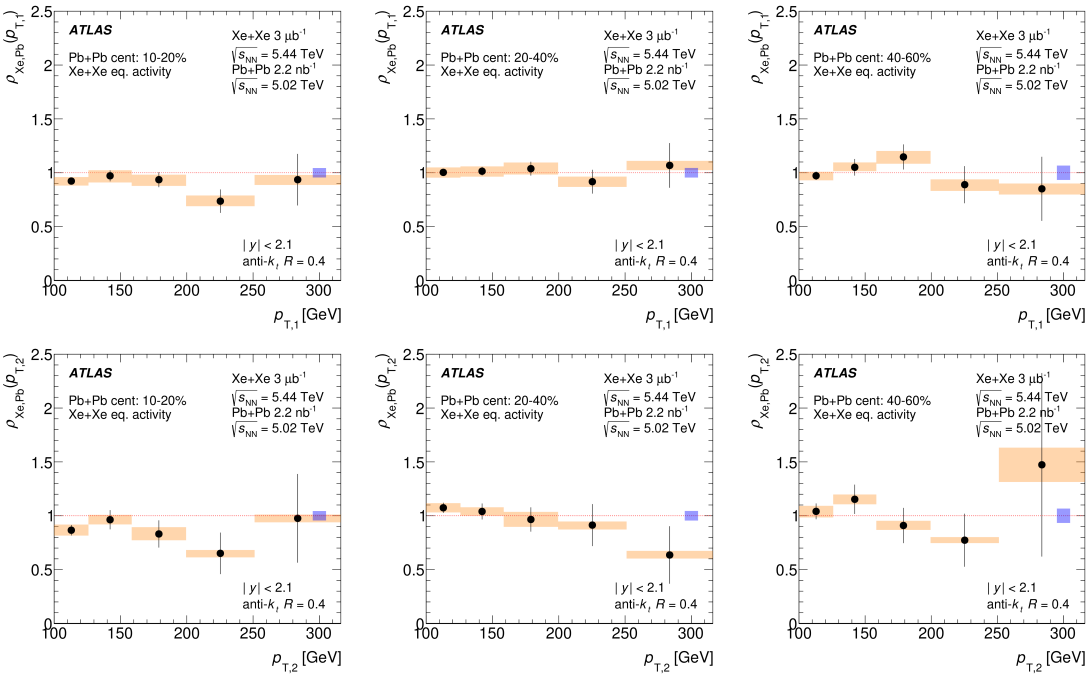

Figure 5.37: Ratio of Xe+Xe and Pb+Pb pair nuclear modification factors, $\rho_{\mathrm{Xe,Pb}}$, evaluated as a function of $p_{\mathrm{T},1}$ (upper panels) and $p_{\mathrm{T},2}$ (lower panels) in the same $\Sigma E_{\mathrm{T}}^{\mathrm{FCal}}$ intervals (selecting equivalent event activity). Statistical and systematic uncertainties are represented by error bars and colored boxes, respectively. The blue box represents systematic uncertainty on $\langle T_{\mathrm{AA}} \rangle$.

Conclusion

The measurement of dijet balance in Xe+Xe collisions at $\sqrt{s_{\mathrm{NN}}} = 5.44$ TeV is provided in terms of per-pair normalized x_{J} distributions and absolutely normalized x_{J} distributions obtained using data collected by the ATLAS detector at the LHC.

A higher relative rate of imbalanced dijets in central Xe+Xe collisions compared to peripheral collisions is seen in the per-pair normalized x_{J} distributions. The absolutely normalized x_{J} distributions then show that this feature arises predominantly from a decrease in the yields of more balanced dijets with x_{J} values close to 1.

The results are compared to the already published measurement of dijets in Pb+Pb collisions at $\sqrt{s_{\mathrm{NN}}} = 5.02$ TeV done by ATLAS. The x_{J} distributions are found to be consistent between Pb+Pb and Xe+Xe collisions when compared in the same event activity intervals and after correcting the absolutely normalized distributions for the expected difference in hard cross-section due to the different center-of-mass energy between Xe+Xe and Pb+Pb collisions.

An alternative evaluation of the dijet suppression between the Xe+Xe and Pb+Pb collisions is provided by the ratios of pair nuclear modification factors, $\rho_{\mathrm{Xe,Pb}}$, which are found to be consistent with unity when evaluated in the same event activity intervals.

These results should bring a better understanding of the role of path-length, energy density, and fluctuations in the jet energy loss in the QGP and add a new input to quantifying its system size dependence.

List of Publications

The author of this thesis is the principal analyzer and contact editor of the dijet momentum balance analysis discussed in Chapter 5. The analysis is approved for publication by the ATLAS Collaboration. Further, through the work on procedures described in Chapter 4, the author contributed to six additional ATLAS publications, where he is also listed as a co-author. These publications are listed below:

ATLAS papers

1. ATLAS Collaboration, *Measurements of azimuthal anisotropies of jet production in Pb+Pb collisions at* $\sqrt{s_{\mathrm{NN}}} = 5.02$ *TeV with the ATLAS detector*. Phys. Rev. C **105** (2022) 064903

2. ATLAS Collaboration, *Measurements of the suppression and correlations of dijets in Pb+Pb collisions at 5.02 TeV*, arXiv:2205.00682, **Accepted** by Physical Review C

3. ATLAS Collaboration, *Measurement of the nuclear modification factor of b-jets in 5.02 TeV Pb9Pb collisions with the ATLAS detector*, arXiv:2204.13530, **Accepted** by The European Physical Journal C

4. ATLAS Collaboration, *Measurement of substructure-dependent jet suppression in Pb+Pb collisions at 5.02 TeV with the ATLAS detector*, https://cds.cern.ch/record/2806467

5. ATLAS Collaboration, *Comparison of inclusive and photon-tagged jet suppression in 5.02 TeV Pb+Pb collisions with ATLAS*, https://cds.cern.ch/record/2805980

6. ATLAS Collaboration, *Measurement of suppression of large-radius jets and its dependence on substructure in Pb+Pb at 5.02 TeV by ATLAS detector*, https://cds.cern.ch/record/2701506

ATLAS proceedings

1. Martin Krivoš on behalf of the ATLAS Collaboration, *Measurement of angular and momentum distributions of charged particles within and around jets with the ATLAS detector*, **Published** in Revista Mexicana de Fisica, 3 (2022) 3, 0308116

2. Martin Krivoš on behalf of the ATLAS Collaboration, *Hard probes of heavy ion collisions with ATLAS*, **Accepted** in Elsevier

Appendices

A. Performance plots

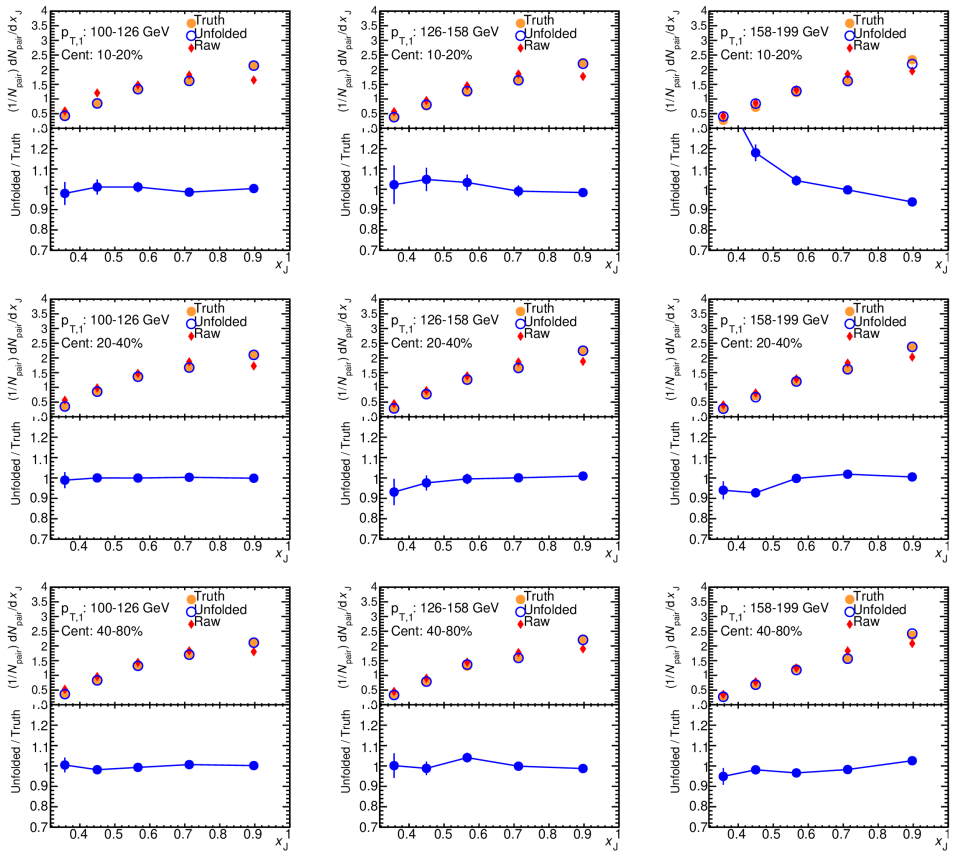

Figure A.1: Unfolding closure for three $p_{\mathrm{T},1}$ intervals and for $10-20\%$, $20-40\%$ and $40-80\%$ centrality intervals.

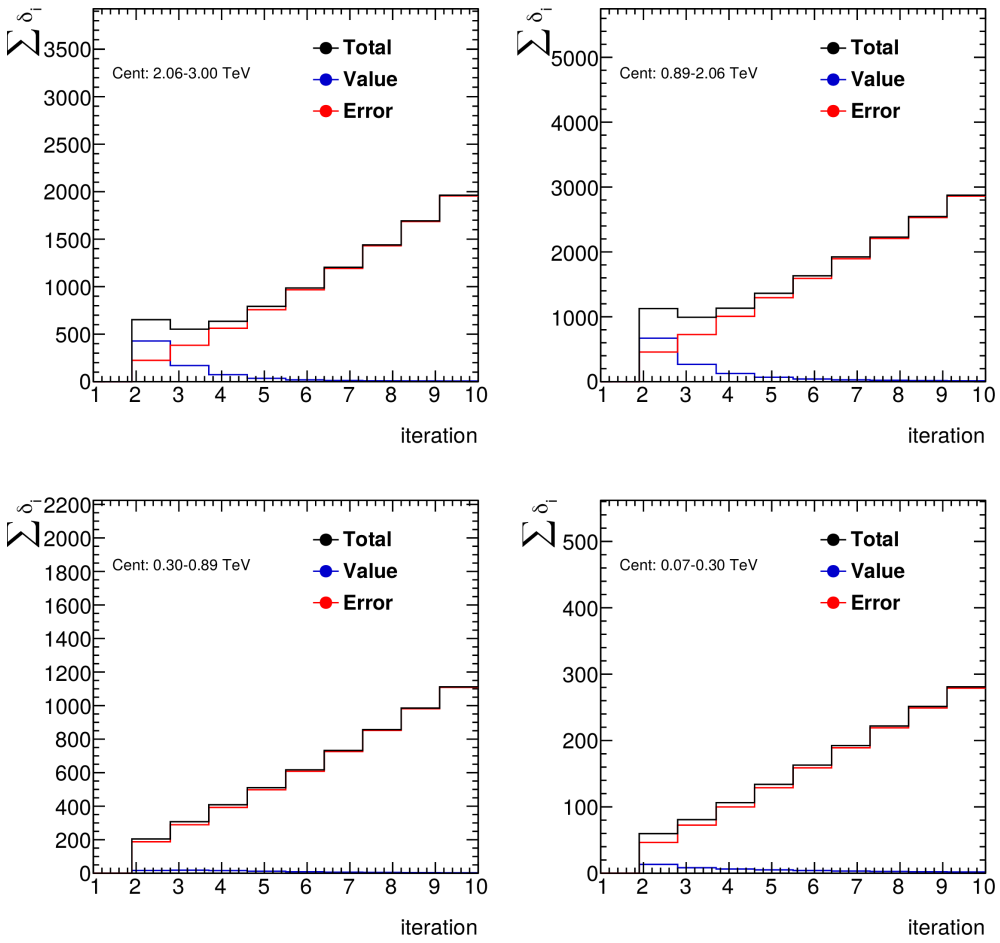

Figure A.2: Evolution of iterations for unfolding in $\Sigma E_{\mathrm{T}}^{\mathrm{FCal}}$ intervals.

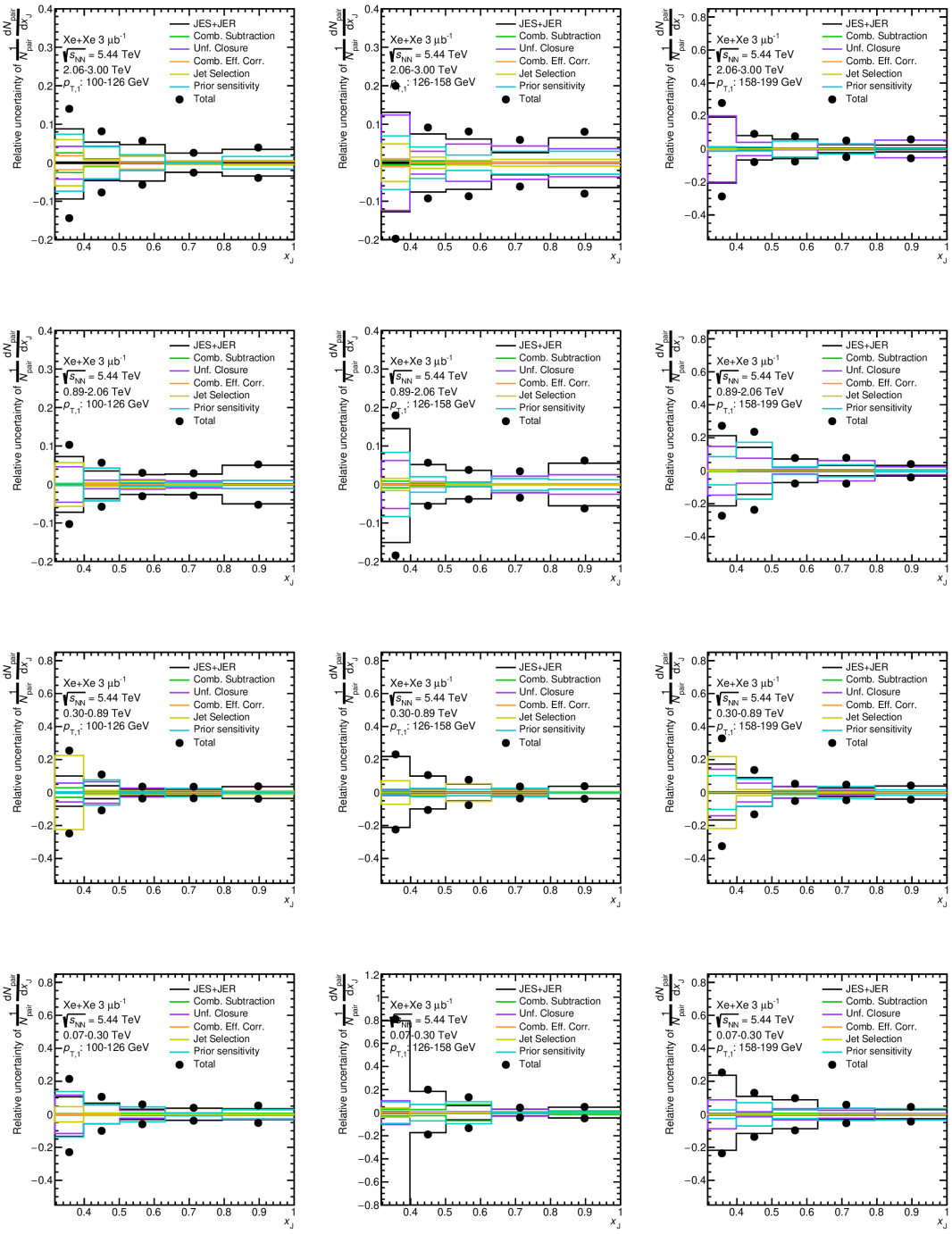

Figure A.3: Systematic uncertainties for x_{J} distribution for four $\Sigma E_{\mathrm{T}}^{\mathrm{FCal}}$ intervals and three leading jet p_{T} in Xe+Xe collisions at $\sqrt{s_{\mathrm{NN}}} = 5.44$ TeV.

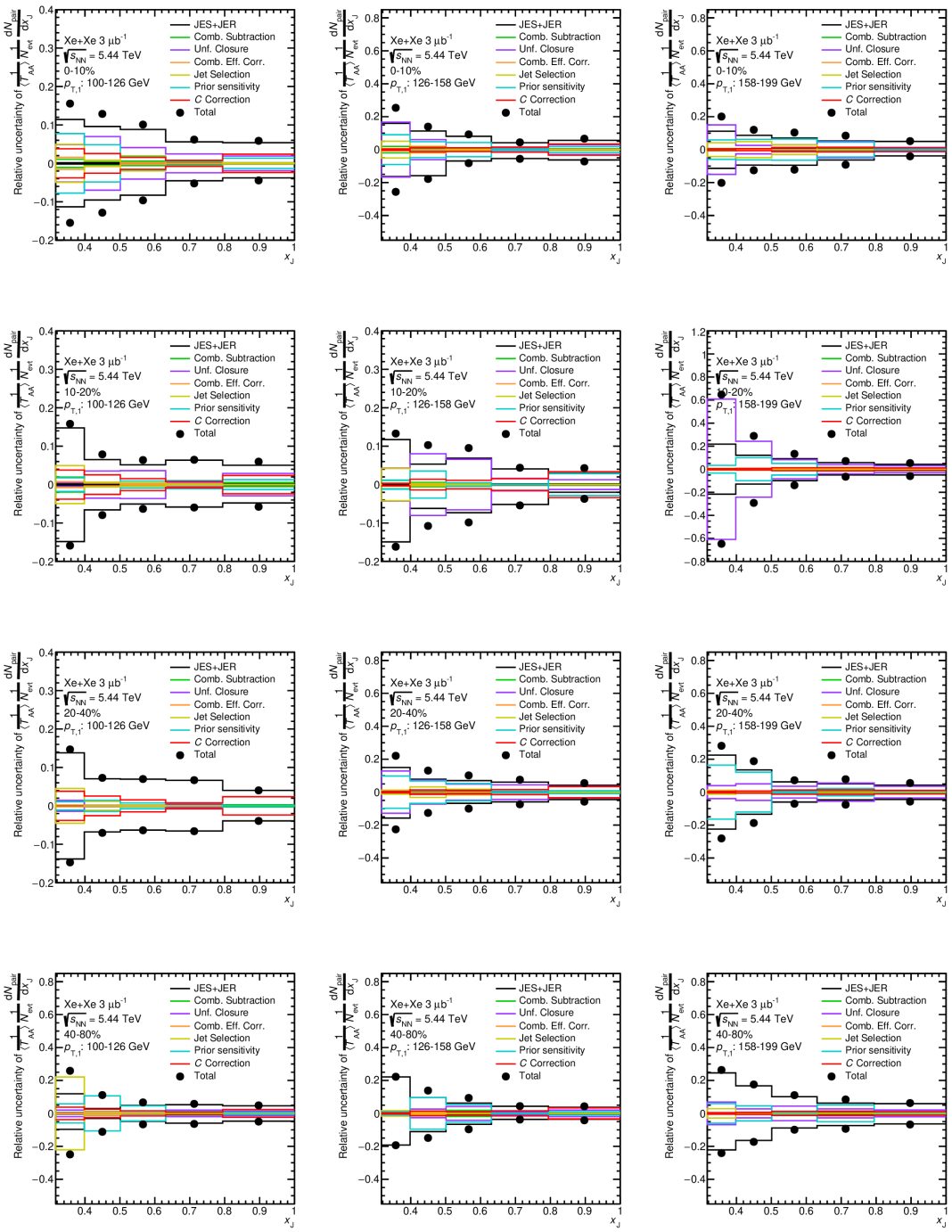

Figure A.4: Systematic uncertainties for absolutely normalized x_{J} distribution for four centralities and three leading jet p_{T} in Xe+Xe collisions at $\sqrt{s_{\mathrm{NN}}} = 5.44$ TeV. The $\mathcal{C}$ Correction systematic is applied on Pb+Pb distributions.

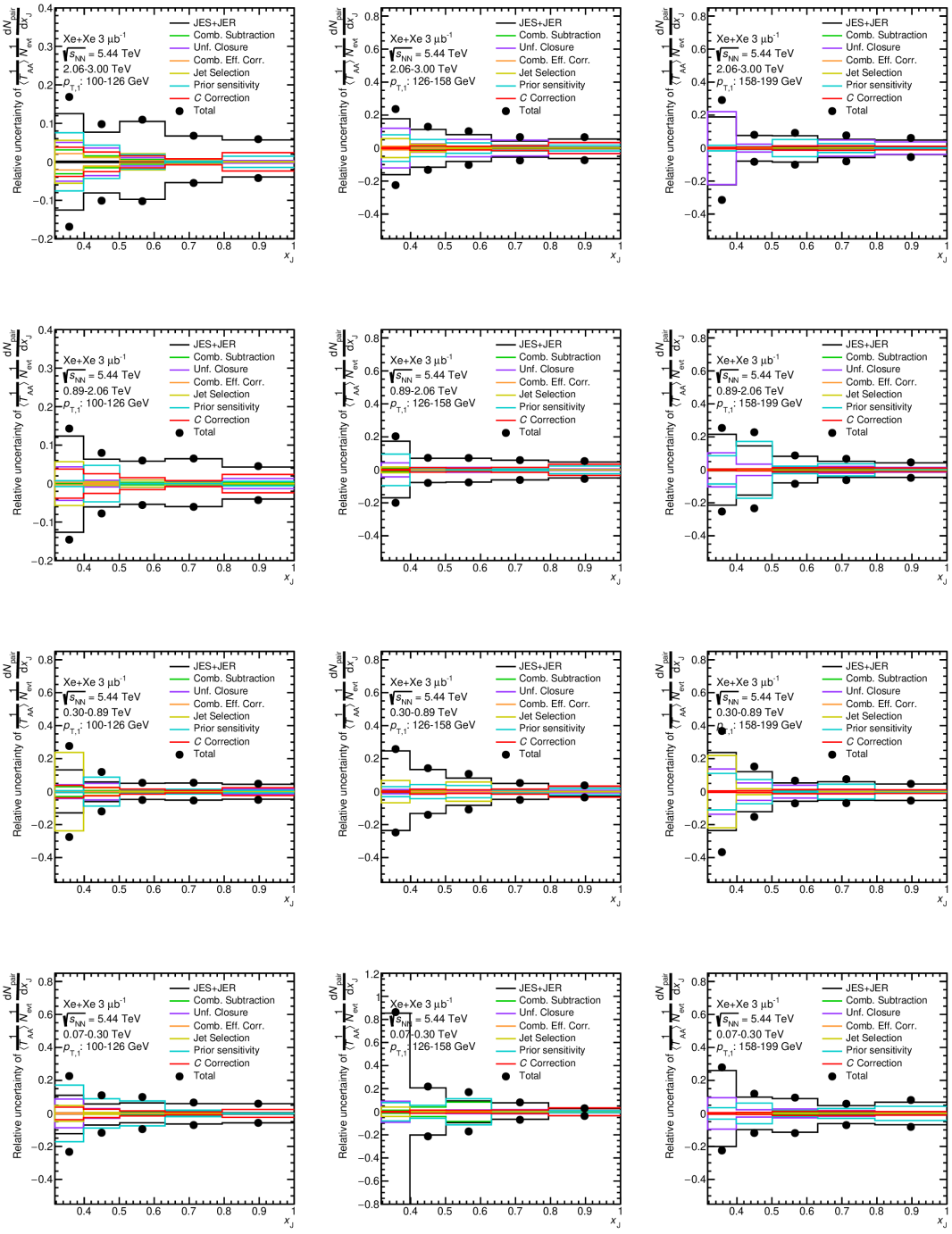

Figure A.5: Systematic uncertainties for absolutely normalized x_{J} distribution for four $\Sigma E_{\mathrm{T}}^{\mathrm{FCal}}$ intervals and three leading jet p_{T} in Xe+Xe collisions at $\sqrt{s_{\mathrm{NN}}} = 5.44$ TeV. The $\mathcal{C}$ Correction systematic is applied on Pb+Pb distributions.

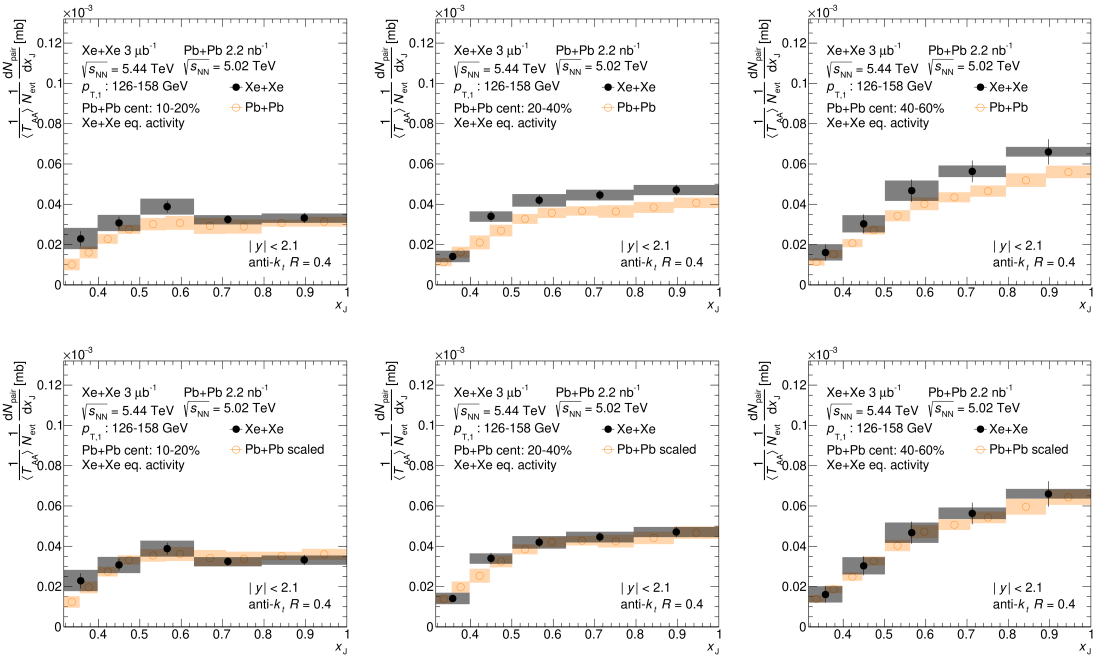

Figure A.6: Comparison of Xe+Xe (black) and Pb+Pb (orange) absolutely normalized x_{J} distribution in $126 < p_{\mathrm{T},1} < 158$ GeV and 10–20%, 20–40%, and 40–60% Pb+Pb centrality interval and in the corresponding Xe+Xe $\Sigma E_{\mathrm{T}}^{\mathrm{FCal}}$ intervals. The upper panels show directly measured distributions. The lower panels show Pb+Pb distribution corrected for the impact of the difference in the center-of-mass energy of the hard scattering process between Xe+Xe and Pb+Pb collisions (see text). Statistical and systematic uncertainties are represented by error bars and colored boxes, respectively.

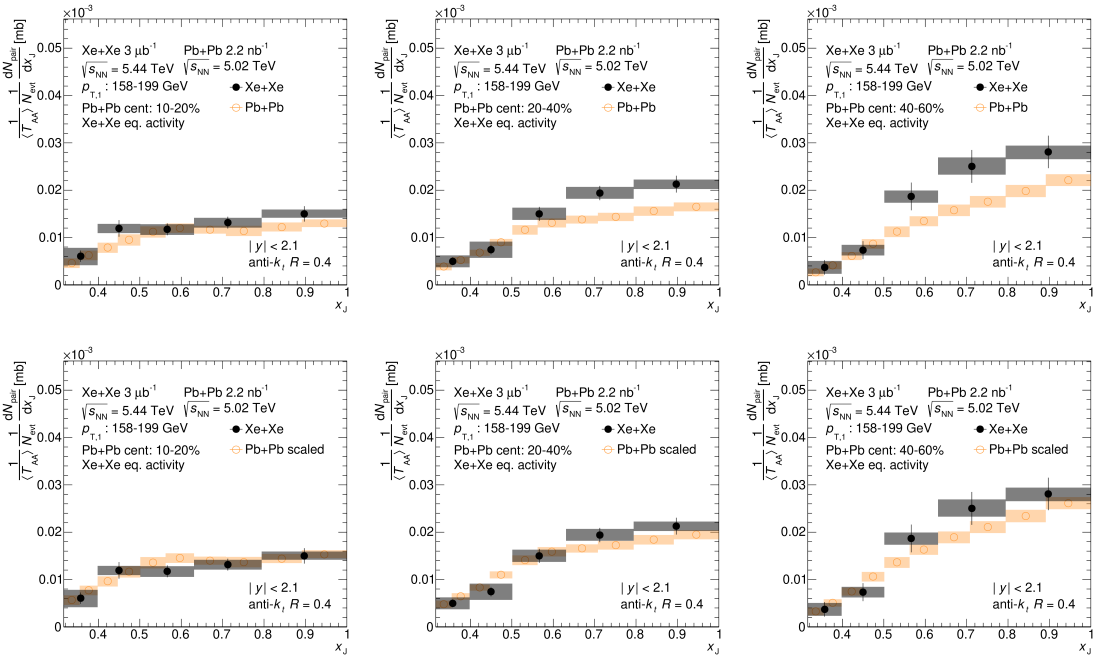

Figure A.7: Comparison of Xe+Xe (black) and Pb+Pb (orange) absolutely normalized x_{J} distribution in $158 < p_{\mathrm{T},1} < 199$ GeV and 10–20%, 20–40%, and 40–60% Pb+Pb centrality interval and in the corresponding Xe+Xe $\Sigma E_{\mathrm{T}}^{\mathrm{FCal}}$ intervals. The upper panels show directly measured distributions. The lower panels show Pb+Pb distribution corrected for the impact of the difference in the center-of-mass energy of the hard scattering process between Xe+Xe and Pb+Pb collisions (see text). Statistical and systematic uncertainties are represented by error bars and colored boxes, respectively.

Bibliography

[1] B. B. Back et al. The PHOBOS perspective on discoveries at RHIC. *Nucl. Phys. A*, 757:28–101, 2005.

[2] K. Adcox et al. Formation of dense partonic matter in relativistic nucleus-nucleus collisions at RHIC: Experimental evaluation by the PHENIX collaboration. *Nucl. Phys. A*, 757:184–283, 2005.

[3] I. Arsene et al. Quark gluon plasma and color glass condensate at RHIC? The Perspective from the BRAHMS experiment. *Nucl. Phys. A*, 757:1–27, 2005.

[4] John Adams et al. Experimental and theoretical challenges in the search for the quark gluon plasma: The STAR Collaboration's critical assessment of the evidence from RHIC collisions. *Nucl. Phys. A*, 757:102–183, 2005.

[5] ATLAS Collaboration. Measurement of the nuclear modification factor for inclusive jets in Pb+Pb collisions at $\sqrt{s_{\mathrm{NN}}} = 5.02$ TeV with the ATLAS detector. *Phys. Lett. B*, 790:108–128, 2019.

[6] ATLAS Collaboration. Comparison of Fragmentation Functions for Jets Dominated by Light Quarks and Gluons from *pp* and Pb+Pb Collisions in ATLAS. *Phys. Rev. Lett.*, 123:042001, 2019.

[7] ATLAS Collaboration. Medium-Induced Modification of Z-Tagged Charged Particle Yields in Pb+Pb Collisions at 5.02 TeV with the ATLAS Detector. *Phys. Rev. Lett.*, 126:072301, 2021.

[8] ATLAS Collaboration. Measurement of $W^{\pm}$ boson production in Pb+Pb collisions at $\sqrt{s_{\mathrm{NN}}} = 5.02$ TeV with the ATLAS detector. *Eur. Phys. J. C*, 79:935, 2019.

[9] ATLAS Collaboration. Z boson production in Pb+Pb collisions at $\sqrt{s_{\mathrm{NN}}}=$ 5.02 TeV measured by the ATLAS experiment. *Phys. Lett. B*, 802:135262, 2020.

[10] Charged-hadron production in *pp*, *p*+Pb, Pb+Pb, and Xe+Xe collisions at $\sqrt{s_{\mathrm{NN}}} = 5$ TeV with the ATLAS detector at the LHC. 11 2022.

[11] CMS Collaboration. Charged-particle nuclear modification factors in XeXe collisions at $\sqrt{s_{\mathrm{NN}}} = 5.44$ TeV. *JHEP*, 10:138, 2018.

[12] ALICE Collaboration. Transverse momentum spectra and nuclear modification factors of charged particles in Xe-Xe collisions at $\sqrt{s_{NN}} = 5.44$ TeV. *Phys. Lett. B*, 788:166–179, 2019.

[13] Z. Citron et al. Report from Working Group 5: Future physics opportunities for high-density QCD at the LHC with heavy-ion and proton beams. *CERN Yellow Rep. Monogr.*, 7:1159–1410, 2019.

[14] ATLAS Collaboration. Measurement of jet p_{T} correlations in Pb+Pb and pp collisions at $\sqrt{s_{\mathrm{NN}}} = 2.76\,\mathrm{TeV}$ with the ATLAS detector. *Phys. Lett. B*, 774:379, 2017.

[15] ATLAS Collaboration. Measurements of the suppression and correlations of dijets in Pb+Pb collisions at $\sqrt{s_{\mathrm{NN}}} = 5.02$ TeV. 5 2022.

[16] Michael L. Miller, Klaus Reygers, Stephen J. Sanders, and Peter Steinberg. Glauber modeling in high energy nuclear collisions. *Ann. Rev. Nucl. Part. Sci.*, 57:205–243, 2007.

[17] Cejnar, P. *A Condensed Course of Quantum Mechanics*. Karolinum Press, Charles University, 2015.

[18] Mark Thomson. *Modern particle physics*. Cambridge University Press, New York, 2013.

[19] Michael E. Peskin and Daniel V. Schroeder. *An Introduction to quantum field theory*. Addison-Wesley, Reading, USA, 1995.

[20] Jiri Horejsi. *Fundamentals of electroweak theory*. 2002.

[21] H. David Politzer. Reliable Perturbative Results for Strong Interactions? *Phys. Rev. Lett.*, 30:1346–1349, 1973.

[22] David J. Gross and Frank Wilczek. Ultraviolet Behavior of Nonabelian Gauge Theories. *Phys. Rev. Lett.*, 30:1343–1346, 1973.

[23] P. A. Zyla et al. Review of Particle Physics. *PTEP*, 2020(8):083C01, 2020.

[24] Matteo Cacciari, Gavin P. Salam, and Gregory Soyez. The anti-k_t jet clustering algorithm. *JHEP*, 04:063, 2008.

[25] S. Catani, Yu.L. Dokshitzer, M.H. Seymour, and B.R. Webber. Longitudinally-invariant k_t-clustering algorithms for hadron-hadron collisions. *Nuclear Physics B*, 406(1):187–224, 1993.

[26] Stephen D. Ellis and Davison E. Soper. Successive combination jet algorithm for hadron collisions. *Phys. Rev. D*, 48:3160–3166, 1993.

[27] Yuri L. Dokshitzer, G. D. Leder, S. Moretti, and B. R. Webber. Better jet clustering algorithms. *JHEP*, 08:001, 1997.

[28] M. Wobisch and T. Wengler. Hadronization corrections to jet cross-sections in deep inelastic scattering. In *Workshop on Monte Carlo Generators for HERA Physics (Plenary Starting Meeting)*, pages 270–279, 4 1998.

[29] Stephen Holmes, Ronald S. Moore, and Vladimir Shiltsev. Overview of the Tevatron Collider Complex: Goals, Operations and Performance. *JINST*, 6:T08001, 2011.

[30] Wit Busza, Krishna Rajagopal, and Wilke van der Schee. Heavy Ion Collisions: The Big Picture, and the Big Questions. *Ann. Rev. Nucl. Part. Sci.*, 68:339–376, 2018.

[31] Francois Gelis, Edmond Iancu, Jamal Jalilian-Marian, and Raju Venugopalan. The Color Glass Condensate. *Ann. Rev. Nucl. Part. Sci.*, 60:463–489, 2010.

[32] J. D. Bjorken. Highly Relativistic Nucleus-Nucleus Collisions: The Central Rapidity Region. *Phys. Rev. D*, 27:140–151, 1983.

[33] ALICE Collaboration. Measurement of transverse energy at midrapidity in Pb-Pb collisions at $\sqrt{s_{\mathrm{NN}}} = 2.76$ TeV. *Phys. Rev. C*, 94(3):034903, 2016.

[34] CMS Collaboration. Measurement of the pseudorapidity and centrality dependence of the transverse energy density in PbPb collisions at $\sqrt{s_{NN}} = 2.76$ TeV. *Phys. Rev. Lett.*, 109:152303, 2012.

[35] Pohl, R., Antognini, A., Nez, F. and others. The size of the proton. *Nature Phys.*, 466:213–216, 2010.

[36] Miklos Gyulassy and Larry McLerran. New forms of QCD matter discovered at RHIC. *Nucl. Phys. A*, 750:30–63, 2005.

[37] STAR BRAHMS, PHOBOS and PHENIX. *Nucl. Phys. A*, 757, 2005.

[38] Ulrich Heinz and Raimond Snellings. Collective flow and viscosity in relativistic heavy-ion collisions. *Ann. Rev. Nucl. Part. Sci.*, 63:123–151, 2013.

[39] Paul Romatschke and Ulrike Romatschke. *Relativistic Fluid Dynamics In and Out of Equilibrium.* Cambridge Monographs on Mathematical Physics. Cambridge University Press, 5 2019.

[40] H. Hahn et al. The RHIC design overview. *Nucl. Instrum. Meth. A*, 499:245–263, 2003.

[41] ATLAS Collaboration. Evidence for light-by-light scattering in heavy-ion collisions with the ATLAS detector at the LHC. *Nature Phys.*, 13(9):852–858, 2017.

[42] S. Chatrchyan et al. The CMS Experiment at the CERN LHC. *JINST*, 3:S08004, 2008.

[43] Sergei A. Voloshin, Arthur M. Poskanzer, and Raimond Snellings. Collective phenomena in non-central nuclear collisions. *Landolt-Bornstein*, 23:293–333, 2010.

[44] Arthur M. Poskanzer and S. A. Voloshin. Methods for analyzing anisotropic flow in relativistic nuclear collisions. *Phys. Rev. C*, 58:1671–1678, 1998.

[45] ATLAS Collaboration. Measurement of the pseudorapidity and transverse momentum dependence of the elliptic flow of charged particles in lead-lead collisions at $\sqrt{s_{NN}} = 2.76$ TeV with the ATLAS detector. *Phys. Lett. B*, 707:330–348, 2012.

[46] Bjoern Schenke, Prithwish Tribedy, and Raju Venugopalan. Fluctuating Glasma initial conditions and flow in heavy ion collisions. *Phys. Rev. Lett.*, 108:252301, 2012.

[47] J. Adams et al. Azimuthal anisotropy in Au+Au collisions at s(NN)**(1/2) = 200-GeV. *Phys. Rev. C*, 72:014904, 2005.

[48] A. Adare et al. Azimuthal anisotropy of neutral pion production in Au+Au collisions at $\sqrt{(}s_N N) = 200$ GeV: Path-length dependence of jet quenching and the role of initial geometry. *Phys. Rev. Lett.*, 105:142301, 2010.

[49] K Aamodt et al. Elliptic flow of charged particles in Pb-Pb collisions at 2.76 TeV. *Phys. Rev. Lett.*, 105:252302, 2010.

[50] Serguei Chatrchyan et al. Measurement of the elliptic anisotropy of charged particles produced in PbPb collisions at $\sqrt{s}_{NN}$=2.76 TeV. *Phys. Rev. C*, 87(1):014902, 2013.

[51] ATLAS Collaboration. Measurement of the azimuthal anisotropy of charged-particle production in $Xe + Xe$ collisions at $\sqrt{s_{\mathrm{NN}}} = 5.44$ TeV with the ATLAS detector. *Phys. Rev. C*, 101(2):024906, 2020.

[52] ATLAS Collaboration. Measurements of azimuthal anisotropies of jet production in Pb+Pb collisions at $\sqrt{s_{NN}} = 5.02$ TeV with the ATLAS detector. *Phys. Rev. C*, 105(6):064903, 2022.

[53] R. J. Glauber. Cross-sections in deuterium at high-energies. *Phys. Rev.*, 100:242–248, 1955.

[54] A. Bialas, M. Bleszynski, and W. Czyz. Multiplicity Distributions in Nucleus-Nucleus Collisions at High-Energies. *Nucl. Phys. B*, 111:461–476, 1976.

[55] Roger D. Woods and David S. Saxon. Diffuse Surface Optical Model for Nucleon-Nuclei Scattering. *Phys. Rev.*, 95:577–578, 1954.

[56] Martin Spousta and Brian Cole. Interpreting single jet measurements in Pb + Pb collisions at the LHC. *Eur. Phys. J. C*, 76(2):50, 2016.

[57] ATLAS Collaboration. Observation of a Centrality-Dependent Dijet Asymmetry in Lead-Lead Collisions at $\sqrt{s_{NN}} = 2.77$ TeV with the ATLAS Detector at the LHC. *Phys. Rev. Lett.*, 105:252303, 2010.

[58] CMS Collaboration. First measurement of large area jet transverse momentum spectra in heavy-ion collisions. *JHEP*, 05:284, 2021.

[59] ALICE Collaboration. Measurements of inclusive jet spectra in pp and central Pb-Pb collisions at $\sqrt{s_{\mathrm{NN}}} = 5.02$ TeV. *Phys. Rev. C*, 101(3):034911, 2020.

[60] ATLAS Collaboration. Measurement of $W^{\pm}$ boson production in Pb+Pb collisions at $\sqrt{s_{\mathrm{NN}}} = 5.02$ TeV with the ATLAS detector. *Eur. Phys. J. C*, 79(11):935, 2019.

[61] ATLAS Collaboration. Z boson production in Pb+Pb collisions at $\sqrt{s_{\mathrm{NN}}}$= 5.02 TeV measured by the ATLAS experiment. *Phys. Lett. B*, 802:135262, 2020.

[62] Comparison of inclusive and photon-tagged jet suppression in 5.02 TeV Pb+Pb collisions with ATLAS. 2022.

[63] Yu L Dokshitzer, V A Khoze, and S I Troyan. On specific QCD properties of heavy quark fragmentation (dead cone). *Journal of Physics G: Nuclear and Particle Physics*, 17(10):1602–1604, oct 1991.

[64] ATLAS Collaboration. Measurement of the nuclear modification factor for muons from charm and bottom hadrons in Pb+Pb collisions at 5.02 TeV with the ATLAS detector. *Phys. Lett. B*, 829:137077, 2022.

[65] Measurement of substructure-dependent jet suppression in Pb+Pb collisions at 5.02 TeV with the ATLAS detector. 11 2022.

[66] Martin Rybar. Private communication.

[67] LHC Machine. *JINST*, 3:S08001, 2008.

[68] CERN. LHC facts and figures. https://home.cern/resources/faqs/facts-and-figures-about-lhc.

[69] LHC Machine Outreach. http://lhc-machine-outreach.web.cern.ch.

[70] ATLAS Run Query, Xe+Xe collisions, Run 338037. Online.

[71] W. Herr and B. Muratori. Concept of luminosity. In *CERN Accelerator School and DESY Zeuthen: Accelerator Physics*, pages 361–377, 9 2003.

[72] The ATLAS Collaboration. The ATLAS experiment at the CERN large hadron collider. *Journal of Instrumentation*, 3(08):S08003–S08003, aug 2008.

[73] Atlas luminosity public results. https://twiki.cern.ch/twiki/bin/view/ AtlasPublic/LuminosityPublicResults.

[74] Kazunori Akai, Kazuro Furukawa, and Haruyo Koiso. SuperKEKB Collider. *Nucl. Instrum. Meth. A*, 907:188–199, 2018.

[75] CERN Courier. https://cerncourier.com/a/kek-reclaims-luminosity-record.

[76] G. Apollinari, O. Brüning, T. Nakamoto, and Lucio Rossi. High Luminosity Large Hadron Collider HL-LHC. *CERN Yellow Rep.*, (5):1–19, 2015.

[77] K. Aamodt et al. The ALICE experiment at the CERN LHC. *JINST*, 3:S08002, 2008.

[78] A. Augusto Alves, Jr. et al. The LHCb Detector at the LHC. *JINST*, 3:S08005, 2008.

[79] ATLAS Collaboration. Observation of a new particle in the search for the Standard Model Higgs boson with the ATLAS detector at the LHC. *Phys. Lett. B*, 716:1–29, 2012.

[80] CMS Collaboration. Observation of a New Boson at a Mass of 125 GeV with the CMS Experiment at the LHC. *Phys. Lett. B*, 716:30–61, 2012.

[81] Josh McFayden. *The LHC and ATLAS Detector*, pages 25–45. Springer International Publishing, Cham, 2014.

[82] Alessandro La Rosa. The ATLAS Insertable B-Layer: from construction to operation. *JINST*, 11(12):C12036, 2016.

[83] Peter Jenni, Marzio Nessi, and Markus Nordberg. Zero Degree Calorimeters for ATLAS. Technical report, CERN, Geneva, 2007.

[84] Trigger menu in 2018. Technical report, CERN, Geneva, 2019. All figures including auxiliary figures are available at https://atlas.web.cern.ch/Atlas/GROUPS/PHYSICS/PUBNOTES/ATL-DAQ-PUB-2019-001.

[85] Eduard Simioni. The Topological Processor for the future ATLAS Level-1 Trigger: from design to commissioning. 6 2014.

[86] ATLAS Collaboration. Jet energy scale and resolution measured in proton–proton collisions at $\sqrt{s} = 13$ TeV with the ATLAS detector. *Eur. Phys. J. C*, 81(8):689, 2021.

[87] Matteo Cacciari, Gavin P. Salam, and Gregory Soyez. FastJet User Manual. *Eur. Phys. J. C*, 72:1896, 2012.

[88] G. D'Agostini. Improved iterative bayesian unfolding, 2010.

[89] Tim Adye. Unfolding algorithms and tests using RooUnfold. In *PHYSTAT 2011*, pages 313–318, Geneva, 2011. CERN.

[90] ATLAS Collaboration. Xe+Xe centrality values,N_{coll}, T_{AA}.

[91] ATLAS Collaboration. Pb+Pb centrality values,N_{coll}, T_{AA}.

[92] ATLAS Collaboration. Measurement of the pseudorapidity and transverse momentum dependence of the elliptic flow of charged particles in lead–lead collisions at $\sqrt{s_{\text{NN}}} = 2.76\,\text{TeV}$ with the ATLAS detector. *Phys. Lett. B*, 707:330, 2012.

[93] ATLAS Collaboration. Study of photon-jet momentum correlations in Pb+Pb and *pp* collisions at $\sqrt{s_{\text{NN}}} = 5.02$ TeV with ATLAS. ATLAS-CONF-2016-110, 2016.

[94] Torbjörn Sjöstrand, Stefan Ask, Jesper R. Christiansen, Richard Corke, Nishita Desai, Philip Ilten, Stephen Mrenna, Stefan Prestel, Christine O. Rasmussen, and Peter Z. Skands. An introduction to PYTHIA 8.2. *Comput. Phys. Commun.*, 191:159–177, 2015.

[95] ATLAS Collaboration. https://cds.cern.ch/record/1966419.

[96] Richard D. Ball et al. Parton distributions with LHC data. *Nucl. Phys. B*, 867:244–289, 2013.

[97] Glen Cowan. *Statistical Data Analysis*. Clarendon Press, Oxford, 1998.